The University Of Sheffield.

Design of Hybrid Nanoantenna-Dielectric-Cavity with Strong Near-Field Intensity Enhancement

Thesis submitted for the Degree of Doctor of Philosophy

by

A. L. Torla

The University of Sheffield

2020

(This page is intentionally left blank)

The University Of Sheffield.

Design of Hybrid Nanoantenna-Dielectric-Cavity with Strong Near-Field Intensity Enhancement

Thesis submitted for the Degree of Doctor of Philosophy

by

Ahmad Lutfi Torla

Department of Electronic & Electrical Engineering

The University of Sheffield

April 2020

(This page is intentionally left blank)

Abstract

This dissertation investigates the Near-Field Intensity Enhancement (NFIE) of plasmonic nano-antennas in the visible and near-infrared frequency region and proposes a gold nanoantenna on a dielectric nanocavity for use in Surface Enhanced Raman Spectroscopy (SERS). Plasmonic nanoantennas allow direct coupling of light to metal and have since gained traction as fabrication methods have become more precise, allowing designs that were previously limited to theories. Attempts have been made to improve the NFIE but most of these efforts have been in improving the nano-antenna design as well as in the use of Fabry-Perot cavities. This dissertation therefore proposes a "*hybrid antenna*" in the form of a dielectric resonant cavity (DRC) coupled to a plasmonic dipole as a receiver. The interaction that occurs during the coupling is investigated in detail and a relation is made between the overall NFIE and the NFIE introduced by the dielectric resonator modes. A simple way to design dielectric resonator cavities for use at optical frequencies is introduced and data from two commercial electromagnetic field solvers and self-coded FDTD numerical analysis are compared against results found in literature. It is found that the addition of the proposed dielectric resonator nanocavity increases the NFIE of a plasmonic gold dipole by 21 times, from 1750 to 37k. It was further found that the NFIE can be increased further to 68k when mirrored with a gold slab, where other published results not employing optical cavities have a maximum NFIE of 29k. This dissertation contributes by proposing an effective and simple DRC that can significantly improve the near-field properties of surface plasmon resonance to be used in SERS measurements.

(This page is intentionally left blank)

Table of Contents

List of Figures

List of Tables

(This page is intentionally left blank)

List of Abbreviations

1D	1-Dimensional
2D	2-Dimensional
3D	3-Dimensional
ACS	Absorption Cross-section
ANSYS HFSS / HFSS	ANSYS HFSS electromagnetic solver software
ASE	Amplified Spontaneous Emission
B-B	Brendel-Bormann
CST	CST Microwave Studios
DNA	Deoxyribo Nucleic Acid
DR	Dielectric Resonator
DRA	Dielectric Resonator Antenna
DRC	Dielectric Resonant Cavity
DWM	Dielectric Waveguide Model
EBL	Electron-Beam Lithography
ECS	Extinction Cross-section
EM	Electromagnetic
FDTD	Finite Difference Time Domain
FEM	Finite Element Method
FIT	Finite Integration Technique

FP	Fabry-Perot
FSS	Frequency Selective Surface
GaAs	Gallium arsenide
GaSb	Galium Antimonide
GHz	Gigahertz
GP	Ground plane
InAs	Indium Arsenide
InSb	Indium Antimonide
LED	Light Emitting Diode
LP	Low profile
MATLAB	MATLAB numerical computing software
MMP	Multiple Multipole Program
MoM	Method of Moments
NA	Nanoantenna
NFC	Near Field Communication
NFIE	Near Field Intensity Enhancement
NIR	Near-Infrared
PEC	Perfect Electrical Conductor
QD	Quantum Dot
RCS	Radar Cross-section
RF	Radio Frequency
SBD	Single Big Dipole
SBR	Shooting Boundary Ray

SE	Spontaneous Emission
SERS	Surfaced Enhanced Raman Spectroscopy
Si_3N_4	Silicon Nitride
SP	Surface Plasmon
SPR	Surface Plasmon Resonance
SPRM	Surface Plasmon Resonance Microscopy
SWR	Standing Wave Ratio
$TE_{m,n,p}$	Transverse Electric mode
THz	Terahertz
TiO_2	Titanium Oxide
TSD	Two Small Dipoles
UV	Ultra Violet

(This page is intentionally left blank)

List of Publications

[1] A. L. Torla and S. K. Khamas, “Variation of Nanoantenna Characteristics Using Different Substrate Parameters,” in *Nanophotonics and Micro/Nano Optics International Conference 2016*, 2016.

[2] A. L. Torla and S. K. Khamas, “Near-Field Intensity Enhancement of a nano-antenna above an inverted Bragg Reflector,” in *2017 International Workshop on Antenna Technology: Small Antennas, Innovative Structures, and Applications (iWAT)*, 2017, pp. 304–307.

(This page is intentionally left blank)

Chapter 1: **Introduction**

The focus of this dissertation is to design plasmonic antenna configurations with improved performance for light collection and emission at Near-Infrared (NIR) frequencies. The improved performance has been achieved by truncating the supporting substrate of the nanoantenna so that it acts as a dielectric cavity resonator. This truncation has provided a considerable improvement in the Near-Field Intensity Enhancement (NFIE) as well as in the Spontaneous Emission (SE) of a quantum emitter that is placed in the feed gap of the plasmonic antenna.

1.1 Background

An antenna can be considered a transducer that converts an electrical signal to a radiated electromagnetic wave. It is commonly used in modern technology to transmit and receive data in applications such as radio and television broadcasting, radar, and satellite communications. An antenna can be evaluated in terms of various parameters such as the radiation pattern, gain, efficiency, bandwidth, and directivity [1]. These variables can be changed through the antenna design process, after which the designed antenna can be measured to ensure its response meets the required specifications. The antenna response can be separated into two regions; the near- and far field regions. These fields are defined to describe the more dominant field effects at certain distances, where in the near-field, some energy is trapped in the area near the antenna that is not radiated into the far-field. In the far-field however, any energy is radiated to infinity. The antenna far-field response is often the area of focus since it is usually used as a long-distance transceiver. However, the near-field response is useful for applications such as Near-Field Communications (NFC).

The demand for antennas has increased in the past few decades due to the proliferation of personal communication devices and long-distance communications through phone networks, media broadcasts and the internet [1]. Numerous antenna designs have been thoroughly investigated in terms of improvement and performance, although mainly in the radio and microwave frequency regions of the electromagnetic spectrum where most antenna communications occur.

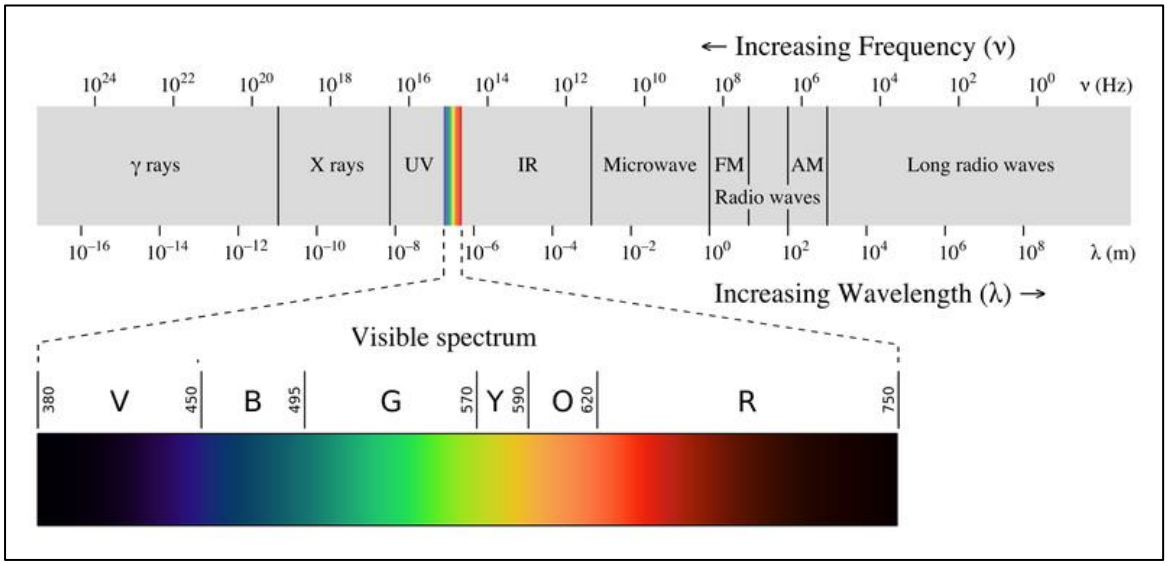

Figure 1.1: The electromagnetic spectrum showing the visible and infrared frequency bands [2]

The electromagnetic spectrum has been divided into various frequency bands for different applications, from radio waves to gamma rays, as illustrated in Figure 1.1. Considerable research which had focused on radio waves and microwaves have been undertaken and therefore have left very little in terms of research areas. However, research on infrared and visible frequency ranges are ripe for further research. The visible spectrum encompasses only a very small band of the whole electromagnetic spectrum but has strong potential for communications, and the infrared spectrum has similar capabilities. In recent years, scholars have carried out further research on optical antennas, in the hope of furthering high bandwidth communications [3]. An optical antenna operates in the optical

frequency range (including infrared, visible and ultraviolet frequencies) and has dimensions of tens or hundreds of nanometres, thus also being called nanoantennas, and is made from noble metals. The nanoantenna has many promising applications and areas of study. The utilization of the optical frequency range shifts some communications out of the packed RF and microwave bands when serving as far-field emitters and can serve well for the purposes of light collection. The antenna designs used for RF and microwave applications can also be duplicated in the optical frequency range based on the same electromagnetic theories, where similar and novel applications can be developed in the optical range. Optical antennas also benefit from a high bandwidth, even with a more limited frequency range due to the high operating frequencies, which allows higher data transmissions per second. Although far-field applications of optical antennas are of interest, optical antennas also have the interesting property of being able to produce promising results compared to traditional antennas, especially when considering the near-field. The light collection abilities of optical antennas are not limited by traditional antenna theory and are boosted by effects that occur in the optical band. This concentrates electric fields from waves of thousands of nanometres into volumes of tens of nanometres, which are tens or hundreds of times smaller than the excitation wavelength. These effects are called plasmonic effects and can increase the potential of optical antennas. However, the study of optical antennas has thus far been limited by fabrication techniques and advances in optical measurement devices. The development of nanoscience and nanotechnology in recent decades has prompted the growth of this field, which has in turn prompted further research into the theoretical underlying characteristics of nanoantennas.

Nanoantennas have certain unique properties in terms of the material behaviour in the optical band where metals do not behave as perfect conductors with a surface charge, but rather behave as negative dielectric materials, which are also frequency dependent. As

the dimensions approach single nanometres, quantum effects also become more apparent, which also affects behaviour. An excitation planewave does not disperse on the surface of the metal, but rather permeates the metal which acts as a cloud of electrons, or a plasma, which gives rise to Surface Plasmons (SPs). The existence of Surface Plasmons was first observed in 1902 [4] but a complete explanation only arose in 1968 [5], [6]. Additionally, SPs are resonant electron oscillations that occur at the boundary between two materials of positive and negative permittivity. This condition can be satisfied in the visible and near-infrared frequency ranges, where metals exhibit negative permittivity. This resonant oscillation travels parallel to the surface boundary and is extremely sensitive to the permittivities on both sides. This resonant oscillation has been termed as Surface Plasmon Resonance (SPR). Most present studies of optical antennas focus more on the field of optics and microscopy, and less on the electromagnetic theory and electric properties of the nanoantenna. Further investigations into improving the near-field resonance of nanoantennas are required, especially to investigate the response of traditional RF antenna designs at optical dimensions.

1.2 Objectives / Research direction

The main objective of this dissertation is to design a plasmonic antenna that has high Near Field Intensity Enhancement (NFIE) for use in Surface-Enhanced Raman Scattering (SERS) applications by coupling a plasmonic metal nanoantenna with a dielectric nanocavity. The parameters that govern the increase in the NFIE of plasmonic antennas are first established and the enhancements given by dielectric resonant cavities are subsequently explored. The NFIE of a hybrid plasmonic-dielectric antenna is optimized and maximized and its near-field properties are investigated.

Several research questions have been raised during this study. The first is focused on investigating the effects of a dielectric nanocavity on the response of a plasmonic antenna. Elementary investigations demonstrate a strong sensitivity to changes in the dielectric substrate of a nanoantenna, and the exact response of the nanoantenna is investigated according to changes in the dielectric cavity parameters. The second question is whether this study can demonstrate a significant increase in NFIE as compared to currently published results. Through survey of literatures and records of current results for nanoantennas, it has been concluded that a significant contribution can be made if the maximum light enhancement for a nanoantenna could be further increased. As a result, alternative methods to increase the NFIE are explored, other than through fine tuning the antenna design parameters. A straightforward approach to improve the NFIE is to accomplish improvements in terms of fabricating the plasmonic antenna with higher accuracy. However, there are well-known limitations in fabrication which require expensive machines to get down to molecular level fabrication. Alternative methods of increasing the NFIE should be considered which are explored in this work. Nano-antennas are known to be highly sensitive to changes in the environment, which leads to the understanding that if the incident light can be enhanced prior to exciting plasmonic resonance, proportional increases in the NFIE should also be observed.

Plasmonic antennas in the optical frequency range are expected to be highly sensitive to materials of different permittivity in the immediate environment. The addition of a dielectric resonant cavity of an optimized design and permittivity value should increase the NFIE of the overall structure. This approach has the advantage that it can be coupled with various plasmonic antenna designs. Furthermore, strategic use of dielectric mirrors and lenses should also facilitate focusing effects in order to further increment the resultant NFIE. The methods used to increase NFIE will also be investigated in terms of enhancing

spontaneous emission properties. These assumptions will be tested and compared against results from self-coded and commercial electromagnetic field solvers in the coming chapters.

There are certain limitations that surfaced during this dissertation. For example, when scaling antennas down to visible and near-infrared frequencies, the fabrication cost increases drastically. It is therefore not feasible to experimentally test the proposed designs through trial and error. Therefore, the results have instead been compared against the literature as well as against results from self-coded and commercial electromagnetic field solvers.

1.3 Literature Review

1.3.1 Maxwell equations and Mie theory

Nano-antennas in this work have been approached through the basis of electromagnetics and antenna theory, in which case it is imperative to come across the Maxwell equations [7] that govern every electromagnetics' aspect, except for quantum effects which are less relevant to antenna theory. The equations are based on a number of laws by other scholars, but which were collected and unified by Maxwell through a combination of four equations.

$$\nabla . \boldsymbol{E} = \frac{\rho_v}{\varepsilon_0} \tag{1.1}$$

$$\nabla . \boldsymbol{B} = 0 \tag{1.2}$$

$$\nabla \times \boldsymbol{E} = -\frac{\partial \boldsymbol{B}}{\partial t} \tag{1.3}$$

$$\nabla \times \boldsymbol{B} = \mu \boldsymbol{J} + \mu \varepsilon \frac{\partial \boldsymbol{E}}{\partial t} \tag{1.4}$$

where ρ_v is the volume electric charge density, J is the electric current density, ε is the permittivity and μ is the permeability. Equations (1.1) and (1.2) are the Gauss' Law and Gauss' Law for Magnetism, respectively. In addition, Equation (1.3) describes Faraday's Law and Equation (1.4) shows Ampere's Law. These separate equations collectively describe the underlying electromagnetic theory, which explains the antenna behaviour.

A particular solution for the Maxwell equations occurs when describing the scattering of light by a homogenous spherical particle, which is called the Mie theory [8]. Maxwell equations can be derived using certain assumptions for a sphere, which result in a solution in the form of an infinite series of spherical multipole partial waves.

$$Q_{extinction} = \frac{2}{x^2}\sum_{n=1}^{\infty}(2n+1)Re(a_n + b_n) \tag{1.5}$$

$$Q_{scattering} = \frac{2}{x^2}\sum_{n=1}^{\infty}(2n+1)(|a_n|^2 + |b_n|^2) \tag{1.6}$$

where $x = 2\pi r/\lambda$ is the diffraction parameter and a_n, b_n are the Mie scattering coefficients [7]. The Mie theory assumes that under certain conditions, a vanishingly small nanoparticle can act as an electric dipole, thus absorbing and scattering electromagnetic fields. This approach is generally used for spherical particles illuminated by a light source and can be useful to provide solutions for problems that include spherical antennas, including spherical nanoparticles.

Maxwell equations and the derived Mie theory fully describe all electromagnetic effects and are the basis of all electromagnetic solvers in the market today. Although the equations are complete, they are also rigorous, and require computational power to be solved to a high degree of accuracy. Antenna theory has been developed around these laws and certain limits have been noted by scholars that would be noticeable based on traditional antenna design and theory [7].

1.3.2 Antenna limits and diffraction theory

There are certain physical limitations to antennas designed using classical antenna theory as described by the Maxwell equations, which are the half-wavelength limit and the optical diffraction limit. The half-wavelength limit is well-known amongst antenna scholars whereby the minimum length of an antenna should be at least half a wavelength to resonate correctly with an electromagnetic wave [1]. The optical diffraction limit pertains to the limit of focusing optical waves which is usually done through the use of optical lenses and is limited by the relation:

$$d = \frac{\lambda}{2NA} \tag{1.7}$$

where d is the resolution and NA is the numerical aperture of the optical lens and can reach around ~1.5 in modern optics [9]. If a green light is used with a wavelength ~550 nm in conjunction with a lens of NA=1.4, the resolution limit is found to be ~200 nm, which is known as the Abbe diffraction limit that represents the lower resolution bound of the traditional optical microscope. A resolution of ~200 nm is sufficient when dealing with most biological cells which have a minimum size of 1 μm, but is found inadequate when imaging viruses that can be as small as 100 nm, or proteins with a size of 10 nm and simple molecules which can be as small as 1 nm [7]. Many attempts have been made to break through the diffraction limit, which has given rise to various forms of super-resolution microscopy including the use of plasmonics in optical antennas. Optical antennas, also known as nanoantennas, circumvent both the half-wavelength limit and the diffraction limit by harnessing the quantum effect of plasmons and can have resolution down to single nanometres. It should be noted that in the same way light, an optical oscillation, can be quantized into photons, plasma oscillations can be quantized into plasmons. These plasma oscillations arise from the interaction between a metal and positive dielectric material at

very high frequencies and form on the surface of the metal, lending it the name Surface Plasmon Resonance (SPR).

1.3.3 Surface Plasmon Resonance (SPR)

Surface Plasmon Resonance is a phenomenon that happens when a light wave is incident at the boundary between positive and negative permittivity materials. This phenomenon occurs most readily in metals at the visible and near-infrared frequency range where the metal's permittivity is negative [10]. At these frequencies, the metal behaves as a plasma with conduction electrons that are free to move within the metal while the relatively heavy ions are held in place. The metal thus behaves as a cloud of plasma [7] where an incident electromagnetic wave passes through the metal instead of being converted into a current, albeit with high ohmic loss [11]. The electrons then absorb the energy and oscillate, causing a localized non-radiative resonance that is strongest at the metal surface, which behaves as plasma oscillations. The plasma oscillations on the surface of the metal consists of plasmons, thus being termed "Surface Plasmon Resonance".

Because the resonance is strongest at the surface, SPR is not only affected by the used metal, but also by the behaviour of the positive permittivity dielectric material. Small changes in either side of the surface boundary can lead to a measurable change in the SPR frequency or enhancement. The detection of changes on the dielectric side of the boundary with a high sensitivity has allowed researchers to use SPR for measurement and sensing of changes in chemicals and proteins at a spatial resolution of single digit nanometres [12]. The effects of changes on the metallic side of the boundary have led researchers to test multiple antenna designs in order to improve the resonance capabilities, thus leading to more sensitive plasmonic devices. The sensitivity of plasmonic antennas is described by analysing the strength of the resonance on the surface of the metal. This is most easily

described through the electric field, *E*, with a unit of Volt per meter (V/m). Research was first carried out on plasmonic nanospheres and planar designs and was promptly applied in the fields of chemical sensing and SERS due to its sensitivity [12]. SPR is associated with a highly localized field over a range several orders of magnitude smaller than its wavelength. For example, an incident light at 150THz, i.e. a wavelength of ~2000nm, can be localized into regions of ~$10nm^3$ in volume. Changes at the scale of single digit nanometres therefore have an effect at much larger wavelengths and can greatly magnify the sensitivity of measurement instruments. These subwavelength properties have therefore been used in applications such as Surfaced Enhanced Raman Spectroscopy (SERS) for highly precise imaging, and chemical sensing to differentiate chemical signatures through plasmonic responses.

Although the theory has existed since the late 1960s, issues in the fabrications at such sizes have limited experimental studies until only the past few decades. Lithography technologies have matured greatly and techniques such as optical lithography with a resolution of 100nm have given way to alternative techniques such as Electron-Beam Lithography (EBL) with a resolution of 10nm [13]. These methods will be discussed in more detail in the later parts of this chapter. The emergence of these fabrication technologies have allowed the practical application of SPR sensing in several fields such as chemical sensing [14] and Raman spectroscopy [12].

An alternative approach to understand SPR is by visualizing metals as a collection of unbounded free electrons. At optical frequencies, this collection acts as a cloud of electrons, or a plasma, where the electrons absorb incident energy and oscillate. This behaviour as a plasma gave rise to the name “plasmonics”. This plasma has a negative permittivity which causes the behaviour to be distinct from antenna applications in the

microwave region. This has led to new applications of plasmonic antennas. One of the key parameters to measure strong SPR is the Near Field Intensity Enhancement (NFIE), also referred to as light intensity enhancement in some publications. The first and main reason for NFIE increases in a nano-antenna would be due to the plasmonic effect. As an incident electromagnetic wave affects a plasmonic material at certain frequencies surface plasmon resonance (SPR) can occur. This phenomenon can have two modes which are affected by the shape of the material, which are called the transverse surface plasmon resonance (TSPR) and longitudinal surface plasmon resonance (LSPR) [10]. The plasmonic resonance frequency for gold is sometimes quoted at 550 THz, however this only holds true for TSPR. The secondary mode for surface plasmon resonance is the longitudinal resonance that oscillates along the parallel axis and has a resonant frequency that reduces as the aspect ratio is increased. The longitudinal plasmonic resonance has been found to exhibit a more significant amplitude of the two resonances and is therefore an aspect that will be explored further in this paper. It has also been shown that the NFIE can be further increased through coupling two plasmonic structures [15]. The NFIE of two nanospheres has been shown to have a dramatic increase, which occurs due to the dual focusing effect of both structures into the gap between them. The effect of coupling also predictably shifts the resonant frequency down by approximately half, which is naturally due to the double length of the total structure. Although the frequency response changes drastically, the increase in NFIE is extremely large. This is highly beneficial to the proposed work due to the need for high sensitivity to identify the effects of the proposed hybrid structure.

As a separate phenomenon, there is also the lightning rod effect, so called due to the nature of the antenna to act like a lightning rod and focus the incident optical wave [16]. The lightning rod effect is highly reliant on the structure of the plasmonic antenna and occurs due to the sharp edges that focus the electric field to a smaller point or edge. The

sharper the edge, the stronger the lightning rod effect and this is visible due to the fact that dipoles with flat edges have a weaker NFIE than the dipole with a sharpened tip. Research has shown that a bowtie antenna has a significantly higher NFIE of 9000 V^2/m^2 compared to a dipole with an NFIE of 4500 V^2/m^2 [17]. This is partly due to the aforementioned lightning rod effect, which concentrates the incident optical wave at the bowtie tips, where increasing the sharpness of the tip leads to higher NFIE results. However, in this case, the bowtie tip has been rounded to 3nm to emulate real-world scenarios where the tip would not be perfectly sharp. Although the bowtie antenna has a high sensitivity and would produce a stronger NFIE, there are relatively fewer studies that utilize bowtie geometry, which makes the dipole antenna a better comparison with more published data sets. This can be attributed to the simplicity of simulating and fabricating dipole antennas versus bowtie antennas. To a much weaker degree, there is also the phonon effect which occurs due to random lattice vibrations of the dielectric material. This effect however is disregarded in this dissertation as it should not have a significant effect on the results and is also not the primary focus of this work. The final phenomenon to note would be the Purcell effect, which is related to the spontaneous emission and defined as the ratio between the modified and original spontaneous emission and will be discussed later in the chapter.

1.3.4 Application of Surface Plasmon Resonance

Plasmonic antennas have a distinct advantage of extremely high sensitivity and very strong localized electric fields. As a result, they have been employed in various sensing applications as well as in other optical communication systems.

1.3.4.1 **Chemical sensing**

One of the first fields to benefit from plasmonics was the biochemical sensing. Accurately measuring changes at the level of single molecules, or single nanometres has

always been a challenge [13]. For example, a strand of DNA, the gene carrier, is 2 nm long. Surface Plasmon Resonance (SPR) can accurately detect changes of 1 or 2nm and give a response in terms of the electric field strength, resonance frequency, or resonance angle [18]. This has given rise to the field of Surface Plasmon Resonance Microscopy (SPRM), which utilizes scanning angle SPR. The theory behind SPRM is that SPR takes place under particular conditions, one of them being that incident light must hit a plasmonic surface at the right angle for maximum resonance [19]. A light is shone upon a plasmonic antenna or plasmonic surface and an angle sweep is performed, while the reflected light is detected and measured. At the "resonance angle" the reflected light should drop drastically due to the absorption of the plasmonic surface. However, when the plasmonic material is in contact with another material of positive permittivity, its SPR parameters change and the resonance angle changes. This is easily seen through another angle sweep. When the guilty material changes in terms of size or chemical property, this change again affects the SPR response of the plasmonic metal [18]. This means that changes in a genetic DNA strand of 2nm in size, can be effectively detected using wavelengths of 500nm, i.e. green light. Other changes in chemicals and biomolecules can also be tracked such as density changes and tracking surface interactions of bio-molecules [20].

1.3.4.2 **Surface Enhanced Raman Spectroscopy (SERS)**

Another well-known application of SPRs is in Surface Enhanced Raman Spectroscopy (SERS). Normal Raman Spectroscopy uses reflected light for imaging and theoretically has a resolution of $0.61\lambda/NA$, where NA is the Numerical Aperture of the microscope lens being used [21]. A 530nm laser in the optical frequency range would have a theoretical spatial resolution of 361nm, but scattering and other losses would degrade that and the normally quoted resolution for Raman Spectroscopy is 1μm or 1000nm. However, SERS can increase the enhancement by factors of 10^{10}, which enables the detection of

single molecules. This can be achieved through the plasmonic effects, which greatly increase the electric field strength as well as the spatial resolution [19]. The same research explains that the enhancement factor depends on the electric field strength when the Raman modes are excited and the enhancement that has been reported is proportional to E^4, where E is the electric field strength. Another well-known parameter of measurement is the Near-Field Intensity Enhancement (NFIE), which is proportional to E^2. The NFIE is therefore more often published as a result since the Raman enhancement can be easily determined by squaring the NFIE. This is the main thrust of this dissertation, and therefore the main parameter to be enhanced is the NFIE.

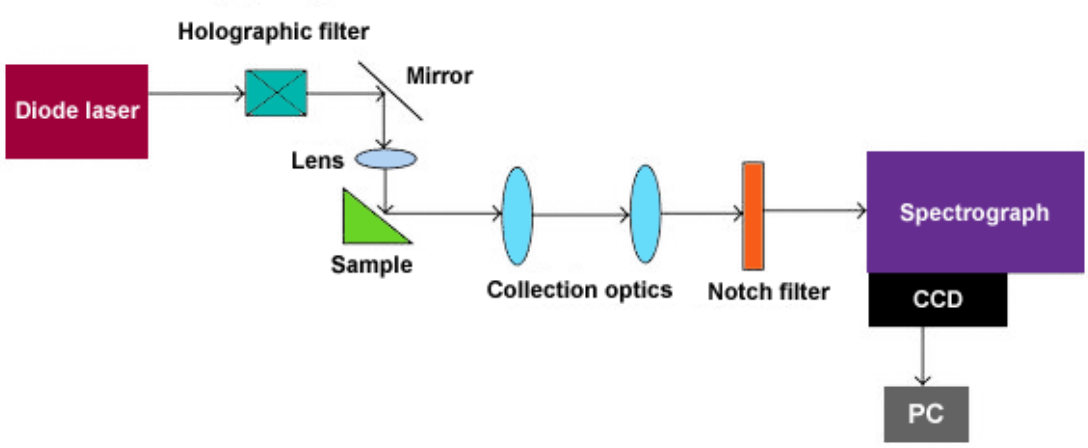

Figure 1.2: General example of the setup for a SERS experiment [22]

Figure 1.2 illustrates a general design for a SERS measurement. A diode laser sends a pulse through a filter, and the pulse is focused on a sample. In this dissertation, the sample would be the plasmonic gold dipole addressed in Chapter 3. The sample is excited and releases Raman scattering which is collected into a spectrometer and analysed using a computer. The analysis of the spectrometer would then allow the computer to reconstruct an image of the sample. This form of measurement allows nanometer accuracy at the cost of a fairly complex setup. It is important that the experimental setup must have extremely

high precision to ensure that the measurement is a success. Figure 1.3 displays a few different ways that Raman measurements can be performed.

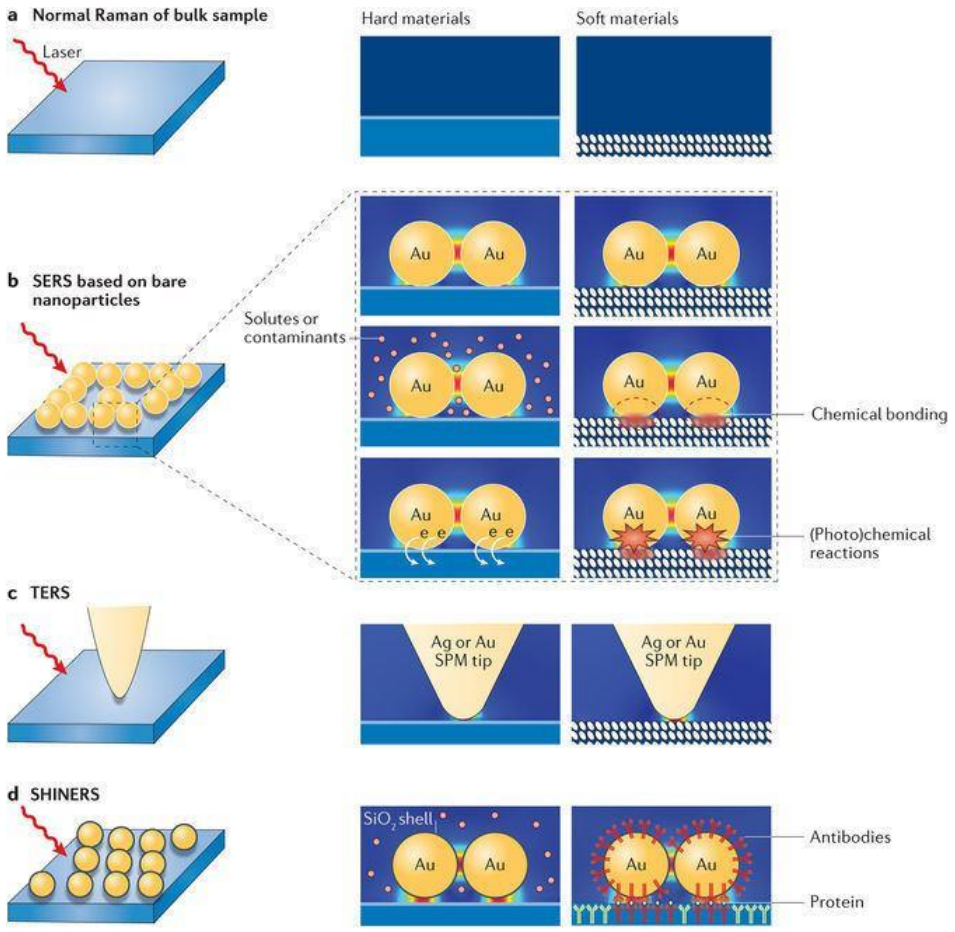

Figure 1.3: Example of Raman effects of different geometries [23]

1.3.4.3 **Solar Cells**

One area which could have considerable benefits from plasmonics is the development of solar cells that have traditionally used crystalline semiconductor wafers and make up the majority of currently installed systems [24]. New thin film strategies have been explored, and one of the approaches is to use plasmonic metals to convert an incident optical wave into an electric field, a.k.a., light to electricity. This could drastically improve the efficiency of solar cells, but research is still being carried out to optimize these designs, especially in terms of lowering their cost [24].

1.3.4.4 **Intra-chip optical communication**

Plasmonic antennas have already been shown to be able to catch light and convert it into electricity, thus acting as a detector. Furthermore, spontaneous emission can also utilize plasmonic antennas to enhance the emission from a quantum emitter [25]. The small dimensions of plasmonic antennas thus brings forward the interesting idea of using plasmonics to facilitate intra-chip optical communication [26]. Rather than using wires to transmit data within a chip, optical communication can be faster, generating less heat, as well as avoiding capacitive coupling issues, which can be important at miniaturization due to the existence of adjacent wires. However, these ideas are still heavily in the research stage.

1.3.5 Fabrication methods

As mention earlier, the applications of SPR only been made possible due to the advances in fabrication techniques. The following are an overview of a few fabrication technologies for creating nanometre sized structures and a brief description of their capabilities. One of the more commonly used techniques to fabricate in sub-micrometre designs is known as optical lithography, where a photomask and light are employed to transfer a "pattern" onto a photo-sensitive layer known as a "photoresist" [27]. However, the use of UV light limits the spatial resolution to ~100nm. Another fabrication process is known as multiphoton lithography, which is similar to optical lithography but without using photomasks. Instead, a direct laser is used, where photons are directly shone onto a photoresist to create the required pattern with a resolution of ~100nm [28].

An alternative process is known as scanning probe lithography, which also directly patterns a material without a photomask, thus bypassing the diffraction limit [29]. The photoresist is eliminated in this method, since patterns are created directly using

mechanical, thermal, chemical or electrical means. A few lithography methods under the umbrella term of scanning probe lithography are mechanical, thermochemical, dip-pen, oxidation, bias-induced, current induced, as well as thermally-assisted magnetic methods [30]. Resolution can be as high as 10nm depending on the method used. Electron-Beam Lithography (EBL) is one of the most commonly used fabrication processes in research studies, in which the resolution has improved from 20nm in the 1990s to ~10nm currently [13]. Such a high resolution has been achieved through focusing a beam of electrons onto a photoresist but has a low throughput. Another high-resolution technique known as Ion Beam Lithography, which utilizes a focused beam of ions that are heavier and have more momentum, and thus reduce scattering in the target [31]. In this process, a resolution of 5nm can be achieved if the ion beams are highly focused. However, this comes at the expense of energy loss and higher shot noise, which means that the random nature of photon emission for the lithography process can cause the fabricated structure to have rough edges that can significantly affect the response of the fabricated design [32]. The fabrication methods mentioned so far can all be classified as serial technologies, which means that they are considerably slow fabrication methods and hence are not entirely suited for mass-fabrication, which requires parallelization.

Nanoimprint lithography employs a mould with a nanoscale pattern, which allows the fabrication of multiple pieces at a time, in which a polymer is heated and softened, and the pattern is pressed on to create an "imprint". This method allows high throughput and consistency. Silicone moulds can last for a few thousand cycles and nickel moulds can last for ten thousand cycles reducing cost substantially with a spatial resolution of down to ~10nm depending on the pattern used [29]. On the other hand, chemical lithography methods provide a promising alternative to scanning beam technologies since chemicals are used to "etch" designs onto surfaces [33]. Additionally, on-wire lithography is a form

of chemical lithography that deals directly with segmenting wire structures where chemical etching is used to make disks as thin as 20m and wire gaps as short as 2nm [34]. However, the application is limited to wire designs. From this overview of fabrication techniques, it can be noticed that most of the fabrication methods have an upper resolution of ~10nm and this can be considered a suitable resolution target for the proposed designs in this work. Although certain technologies may allow for single nanometre resolution, they are limited to certain shapes or may have disadvantages in fabrication consistency. Thus, even when higher results may be achieved through reduced dimensions or reduced gap sizes, the performance of the proposed design may have to be compromised for feasibility in terms of fabrication and financial cost.

1.3.6 Reported plasmonic antenna designs

Table 1.1: Comparison of NFIE values from literature

Design	**Max *E* (V/m)**	**NFIE (V^2/m^2)**	**Methodology**	**λ (nm)**	**Notes**	**Source**
Sphere	13	170	Experimental	350	Silver	[35]
Sphere	-	-	Simulation	600	Investigated ECS	[36]
Dipole	18	300	Experimental	800		[37]
Coupled Sphere on Gold Slab	170	28.9k	Simulation	3000	10nm gap	[38]
Yagi-uda Array	16	256	Numerical	1500		[39]
Bowtie Aperture	7	49	Simulation	630		[40]
Bowtie on silica	60	3600	Simulation	1200		[41]
Crossed dipole	13	160	Simulation	1200		[42]
Dimer in Fabry-Perot Cavity	$9x10^6$	$8x10^{13}$	Simulation	630	- 5nm gap - Fabry-Perot cavity	[43]
Ellipsoid array in Fabry-Perot Cavity	80	6600	Simulation	700		[44]

Bowtie in Fabry-Perot Cavity	288	83k	Simulation	677	- 5nm gap - Fabry-Perot cavity	[45]
Coated Nanosphere	2.2	5	Simulation	1100		[17]
Spheroid	6	36	Simulation	850		[17]
Dipole over gold layer	70	4900	Numerical (FDTD)	785		[46]
Gold Nanorod	22	484	Experimental	6000		[47]
Coupled gold sphere on silver grating	40	1600	Experimental	N/A	5nm gap	[48]
Nanosphere array	50	2500	Experimental	1000		[49]
Plasmonic-dielectric metasurface	30	1000	Experimental	1400		[50]
Nanosphere array	1300	1.69×10^6	Numerical	380	Gap less than 2nm	[51]

Numerous scholars have explored light intensity enhancement by utilising nanoantenna configurations such as spherical [35][36], dipole [37], coupled sphere [38], Yagi-uda [39], bow-tie[40][41], dimer[43], cylindrical[17], and spheroidal[17] as well other geometries. Table 1.1 illustrates a comparison of the NFIE of various designs. A nanosphere represents one of the most basic plasmonic antenna shapes that has been investigated experimentally in [35], where the interaction effects between a plasmonic antenna and a dielectric substrate have been considered. In another article, it has been demonstrated that the gradual change of nanoantenna design from sphere to spheroid improves the directional response, increases resonant frequency and reduces the Extinction Cross-section (ECS) [36]. The Extinction Cross-section is the effective cross-section, which is characterized by the ability of the structure to both absorb and scatter an incident plane wave. The ECS depends on the Absorption Cross-section (ACS) and the Scattering/Radar Cross-section (RCS) according to the following equation:

$$ECS = ACS + RCS \tag{1.8}$$

It has been reported in that particular research that the design of a prolate spheroid yields a larger effect than that of an oblate spheroid. In the same article, it has been observed that an increase in the number of layers of a metal coating increases the resonance frequency and reduces the It has also been observed that increasing the metal coat thickness has a stronger increasing effect on the resonance frequency and ECS than varying the number of layers. Both changes in the nanoantenna and the superstrate have a measurable effect on the NFIE [36].

A typical plasmonic enhancement has been demonstrated in [37], which investigates the effect of antenna length on the resonance behaviour of a metal dipole. Using an arm length of 210 nm, a dipole antenna with a centre gap of 30 nm and thickness of 40 nm offered a NFIE of 300 V^2/m^2. In the same work, data has also been presented to demonstrate the variation of NFIE and resonance frequency as a function of dipole length where it has been noted that increasing the length results in higher NFIE as well as lower resonance. Coupled nanospheres have been investigated in [38], where two gold nanospheres on a gold slab have been analysed, where two distinct NFIE peaks have been observed. The first peak has been achieved when the two spheres resonate with each other and is referred to as the Two Small Dipoles (TSD) mode. This yields an electric field enhancement of up to 100 times compared to the incident light. However, at the second peak, the two spheres act simultaneously through the gold slab and this is referred to as Single Big Dipole (SBD) mode with an electric field enhancement of up to 170 times of the incident light. Due to the gold slab, the current flows freely between the two particles and therefore they act as one larger nanoparticle. The optical force between the two nanospheres has been investigated and it has been reported that the existence of an

exchange current due to the gold slab increases the optical force tremendously. Based on this study, coupled nanospheres can therefore offer a strong enhancement, but a large nanoantenna could claim to have equal or better enhancement, once again displaying that the size and shape of the nanoantenna can be crucial. One example of a more complex nanoantenna is a Yagi-Uda array [39], where it has been demonstrated that a highly directive beam can be achieved with an electric field enhancement factor of 16. However, the radiation efficiency is only 20%, but this could possibly be enhanced further with an improved design. Bow-tie shaped nanoantennas have been reported in [40], where a gold bow-tie aperture nanoantenna has been analysed using the Finite Integration Technique (FIT). It has been observed that an electric field enhancement factor of up to 6.5 can be accomplished, yielding an NFIE of 42. Factors that have been found to affect enhancement also include curvature, flare angle and gap size. It has also been reported that a sharper apex causes a higher enhancement at resonance with a measured directivity of 12.97dBi.

The impact of the bow-tie tip design on the field enhancement has been analysed in [41], where a bowtie nanoantenna design has been evaluated by adjusting parameters such as angle of the apex, tip size, spacing and length . The optimum design yields an electric field enhancement factor of up to 59. As a result of this comparison, it has been noticed that a nanoparticle pair offers a considerably higher field enhancement compared to a single nanoparticle, where the bowtie can be considered as a pair of triangular nanoparticles. This is also corroborated by [38] where it has been demonstrated that coupled nano-sphere pairs and coupled nano-rod pairs also generate higher electric field enhancements as compared to their single counterparts. The effect of cylindrical and spheroidal shapes on the nanoantenna field enhancement has also been evaluated in [17], where it has been reported that a spheroidal nanoantenna at 240 has a NFIE of 30, but a cylindrical nanoantenna of length 240 nm has a NFIE of 1000. This seems to imply that certain conditions can produce

a resonance that could considerably improve the NFIE. This is of interest and will be the general theme pursued later in the presented work.

Dipole nanoantennas have also been thoroughly investigated. As an example, a cross-nanoantenna using two orthogonal dipoles, which results in a polarisation independent antenna, has been reported in [42]. The feed gap between the dipoles highly affects the near-field intensity, e.g. when the feed gap is reduced from 30 to 20 nm, the intensity almost doubles. In the same paper, a maximum NFIE of 160 has been reported at a resonance frequency of 250 THz. Additionally, it has been noticed that for optical antennas, the resonance length is less than half-wavelength, i.e. 250nm instead of 600nm, which demonstrates a considerably different behaviour from that at microwave frequencies. Polemi and Shuford explored dimer antennas with a Fabry-Perot dielectric structure including a superstrate and substrate in [43]. Comparing the designs, with and without the Fabry-Perot structures, show a difference in directivity from 6.2 for a mirrored dimer to 17.5 for the dimer nanoantenna in a Fabry-Perot cavity. An array of ten dimer nanoantennas, has been reported to have a marginal improvement in the directivity to 18.1, and a strong improvement in NFIE of three times. The maximum recorded NFIE in the paper is $8x10^{13}$. This shows that both arrays as well as Fabry-Perot cavities are proven ways to increase the NFIE of a plasmonic antenna and will also be discussed in Chapter 4. Other attempts with a Fabry-Perot cavity have shown results of 6.6k [44] and 83k [45] NFIE, but none were as high as the work by [43] with an NFIE of $8x10^{13}$. The papers in [46]–[50] attempt various methods such as gold and silver substrates, arrays and also a multilayer nanorod consisting of metal-dielectric-metal. However, the NFIE results are not higher than 5k. [51] was able to obtain extremely high results of NFIE above 1 million due to the use of numerical analysis, and reducing the dipole gap size to less than 2 nm. In practice, it was discussed that gaps less than 2nm would be subject to damping effects, partly due to

behaving as one long arm, instead of two short coupled arms, which would eliminate the NFIE gains brought about by plasmonic coupling. The papers listed in Table 1.1 and discussed above represent the recent advances in nanoantennas of the past decade.

In contrast to recent publications, the pioneering studies in the field of plasmonic nanoantennas focused on simple geometric shapes such as individual gold nanoparticles such as spheres and ellipses placed at the end of fibre-based probes [52]. This experiment proved that the size and shape of the nanoantennas has a considerable effect on the localized field enhancement (NFIE). Furthermore, a higher refraction index for the surrounding media caused a red-shift in plasmon resonances, with different resonant wavelengths of 540 nm in air and 600 nm in water. Various methods of affecting the NFIE of SPR have been identified. One study compares the energy transfer between a source and a nanoparticle with and without a dielectric coating [53]. The purpose of the coating was to mitigate quenching, which reduces the total amount of transferred energy. However, the coating itself also reduces the overall efficiency. It has been reported that by tuning the frequency to match the coating thickness, the efficiency loss can be minimized while still reducing quenching. The tuning is required because the silica coating redshifts the resonance frequency by 15%.

This brief overview of nanoantenna designs shows that the behaviours of many different microwave antenna designs have already been explored at a nanometre scales. There are two potential areas of research that do not seem to have been fully explored at the moment, namely nanoscale Dielectric Resonator Antennas and the effects of variations in substrate design. It has also been observed that bowtie and nano-rod designs are attractive due to geometric parameters that can be tuned for improved performance even if the performance itself may be inferior compared to some other designs [43]. The electric field

enhancement can be increased when reducing the curvature of the tip, reducing the apex angle, reducing the gap, and increasing the length of the antenna. The resonance frequency is lowered when reducing the apex angle as well as gap and increasing the length of the antenna. It will be shown later that utilizing the designs proposed in this dissertation with a reduced gap size can surpass these results. One of the most relevant publications to this dissertation is [17], which was previously explained and which investigates various nanoantenna designs from the viewpoint of antenna theory. It remarks that the substrate thickness has a noticeable effect on the NFIE. This leads to an investigation in this dissertation on the effect of the substrate when it acts as a dielectric resonator.

1.3.7 Dielectric Resonators

Dielectric Resonator Antennas (DRAs) have the advantage of low losses due to its non-metallic nature [54]. DRAs come in various forms but are usually formed in simple geometric shapes such as cylindrical, rectangular or hemispherical. In this study, focus is placed on rectangular DRAs as a replacement for the supporting substrates. The performance of rectangular DRAs in the microwave region is well known and the equations governing its behaviour should be easily translated to the optical frequency range since it does not suffer from new plasmonic effects at the target operating frequency. These equation are based on the dielectric waveguide model (DWM) and can be summarized as below for the TE^{z}_{111} mode [54]:

$$H_x = \frac{(k_x k_z)}{j\omega\mu_0} \sin(k_x x) \cos(k_y y) \sin(k_z z) \tag{1.9}$$

$$H_y = \frac{(k_y k_z)}{j\omega\mu_0} \cos(k_x x) \sin(k_y y) \sin(k_z z) \tag{1.10}$$

$$H_z = \frac{(k_x^2 + k_y^2)}{j\omega\mu_0} \cos(k_x x) \cos(k_y y) \cos(k_z z) \tag{1.11}$$

$$E_x = k_y \cos(k_x x) \sin(k_y y) \cos(k_z z) \tag{1.12}$$

$$E_y = -k_x \sin(k_x x) \cos(k_y y) \cos(k_z z) \tag{1.13}$$

$$E_z = 0 \tag{1.14}$$

where,

$$k_x^2 + k_y^2 + k_z^2 = \varepsilon_r k_0^2 \tag{1.15}$$

$$k_z tan\,(k_z d/2) = \sqrt{(\varepsilon_r - 1)k_0^2 - k_z^2} \tag{1.16}$$

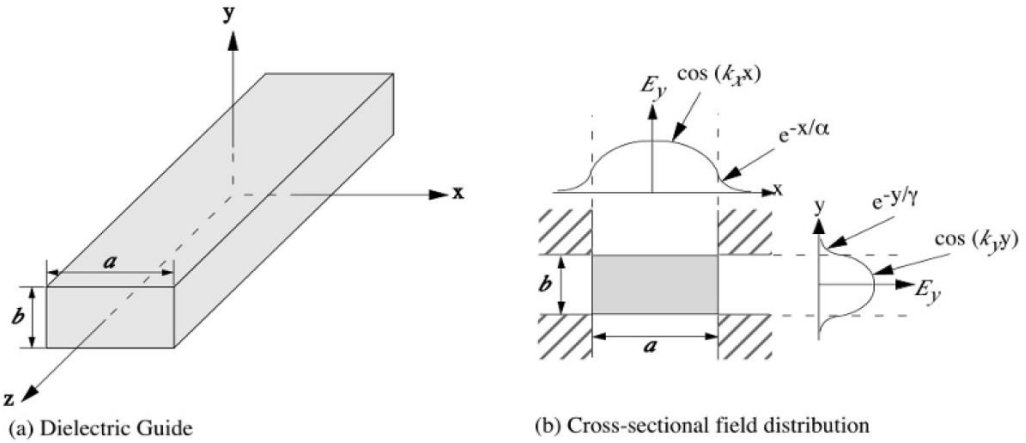

Figure 1.4: Dielectric Waveguide. Adapted from [55]

Equations (1.9) to (1.14) describe the fields within a dielectric resonator, which are utilized in a MATLAB code to calculate the modes resonance frequencies using Equations 1.15 and 1.16, where k_x, k_y, and k_z are the propagation constants for each dimension respectively and ε_r is the relative permittivity. It should be noted that these equations describe the behaviour of a truncated dielectric waveguide, which can approximate the behaviour of a dielectric resonant cavity.

1.3.8 Dielectric Designs in the Optical Range

Dielectric nano-resonators have not been explored as deeply as plasmonic antennas in this frequency range. One paper explores the use of a dielectric dimer on a silver slab used as a radiating nano-resonator [56], where a high radiation efficiency of 90% has been reported up until the near-infrared region. However, at frequencies higher than 300 THz, the loss drastically increases due to absorption by the silver slab. Another recent paper utilizes dielectric nano-resonators to form a unit-cell configurations, which can act as a perfect magnetic mirror [57], where a cross dielectric nano-resonator has been reported to have an in-phase reflection with reflectivity of 99.98% at 300 THz. This strongly shows that dielectric configurations can have strong resonance even in the visible and near-infrared region, leading to enhancement results.

1.3.9 Hybrid structures

Although the field of plasmonic-dielectric hybrid antennas has not been researched thoroughly, a number of studies have been published that have explored some of the responses of this type of antenna. One particularly interesting paper combines metallic antennas with a dielectric substrate to achieve strong spontaneous emission enhancements [58]. A nano-sphere has been placed on top of a dielectric resonator and the enhancement as well as the radiative decay rates were investigated. A spontaneous emission enhancement of 9 times has been reported. The radiative lifetime has been reduced from a few nanoseconds to a few hundred femtoseconds and radiative decay rates have increased from 3000 to 8000 a.u. (arbitrary units) with radiation pattern that is similar to that of a vertical dipole above a high-index substrate. However, this paper focused only on spontaneous emission and did not explore the effect of a plasmonic-dielectric substrate for near-field light intensity (NFIE) enhancement. The effects of the dielectric permittivity have been

studied, and it has been reported that increasing the permittivity, and thus the refractive index, is found to enhance the spontaneous emission significantly.

1.3.10 Other enhancement methods - Dielectric mirrors, Lenses, Fabry-Perot Cavities

Ground planes are often used in the microwave region to configure antennas in particular ways through reflection. The theory of using reflection in the optical frequency range should still hold true. However, problems arise due to the fact that ground planes are usually metallic, but at optical frequencies, the metal does not behave as a mirror but rather behaves as a plasma [5], [59]. Incident electromagnetic waves therefore have a high absorption rate in this frequency range. To increase the reflection of optical waves, the use of non-metallic mirrors such as dielectric mirrors must be explored.

1.3.10.1 Distributed Bragg Reflector

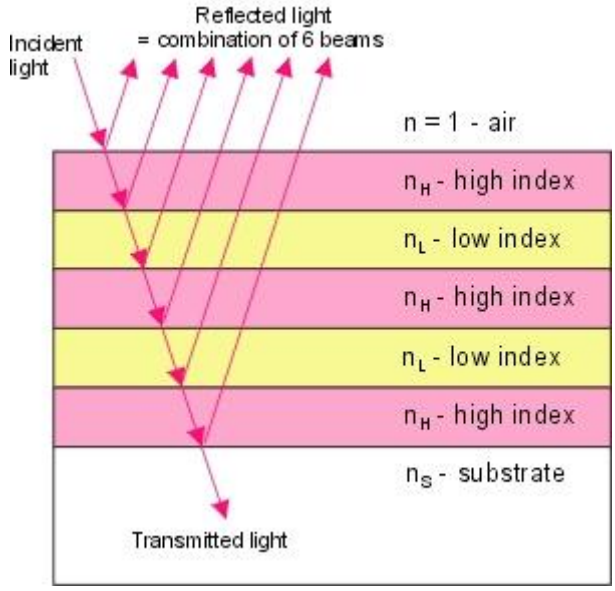

Figure 1.5: Diagram of a Distributed Bragg Reflector [60]. Incident and reflected light are propagating vertically with angle added for better visibility.

A Distributed Bragg Reflector is named due to the layered approach of partial reflection from a stack of dielectric layers. As light enters a high-index dielectric material,

it travels across the material to the other side. If the incident light then encounters a low-index material, the light is partially reflected. This incident light can continue to another layer of high-index and low-index material and will be partially reflected again. Adding on layers will increase the reflectivity of the stack, in the end creating a mirror with high reflectivity. This reflection is coherent due to the high and low-index layers having a set thickness of a quarter wavelength. This thickness means that when the light is reflected at the high-index and low-index boundary, it will be 180 degrees out of phase, but upon reflection and travelling back through 2 layers, it will then be at 0 degrees, or completely in-phase. This design is termed as the Distributed Bragg Reflector (DBR). The thicknesses of the high-index layer can be calculated as $t_H = \lambda/(4n_H)$ and the low-index layer calculated as $t_L = \lambda/(4n_L)$, where n_H and n_L are the respective refractive indices. The reflectance of the design can then be found through:

$$Y = \left(\frac{n_H}{n_L}\right)^{2p} \frac{{n_H}^2}{n_S} \tag{1.17}$$

$$R = \left(\frac{1-Y}{1+Y}\right)^2 \tag{1.18}$$

where n_H is the high-index of refraction and $n_L$is the low-index of refraction and n_S is the index of refraction for the final layer, the substrate. *p* is the number of layer pairs in the stack, *Y* is the admittance and *R* is the calculated reflectance. Equations 1.17 and 1.18 are approximations that hold for the condition where the incident light is vertical or near-vertical. Bragg reflectors are highly reflective in one direction as long as enough layer pairs are used. However, they are highly angle dependent.

A study of metal on a Bragg reflector showed that plasmon resonance occurs at their interface [61]. Although NFIE values were not recorded, the paper describes how multiple

layers are required to achieve high reflectivity, and that to gain the plasmon resonance a low-index first layer was used with a quarter-wavelength thickness. This phenomenon was noted and further research showed that Bragg reflectors with a high-index first layer will have a zeroed electric field on the surface due to the reflected and incident waves being out of phase. The use of a low-index first layer neatly avoids this issue and creates a surface with in-phase incident and reflected waves.

1.3.10.2 **2D and 3D Photonic Mirrors**

The Bragg reflector can be considered a 1-dimensional (1D) photonic mirror since it reflects light in only one direction. In an effort to create a mirror that is more robust in terms of angles, researchers have explored 2D and 3D versions of the Bragg reflector and have come up with various designs. The 2D photonic mirror has been widely researched and is often used to direct electromagnetic waves in the form of a waveguide, where the walls reflect the plane wave internally due to the dielectric mirroring. These 2D mirrors still have angle dependency but can work in two dimensions instead of just one. One paper designed a photonic crystal slab with patterned holes which shows strong reflectivity of >95% for incident angles of 0 – 15 degrees. However, beyond that angle, the reflectivity drops, with certain "zones" having high reflectivity peaks. The design had a dielectric constant of $\varepsilon_r = 12$ with thickness of $h = 0.55a$ and hole radius of $R = 0.4a$, where a is the distance between the centres of two holes [62]. 3D photonic mirrors have also been proposed that are attractive due to their angle-indifference. However, it is still a field in its infancy for nanotech purposes and has not been widely used at these dimensions.

1.3.10.3 **Fabry-Perot resonant cavities**

Fabry-Perot resonant cavities are used in lasers to drastically increase the amplitude of a stimulated emission laser. The incident laser is directed into a cavity with length of nλ/2 (multiples of half-wavelength) and the light is trapped between mirrors on both ends [63]. As more light is fed into this light trap, the laser reflects from one mirror to the other, with each round-trip building intensity. This is a well-known method of increasing light intensity. Although Fabry-Perot cavities are mentioned separately, they are not in fact a form of dielectric mirrors, but rather just an application of them. For example, Distributed Bragg Reflectors can be used to create Fabry-Perot resonant cavities by applying two Bragg reflectors with a gap of $n\lambda/2$ [43].

1.3.10.4 **Lenses**

Dielectric mirrors are one way to increase the amplitude of an incident electromagnetic wave through reflection, but other means also exist, including lenses. Lenses work by focusing incident light through a higher refractive index and focal design and include both classic optical lenses as well as a new category called superlenses that operate in the plasmonic region. A silver slab superlens combined with a coupled spheroid design has shown a NFIE of 1000 V^2/m^2 as seen in Figure 1.6 [64]. Both the superlens and coupled spheroid nanoantenna were designed with silver and simulated in COMSOL MULTIPHYSICS. The dimensions of the nanoantenna and superlens were optimized and the nanoantenna gap set to 20 nm.

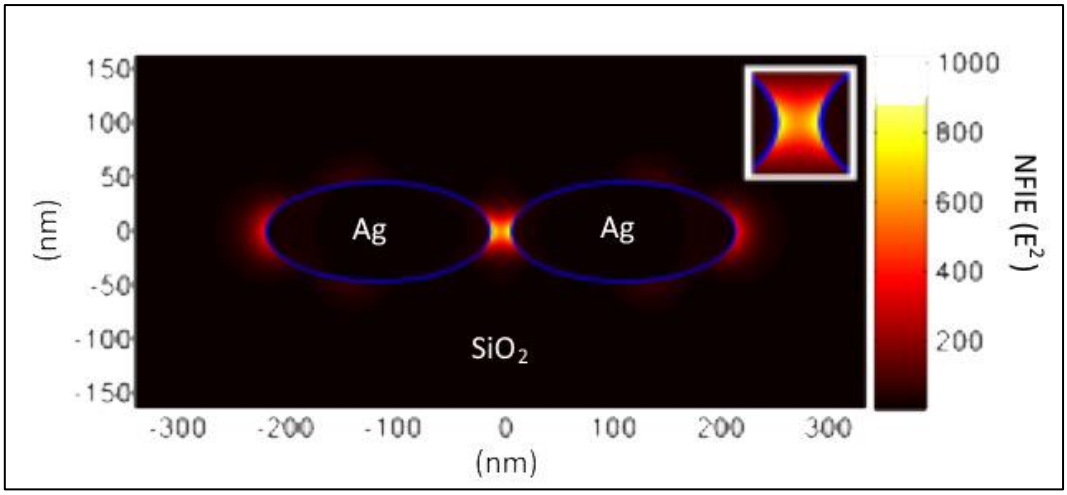

Figure 1.6: NFIE for a nanoantenna coupled with a superlens. Adapted from Liu et al [64]

1.4 Thesis layout

This dissertation is organized in the following way:

Chapter 1 has an overview of the entire thesis. A literature review also discusses the theory and design of plasmonic antennas and the plasmonic effect as well as its potential applications. The necessary and surrounding technologies are also discussed that place limitations on current fabrication of plasmonic designs and the current development of the field is also discussed.

Chapter 2 focuses on the designs and materials used in this dissertation and how they were selected for optimization and feasibility. The methodology and programs used for simulations are also discussed. Both the nanoantenna and dielectric cavity parameters are also optimized.

Chapter 3 discusses the optimization and tuning of the combined metallo-dielectric nanoantenna, also referred to as the "hybrid antenna". It also analyses the theory behind the increases gained due to the dielectric cavity.

Chapter 4 is devoted to the concept of other methods to increase NFIE including dielectric mirrors and their use as ground planes to further increase the intensity enhancement. Lenses and Fabry-Perot resonant cavities are investigated. Full-sized and low-profile dielectric resonators are also compared.

Chapter 5 utilizes FDTD numerical simulation to support the results found in Chapter 3. The same parameters are used for the design of the metallo-dielectric nanoantenna in terms of material composition as well as design structure. The differences in the results are compared to the results found in Chapter 3.

Chapter 6 concludes the thesis and proposes future works in this line of research.

1.5 Conclusion

Surface Plasmon Resonance is proven to have strong enhancement in the visible and near-infrared frequency range. The plasmonic resonance can be measured and compared in the near-field through the Near-Field Intensity Enhancement (NFIE) which is proportional to the square of the electric field strength. The combination of plasmonic antennas and other nanostructures can sometimes lead to stronger NFIE. One hybrid possibility is to combine plasmonic antennas with dielectric resonators which has not yet been deeply explored in the literature. This dissertation focuses on increasing NFIE through this and other methods.

Chapter 2: **Designs & Materials**

The motivations and background of this dissertation have been discussed in the previous chapter. In order to maximize the Near-Field Intensity Enhancement (NFIE), simulations and numerical analysis have been carried out using various methods to accomplish optimum designs with strong NFIE. Multiple methods were cross-checked to determine the consistency of the results, including comparison against numerical analysis, simulations using a commercial electromagnetic (EM) solver, and duplication of published results with the utilized software. In this chapter, the simulations and numerical analysis methodologies are explored to establish the foundation for the results obtained in the later chapters. The assumptions used during the calculations and simulations are also explained in sufficient detail.

The employed methodology has been presented over a number of sections where the used assumptions have been explained and the reasoning and validity of those choices are also explored, and the methods and software used for numerical analysis and simulations are explained. In addition, the materials and models used to simulate the plasmonic dipole and dielectric cavity are specified. Further, the choice of the nanoantenna design parameters has been discussed. Each of these choices has been compared against the closest alternatives and the reasoning behind such choices are explained.

2.1 Methods

The performance of a plasmonic structure can be assessed through numerical analysis, simulations as well as the use of experimental data from the literature.

2.1.1 Numerical Analysis

Numerical analysis can be considered the first step in theorizing an optimized design, where calculations can be carried out to determine if a particular design is viable according to the Maxwell equations as described in Chapter 1. However, the required computational electromagnetics can be rather complex and time consuming. A code has been compiled to automate the Finite-Difference Time-Domain (FDTD) calculations that can solve the Maxwell equations of the proposed structure. The code for the FDTD numerical simulation is as attached in Appendix A and utilizes external dependencies from the MIT Electromagnetic Equation Propagation (MEEP) project and the NumPy library. It was coded entirely in Python.

In Chapter 3, the optimum dimensions for a dielectric cavity was calculated using the dielectric waveguide model which was described in Chapter 1 [54]. Equations (1.9) until (1.14) describe the fields within a dielectric resonant antenna, which are derived to calculate the resonant frequency modes using Equations 1.15 and 1.16, where k_x, k_y, and k_z are the propagation constants for each dimension respectively and ε_r is the relative permittivity with k_0 as the wavenumber. A MATLAB code has also been developed to solve the above equations for a certain cavity size and permittivity and can be found in Appendix D. This step automates a large part of the calculations for dielectric cavity modes and has been used to generate data to compare against known and published results.

As a quick verification of the validity of our calculations, the script was run against published DRA results. Using the MATLAB script shown in Appendix D, the fundamental

mode has been calculated for a rectangular dielectric resonator with dimensions of 10mm x 10mm x 10mm and a relative permittivity of $\varepsilon_r=11$. This yielded a resonance frequency of f_r of 7.47 GHz. This agrees closely with the calculations reported in [54], where the same parameters yield $f_r \approx 7.55$GHz. More data comparisons will be provided in the next chapter when calculating the dielectric resonator modes. However, the aforementioned equations can only be used to determine the modes, and not the amplitude of the NFIE, which is one of the main parameters of this study. Therefore, numerical analysis and simulations must still be carried out using the FDTD code and a commercial electromagnetic solver.

Table 2.1: Comparison of first 20 calculated modes for a reported DRA [65]

Reported [65]		**Calculated (MATLAB)**		**Error**
m,n	Frequency (THz)	**m,n**	Frequency (THz)	
1,1	8.93	**1,1**	8.93	0%
3,1	12.46	**3,1**	12.46	0%
5,1	17.37	**5,1**	17.38	0.06%
7,1	22.78	**7,1**	22.79	0.04%
1,3	22.85	**1,3**	22.86	0.04%
3,3	24.38	**3,3**	24.39	0.04%
5,3	27.18	**5,3**	27.19	0.04%
9,1	25.42	**9,1**	28.43	11.84%
7,3	30.89	**7,3**	30.91	0.06%
9,3	35.25	**9,3**	35.26	0.03%
1,5	37.31	**1,5**	37.54	0.62%
3,5	38.26	**3,5**	38.48	0.58%
5,5	40.09	**5,5**	40.29	0.50%
7,5	42.69	**7,5**	42.87	0.42%
9,5	45.94	**9,5**	46.09	0.33%
1,7	51.89	**1,7**	52.03	0.27%
3,7	52.58	**3,7**	52.71	0.25%
5,7	53.93	**5,7**	54.05	0.22%
7,7	55.89	**7,7**	56.01	0.21%
9,7	58.40	**9,7**	58.51	0.19%

2.1.1.1 **Consistency of MATLAB calculations**

The MATLAB DRA script is compared against a reported DRA design [65] to ensure consistency. The reported design uses the parameters; *a=15.24mm, b=7.62mm, h=3.1mm and* ε_r*=10.8*. The thickness h was doubled to 6.2mm to account for the existence of a ground plane which would mirror the antenna. The excitation plane wave was directed from the Y-direction (length *b*).

The results of a reported DRA design were obtained with the relevant resonant frequencies and modes. The same design parameters were used in a MATLAB script (Appendix D) and the modes were calculated as shown in Table 2.1. A comparison between them shows that the results are almost exactly the same with minor errors for most modes, which lends credibility to our MATLAB calculations. However, the reported DRA design is in the gigahertz (GHz) frequency range whereas this work focuses in the visible and near-infrared range which is ~200 THz. This is a scale of 10,000 times smaller in terms of the antenna structure. To observe the behaviour of the DRA at optical scales, the dimensions are updated and scaled down.

2.1.1.2 **Resonance modes for scaled down DRA in the THZ region**

The reported DRA design was scaled down by a factor of 10,000 times. The scaled-down design was both calculated in MATLAB and simulated in CST. The parameters used for the design were; *a=1524nm, b=762nm, h=620nm and* ε_r*=10.8*. The calculated and simulated resonances are displayed in Table 2.2.

Table 2.2: First 20 calculated modes compared against simulated modes

Calculated (MATLAB)		**Simulated (CST)**		**Relative Difference**
m,n	Frequency (THz)	**m,n**	Frequency (THz)	
1,1	89.3	**1,1**	95	6.4%
3,1	124.6	**3,1**	-	
5,1	173.8	**5,1**	185	6.4%
7,1	227.9	**7,1**	-	
1,3	228.6	**1,3**	-	
3,3	243.9	**3,3**	-	
5,3	271.9	**5,3**	-	
9,1	284.3	**9,1**	-	
7,3	309.1	**7,3**	315	1.9%
9,3	352.6	**9,3**	-	
1,5	375.4	**1,5**	-	
3,5	384.8	**3,5**	-	
5,5	402.9	**5,5**	-	
7,5	428.7	**7,5**	430	0.3%
9,5	460.9	**9,5**	-	
1,7	520.3	**1,7**	-	
3,7	527.1	**3,7**	-	
5,7	540.5	**5,7**	-	
7,7	560.1	**7,7**	555	0.9%
9,7	585.1	**9,7**	-	

Table 2.2 lists some of the modes found in CST along with their resonant frequencies. However, the modes in CST were not always clear and therefore only the modes with high peaks were recorded to avoid discrepancies. A small variation is found as compared to the MATLAB results but overall the error rate is less than 7% which shows good agreement and the DRA model is shown to be valid. The CST results are clearly supported by our MATLAB predictions. The modes predicted in MATLAB can also be seen at the expected frequencies. However, not all resonant peaks show up as strong modes in our simulations and therefore certain peaks are more preferable than others and there are a few modes that show a strong amplitude in our CST simulations. Ideally, the dipole and

the DRA should have resonant peaks at the same frequency which will lead to highly efficient coupling and a stronger NFIE. The dimensions of both the dipole and dielectric cavity can be roughly identified through numerical analysis but can be best optimized through simulations.

2.1.2 Simulations

The well-known traditional methods that can be used to accurately model the optical behaviour of nanoantennas are mainly based on utilizing integration and differential equation formulations of the Maxwell equations and include methods such as the Finite Difference Time Domain (FDTD) method [46], [66], [67], the Finite Element Method (FEM) [64], [68], as well as the Finite Integration Technique (FIT) [40], [69]. FDTD is considered the simplest solution and is the only method that can be realistically implemented as a custom solution. It computes the Maxwell equations mentioned in Chapter 1 in their partial differential form. Transient responses are more accurately modelled by FDTD which makes it more suitable for time-domain calculations. In comparison, FEM also solves the Maxwell equation in partial differential form but has been found to be optimized for curved designs and frequency domain calculations. Curved geometrical objects can be more accurately modelled as finite elements in a non-orthogonal grid. The discretization of the total volume into grids allows solutions of the Maxwell equations at each point. Refining the grids into a denser mesh therefore leads to more accurate results. Another well-known method is FIT which solves the Maxwell equations but in an integral form. It maintains the idea of grid discretization to divide the problem into smaller grids and then solving for each grid. It has been found to be more optimized for solving designs with a large bandwidth and operates in the time-domain. Finally, the Method of Moments (MoM) can also provide fast and accurate EM solutions but has a disadvantage in that the complexity increases proportional to the third power as the mesh

or grid size decreases whereas FEM complexity only increases to the second power with decreasing mesh size. MoM also is not effective in modelling finite dielectric and dispersive behaviour, which is a large part of plasmonic modelling. Some widely known electromagnetic field solvers include COMSOL, CST Microwave Studio, ANSYS HFSS and Lumerical. Among these commercial softwares, ANSYS HFSS and CST Microwave Studios have been utilized to design and analyse the proposed configurations. This is in line with the approaches followed in numerous published studies [38], [40], [42].

CST Microwave Studios is a simulation program with a focus on electromagnetic solutions. Specifically, it provides numerical solutions to Maxwell equations with a focus on accuracy. There are a number of options in terms of solvers and methods including the Finite Integration Technique (FIT), Finite Element Method (FEM), and method of moments (MoM). CST employs FIT for the transient solver; FEM [70] for the frequency domain and eigenmode solvers, and MoM for the Integral equation solver. This is in conjunction with various other solvers such as the shooting Boundary Ray (SBR) through the installation of additional modules. CST has been licensed by the University of Sheffield and hence was the first electromagnetic solver option for this work, where simulations have been be carried out using the transient (time domain) solver which utilizes FIT.

It should be noted that COMSOL is another of the industry standards that utilizes the Finite Element Method (FEM) to solve electromagnetic equations. On the other hand, Lumerical utilizes Finite-Difference Time Domain (FDTD) and Finite-Difference Eigenmode (FDE) to solve Maxwell equations. Other solvers that have been utilized in this field include JCMwave, which is a FEM Maxwell solver for optics, and Multiple Multipole Program (3D MMP), which is a FORTRAN code for electromagnetics simulation described by a text book [71].

Finally, ANSYS HFSS (HFSS) is another well-known electromagnetics simulation software. However, it is more often used for frequencies below the optical region, more specifically in the microwave region. Although it is not as commonly used for plasmonic modelling as CST or COMSOL which have specific modules for optical simulation, it can still be used as a secondary tool to prove simpler behaviour models. The main solver for HFSS is FEM, but it also has a time-domain solver which utilizes MoM. HFSS is also available and licensed for the use of this project and therefore was utilised to generate more supporting data.

Table 2.3: Comparison of NFIE calculated using different electromagnetic field solvers for a pair of gold spheres with radius of 40nm and gap size of 1nm [72]

Electromagnetic solver	$\|\mathbf{E}\|^2$
COMSOL	576,840
JCMwave	547,347
HFSS	556,290
CST	~570,000 (approximate value from graph)
3D MMP	547,624

Although each program has certain differences, in general they have good accuracy once the settings are tuned and can be used to obtain fairly accurate results. Table 2.3 shows results obtained when simulating the NFIE of a pair of gold spheres with a radius of 40nm and a gap size of 1nm using the different solvers including CST, HFSS, and COMSOL, as well as MMP and JCMwave [72]. It has been demonstrated in the paper that as denser meshes are used, all the solvers give converging results of approximately 570k V^2/m^2. In the absence of any glaring differences, this dissertation has defaulted to the use of CST Microwave Studio (CST), which is readily available at the University of Sheffield. ANSYS HFSS is also available but the accuracy of both solvers is shown to be identical. Our results are mainly be solved over a fairly large bandwidth of 100 THz in which case the FIT

method or time-domain solver is a better choice due to its efficiency for wide-bandwidth solutions. Therefore, CST has been chosen as the main simulation tool. However, HFSS has also been used as a tool for confirming the accuracy for some of the simpler design structures. In addition, some of the structures simulated in CST have been corroborated using MATLAB numerical analysis, FDTD numerical analysis, as well as experimental data from the published literature. These are shown in the following chapters where relevant.

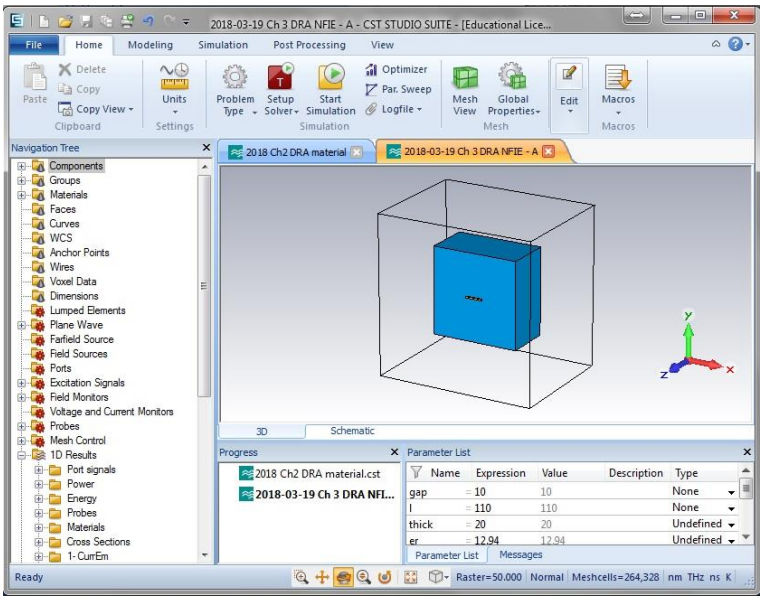

(a)

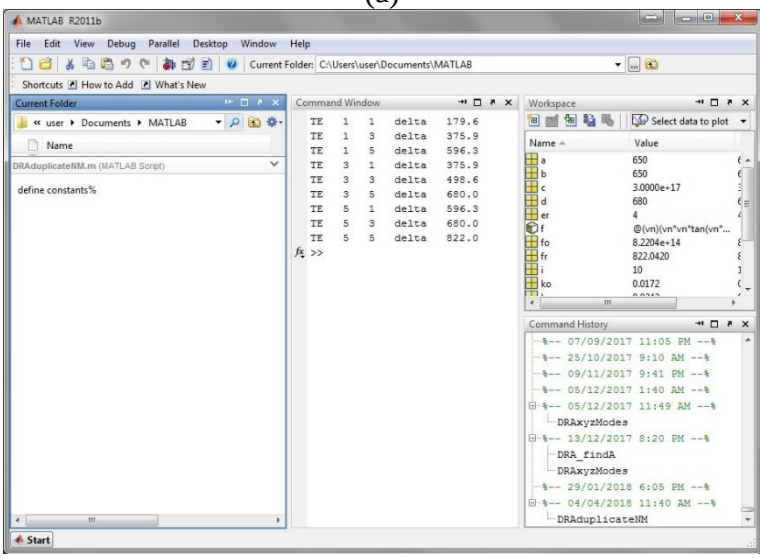

(b)

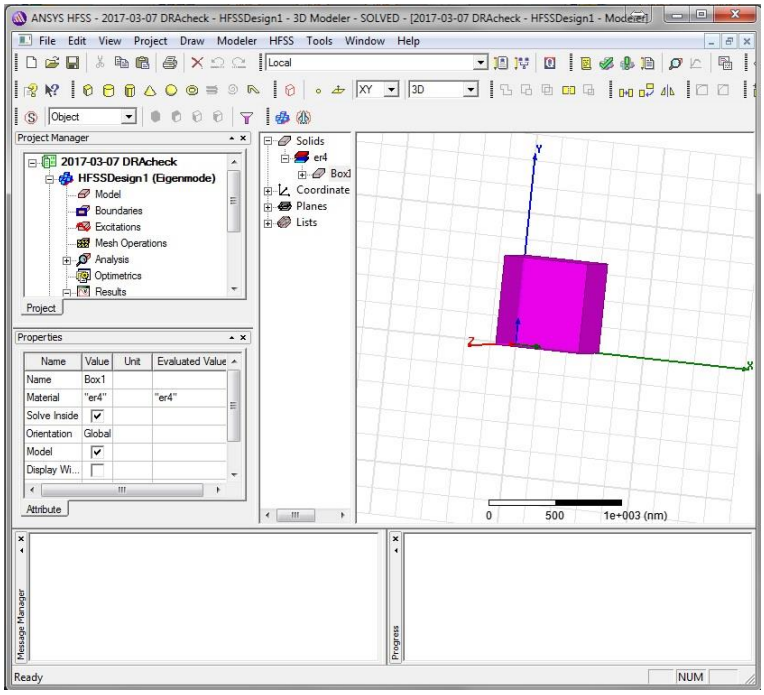

(c)

Figure 2.1: User interfaces for a) CST Microwave Studios, b) MATLAB and c) ANSYS HFSS.

Figure 2.1 illustrates the user interfaces for the simulation tools used in this work. Each software has its own parameters, which require careful settings to ensure that the correct assumptions are used leading to accurate results.

In CST, the Transient Solver has been used to obtain results across a fairly wide frequency range of 100-200 THz. In addition, a global mesh has been set at a density of 20, with an edge refinement factor of 20 for the plasmonic dipole. For improved convergence of results, the transient solver has been set to a maximum solver duration of 4000 pulses, compared to a default of 20 pulses. The “open (add space)” boundary has been utilized for the majority of our work unless mentioned otherwise. This simulates an antenna or resonant structure in free space surrounded by vacuum on all sides, which is most suitable for our proposed hybrid antenna with minimal interference from other factors.

2.1.3 Experimental data and Simulations

Originally, this work aimed to also fabricate a few of our optimized designs. However, fabrication facilities for designs at sub-nanometre lengths are not easily available at the university. An alternative form of verification is through the use of numerical simulation with parameters taken from experimental data. Simulations have therefore been carried out where possible for the assumptions in this dissertation but with the designs of the aforementioned publication as limiting cases for support. If the assumptions are sound, it should therefore lead to similar results as the experimental data, which would go a long way to supporting our results that use the same underlying assumptions, albeit with a different design. In addition, and as mentioned earlier, cross-verification has been implemented by comparing the results from FDTD numerical analysis, and CST, which uses FIT, as well as HFSS, which uses FEM.

2.2 Materials chosen

In the process of simulating the designs, it was necessary to select the materials to be used from a wide range of plasmonic and dielectric materials. When working with a design in the optical and plasmonic range, certain changes appear that do not necessarily occur at lower frequency ranges such as the microwave region. For example, metals are associated with negative permittivity and also have strong loss factors for electromagnetic waves travelling through them. Dielectric materials also have relative permittivities that vary based on the operating frequency. Two main materials will be used in the simulations in this work. The first is the material for the plasmonic dipole, which will be a plasmonic metal. The second is the material for the dielectric resonator cavity that will be utilized, which will be chosen from a range of dielectric materials. The ideal material for each application must first be specified to assess its effectivity and feasibility.

2.2.1 Material of the plasmonic dipole

The material for the plasmonic dipole must necessarily be a plasmonic metal. As was discussed in the previous chapter, it is the inherent behaviour of such metals that causes SPR when light is incident upon it. This behaviour occurs across the spectrum of plasmonic metals, however, they resonate at different frequencies and at different strengths. In order to identify which metal would be a good candidate for this dissertation, three commonly used plasmonic metals have been compared against each other. As a reference, a Perfect Electrical Conductor (PEC) material was also used to compare the plasmonic effect. PEC is a theoretical material that is useful in calculations and simulations to simplify the model. The underlying assumption is to have a material with perfect electrical conductivity but with the magnetic and dielectric characteristics of vacuum. In this particular work, the PEC would function as a metal with infinite electrical conductivity, with the understanding that it would generate the increase of the electric field due to antenna effects. This could then be compared to the increases caused by the plasmonic material , and any differences in the data would thus be attributed to plasmonic effects.

Figure 2.2 presents a simple metal sphere with a radius of 40nm and with an incident plane wave upon it. A probe was placed 1 nm away from the nano-sphere on the side facing the incident plane wave. This records the electric field on the surface of the sphere. As discussed in Chapter 1, a common parameter for measuring the strength of plasmonic effects is the Near-Field Intensity Enhancement (NFIE), which is proportional to the square of the electric field enhancement, E^2. The NFIE for copper, gold and silver have been investigated.

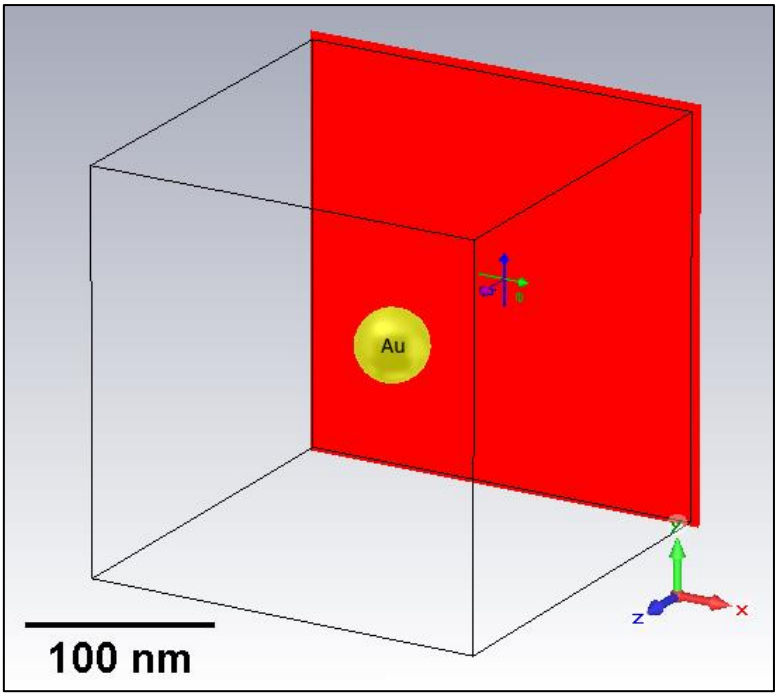

Figure 2.2: Nano-sphere excited by an incident plane wave

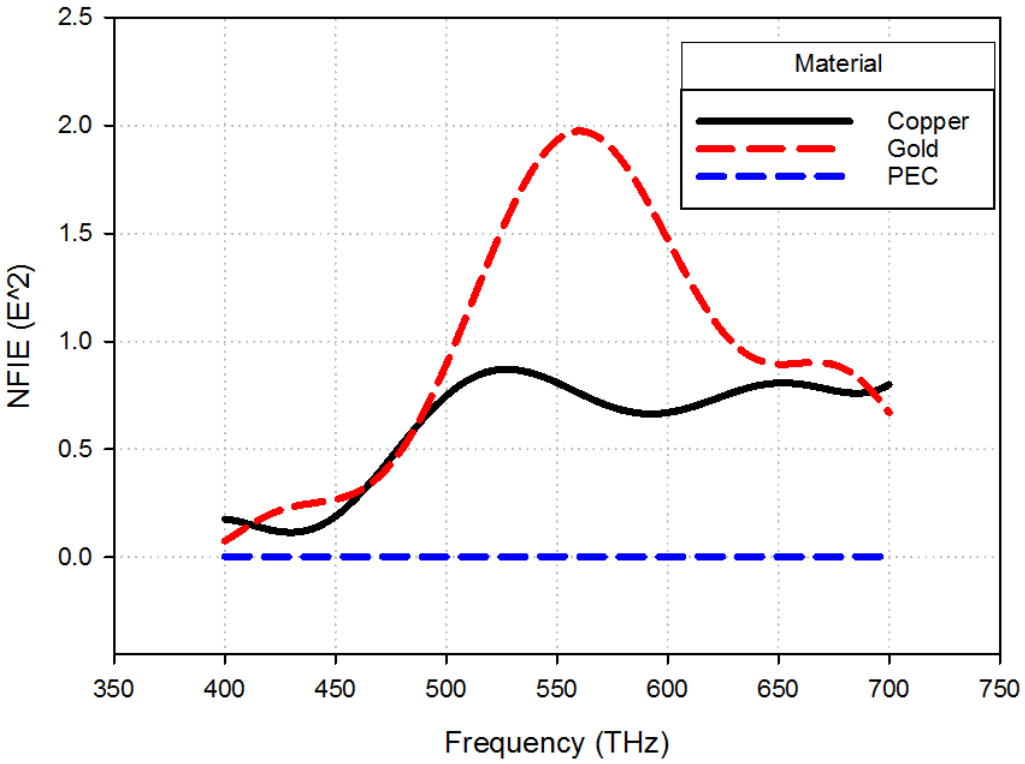

Figure 2.3: NFIE for a nano-sphere of radius 40nm made from PEC, Copper, and Gold.

Figure 2.3 shows the results of the CST simulation for PEC, copper and gold. The first result is for PEC, which is the reference. It can be seen that at such high frequencies and for such a small structure, the incident plane wave generates an extremely small NFIE. This is easily understood due to the subwavelength size of the nano-sphere. At 550 THz, the wavelength of the incident plane wave is ~550nm which is 10 times larger than the nano-sphere at a diameter of 80nm. Normally, an antenna would have to have a length of at least half-wavelength to be resonant with an incident electromagnetic wave. To further show that the plasmonic effect is valid for copper and gold, the use of copper causes a significant difference in NFIE. This readily proves that the plasmonic effect of the material is observed in the simulation. However, the use of gold increases the NFIE further and doubles it. This is a phenomenon that has been widely noted by other researchers who have also found gold to have a much stronger plasmonic effect compared to other metals except silver. The resonant frequency for gold is also consistent with known literature [7] which places the plasmonic frequency of gold at ~550 THz when in a vacuum.

Table 2.4 shows some values for bulk plasmon energy (plasma frequency), $\hbar\omega_p$, and surface plasmon energy [73][74] of some materials in this dissertation. The bulk plasmon energy is a required parameter to model materials as discussed later under heading 2.2.2. However, it is a mistake to consider this as the frequency at which Surface Plasmon Resonance (SPR) occurs, as bulk plasmons occur for longitudinal electron oscillations in the bulk of an electron gas or plasma. Surface plasmons however occur at the interface of two materials, and usually have lower energy than the bulk plasmons. An example from Table 2.4 shows that although gold has a bulk plasmon energy of 9.03 eV, which is equivalent to ~2200 THz, its surface plasmon energy is only 2.38 eV or ~550 THz.

Table 2.4: Plasma Frequency Values [73][74]

Material	**Bulk plasmon energy, $\hbar\omega_p$ (eV)**	**Surface plasmon energy, $\hbar\omega_s$ (eV)**
Gold (Au)	9.03	2.38
Silver (Ag)	9.01	3.10
Copper (Cu)	10.83	1.98
Gallium Arsenide (GaAs), Heavily n-doped	17.8	0.02481

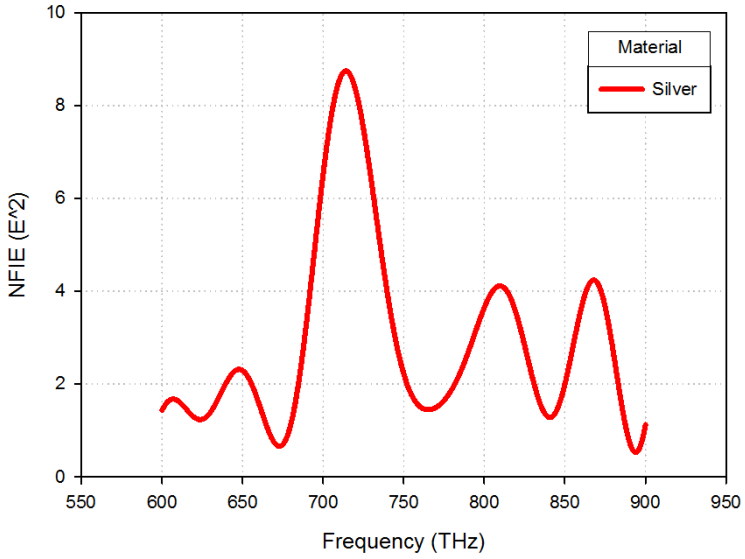

Figure 2.4: NFIE for a nanosphere of radius 40nm made from Silver.

Although gold is often used in literature, Figure 2.4 however demonstrates that plasmonic silver has a much higher NFIE compared to gold. This is further supported by identifying the transverse and longitudinal plasmon modes for gold and silver as shown in Table 2.4. This is still consistent with literature, which states that silver offers the strongest known plasmonic effect among the various metals [7]. The plasmonic resonance of silver

is also consistent with literature, which places it at ~730 THz or at a wavelength of ~450nm. However, Moore and Kuzma argue that although silver has a strong plasmonic property, it has issues in use due to the oxidation of pure silver, also known as tarnishing [75], [76], which reduces the plasmonic response of silver over time. In real-world applications of a plasmonic silver antenna, the exposure to air would cause oxidation of the metal surface, which would quickly reduce the plasmonic effects. Scholars have therefore widely agreed upon using gold as the most common plasmonic antenna metal due to its high NFIE properties combined with a stable constitution with a slow oxidation rate. Gold plasmonic antennas are therefore suitable to be used in various real-world applications and have become the industry standard.

Table 2.5: Plasmonic modes of Silver and Gold

	Transverse plasmonic mode (THz)	Longitudinal plasmonic modes (THz)				
Material		Multipole 1	Multipole 2	Multipole 3	Multipole 4	Reference
Gold dipole	565	165	215	310	385	[77]
Silver Coupled Sphere	730	200	400	545	625	[78]
Gold Coupled Sphere	565	190	375	500	545	[78]

Although the transverse plasmonic mode of gold is found at around 565 THz, it is noted that the first multipole of the longitudinal multipole mode is found at circa 165 THz. This multipole mode has the potential to generate a Third Harmonic Generation (THG) of ~500 THz that has applications in certain situations. This work focuses on the first longitudinal multipole and will collect data at these frequencies.

Once we have determined gold as the material for our plasmonic antenna, it is still necessary to describe the plasmonic behaviour of gold in our simulation program. There are a number of gold models which have been proposed by various scholars and the next step is to choose among them for an accurate model for our needs.

2.2.2 Material model for plasmonic dipole

In order to describe the plasmonic behaviour of gold, a number of models have been proposed that vary in terms of speed and accuracy. The complete complex dielectric function for metals and surface plasma can be expressed by separating the interband effects for the bound electron model and the intraband effects for the free electron behaviour [79]. This can be expressed through the general equations of:

$$\varepsilon_r(\omega) = \varepsilon_r^f(\omega) + \varepsilon_r^b(\omega) \tag{2.1}$$

$$\varepsilon_r^f(\omega) = 1 + \frac{\Omega_p^2}{j\omega\Gamma_0 - \omega^2} \tag{2.2}$$

$$\varepsilon_r^b(\omega) = \sum_{m=1}^{M} \frac{\Omega_p^2}{\omega_m^2 - \omega^2 + j\omega\Gamma_m} \tag{2.3}$$

where ε_r^f describes the effects of modelling the behaviour of electrons as free electrons floating in a cloud, similar to plasma, while ε_r^b models the behaviour of electrons as if bound to the metal molecules. As discussed in Chapter 1, the interband effects dominate at lower frequencies, thus simulating gold as a bulk metal of certain permittivity, while at optical frequencies, the intraband effects dominate, which makes metals gain the property of negative permittivity. The simplest model is the Drude model that approximates the behaviour of metal at optical frequencies by approximating the intraband effects, which is arguably the more dominant phenomenon at these frequencies [80].

$$\varepsilon_{Drude}(\omega) = \varepsilon(\infty) - \frac{f_0\omega_p^2}{\omega(\omega - i\Gamma)} \quad (2.4)$$

where $\varepsilon(\infty)$, f_0, ωp, and Γ are the relative dielectric constant at very high frequencies, oscillator strength (weight factor), plasma frequency and scattering frequency, respectively. Equation 2.4 is the generic Drude model and approximates the dispersion properties of metals. It has the advantage of being relatively simple compared to other models that will be mentioned shortly. However, it has limitations in terms of accuracy since the plasma frequency only takes into account the intraband transitions where electron behaviour is modelled as being free within a cloud of plasma. It is mainly used as a tool to approximate solutions, which must be verified again using alternative methods. Due to these limitations, the Drude model was expanded further by Lorentz into the Drude-Lorentz model which adopts some intricacies of the plasmonic behaviour of metals at optical frequencies.

$$\varepsilon_{D-L}(\omega) = \varepsilon_{Drude}(\omega) + \sum_{j=1}^{k} \frac{f_j\omega_j^2}{(\omega_j^2 - \omega^2) + i\omega\Gamma_j} \quad (2.5)$$

Equation 2.5 shows the Drude-Lorentz model, which incorporates the separated interband expression, which models the behaviour of electrons as being bound to the metal. The terms ω_j, Γ_j, k and f_j refer to the oscillator resonant frequency, damping factor, number of oscillators, and the oscillator strength, respectively. The oscillator in this case refers to the oscillating electrons and the oscillator strength is a dimensionless quantity for the probability of absorption or emission of radiation due to energy-band transitions. The expansion to include these Lorentzian terms increases the accuracy of the simulated behaviour but at the same time increases computation times. Some scholars in an effort to reduce the simulation time have only introduced 1 or 2 Lorentzian terms, which can speed things up at the cost of minor loss in accuracy. Others have increased k to 4 or more Lorentzian terms to increase accuracy at the cost of computation time. Although the Drude-

Lorentz model is more accurate than the Drude model, it still has some lapses in accuracy. Some have argued that the Drude-Lorentz does not accurately depict the interband absorption for noble metals in the plasmonic frequency range even when using up to five Lorentzian terms [79]. Another interpretation of the Drude-Lorentz model gives rise to the multi-oscillator model which is described by,

$$\varepsilon_{M-O}(\omega) = \varepsilon(\infty) - \frac{\omega f_0 \omega_p^2 - i f_0 \omega_p^2 \Gamma}{\omega(\omega^2 + \Gamma_0^2)} + \sum_{j=1}^{k} \frac{f_j \omega_{pj}^2 \left(-\omega^2 + \omega_{pj}^2\right) + i\omega f_j \Gamma_j \omega_{pj}^2}{\omega^2 \Gamma_j^2 + (-\omega^2 + \omega_{pj}^2)^2} \tag{2.6}$$

Equation 2.6 shows the multi-oscillator Drude-Lorentz model which extends the validity range of the equation through the addition of different interband terms. However, it is more interesting to focus on a different model such as the Brendel-Bormann model [79];

$$\varepsilon_{B-B}(\omega) = \varepsilon(\infty) - \frac{f_0 \omega_p^2}{\omega(\omega - i\Gamma_0)} + \sum_{j=1}^{k} \mathcal{X}_j(\omega) \tag{2.7}$$

$$\mathcal{X}_j(\omega) = \frac{1}{\sqrt{2\pi\sigma_j}} \int_{-\infty}^{+\infty} exp\left[-\frac{(x-\omega_j)^2}{2\sigma_j^2}\right] \times \frac{f_j \omega_p^2}{(x^2 - \omega^2) + i\omega\Gamma_j} dx \tag{2.8}$$

Equation 2.7 demonstrates that the Brendel-Bormann (B-B) model retains some of the multi-oscillator Drude-Lorentz model, but adds a Gaussian complex error method in the polynomial *Xj* (Equation 2.8) to reduce some of the errors from the Lorentzian terms. This method has been proposed by Brendel and Bormann, which reduces the deviance of the Drude models from the actual values. The final term is therefore replaced with the B-B polynomial, *Xj*.

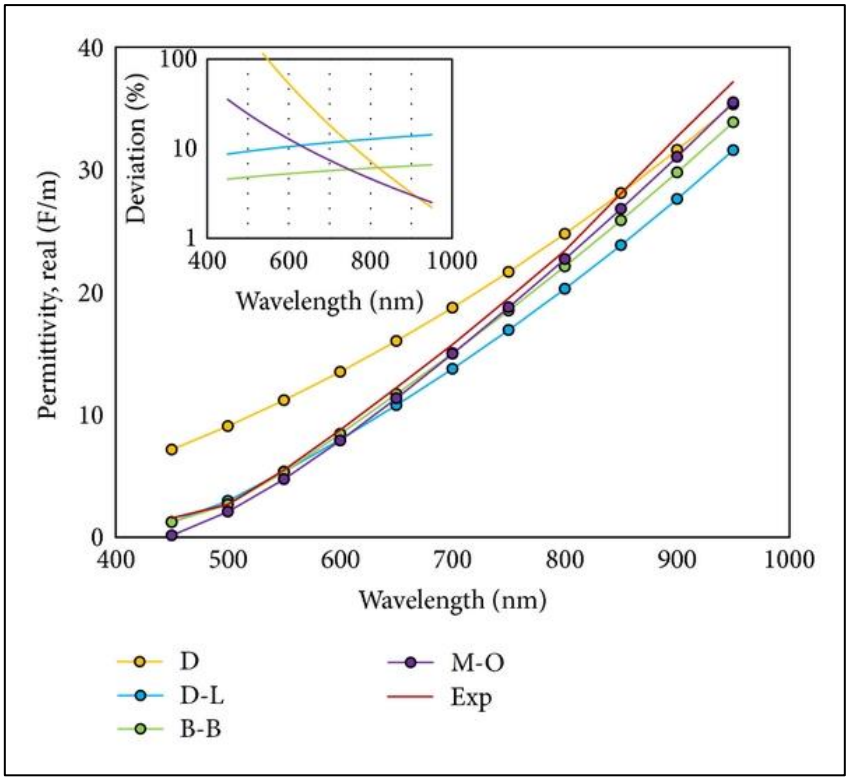

Figure 2.5: Real part of permittivity (F/m) against wavelength (nm) for all four models compared to experimental data. Inset: error value of the permittivity against wavelength indicating the accuracy of the B-B model with less than 10% deviation. [80]

Figure 2.5 displays the results of [80] which compares the accuracy of the B-B model against the other models mentioned above. It was found that the B-B model had strong fit to experimental data.

The most accurate models of all are those that are based on experimental data. Johnson & Christy proposed one of the most commonly used sets of data for plasmonic metals in one of the well-known sets of data used by researchers [81]. They recorded the behaviour of plasmonic metals between 150 THz to 1600 THz. An alternative and well known set of data was recorded by Palik et al., which updated the data found by Johnson & Christy and is valid between 150 THz to 3000 THz [82]. However, Rakic et al has demonstrated that the Brendel-Bormann model could be fitted to experimental data

reported by J& C and Palik. This has given an extremely accurate model for the range of 100– 2000 THz.

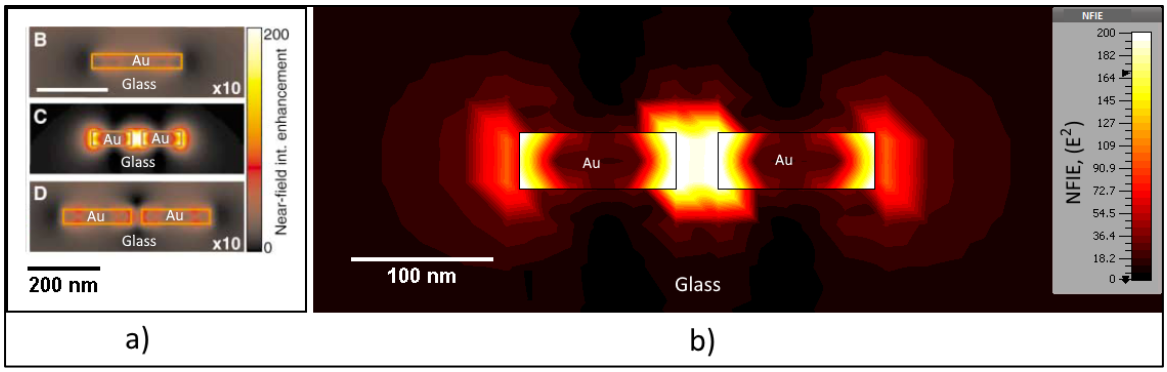

Figure 2.6: Diagram of NFIE results for a dipole antenna on glass substrate for a) a published journal [83] and b) duplicated simulation.

In order to verify the accuracy of this model, the parameters of a journal paper [83] were reproduced, and the generated data have been compared against the experimental results in the paper. A gold dipole with arm dimensions of 110x40x40 nm has been simulated when positioned above a glass substrate with a relative permittivity of $\varepsilon_r = 2.25$. The gap size is set to 30nm and a probe is placed in the centre of the gap, 10nm above the antenna, or 50nm above the substrate surface. The journal paper presents experimental results of NFIE in the order of ~200 V^2/m^2 at a resonance frequency of 361THz. Simulating the same design using CST Microwave studio with a substrate of relative permittivity 2.25 and utilizing the B-B model for gold, yields an NFIE of ~225 V^2/m^2 at a resonance frequency of 351 THz as displayed in Figure 2.6. The results are close in terms of resonance frequency and NFIE. The discrepancies can be easily explained due to the use of a lossless substrate in the simulations and the imperfect lines in the fabricated dipole. A real-world lossy substrate would slightly lower the resultant NFIE leading to the result found in the experimental data and small errors in fabrication and surface roughness would also shift

the frequency and reduce the NFIE. This supports the choice of model and the Brendel-Bormann model has been used for the simulations in this dissertation. In order to corroborate the results, a numerical simulation was also conducted in Chapter 5.

The numerical simulation in Chapter 5 was then carried out utilizing FDTD and a Brendel-Bormann material model of gold. Specifically, the calculated parameters from [79] were used, which are listed in Appendix B and plotted in Figure 2.7.

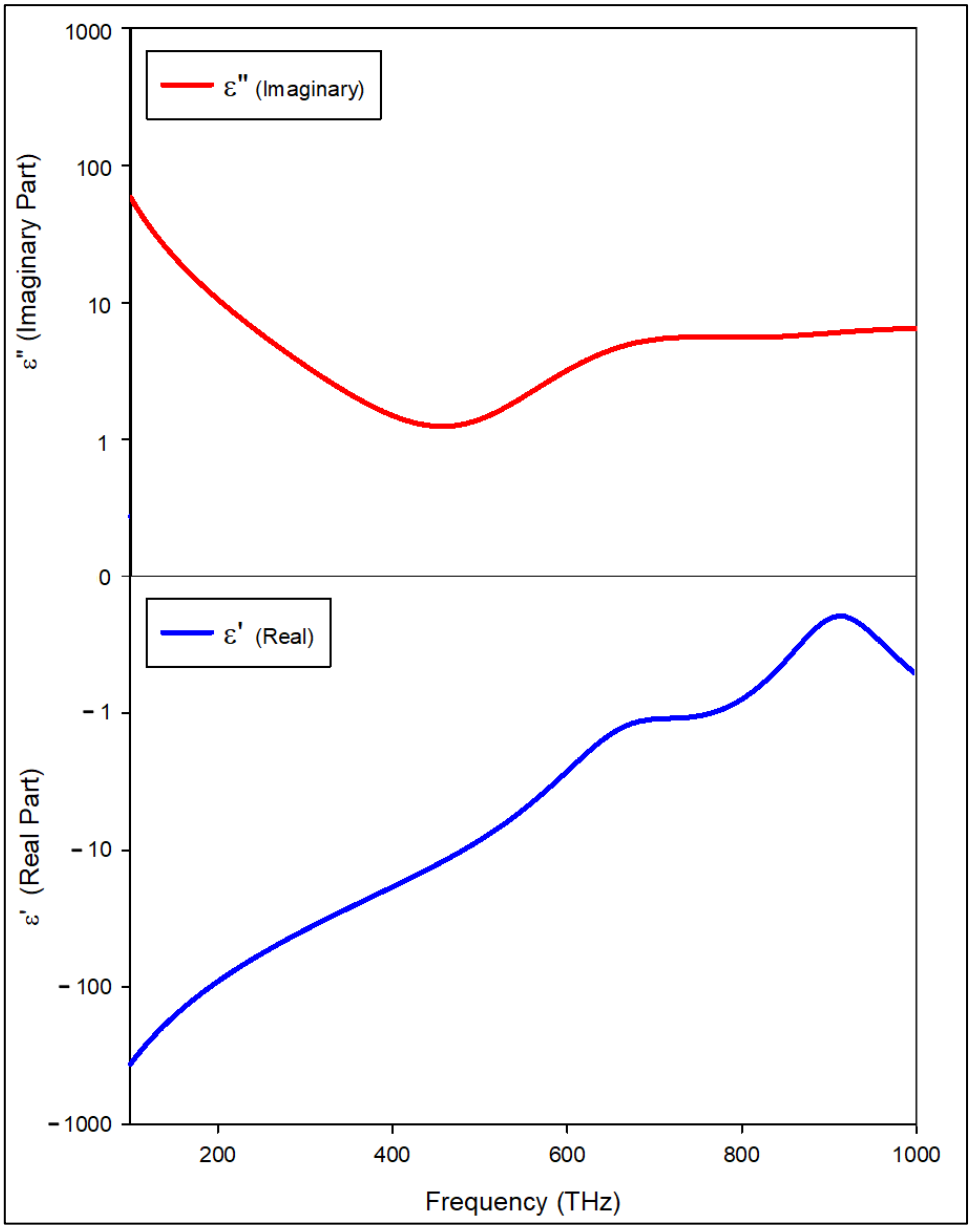

Figure 2.7: Complex Permittivity of Gold

2.2.2.1 **Creating the gold material model in FDTD**

In the code for the numerical simulation utilizing FDTD in MEEP, it is possible to define a realistic model for metals as well as other conductive materials. A material model can be defined using four different methods that applies the models discussed in the past few pages.

1) The Perfect Electric Conductor (PEC) – In a PEC, an ideal metal is simulated where the E field in the material is always zero. All electromagnetic waves are allowed to pass through the material with infinite electrical conductivity (and therefore no resistance or electrical damping) and infinite permittivity. The metal can also act as a perfect ground plane with no reflection losses. PEC can be utilized as a sufficient approximation for the majority of non-resonant bulk metallic structures.

2) The Drude model (Lossless) – The Drude model emulates the behaviour of the metal by assuming the charges to have a mass. At a frequency above a predetermined *plasma frequency* (related to their mass and concentration), the charges are not fast enough to compensate the electric field and the wave starts to propagate through the metal, making it dispersive and allowing the permittivity to vary between 0 and 1. However, at far below the plasma frequency, the material behaves similarly to PEC except that the permittivity is a finite complex function diverging at low frequencies. Losses can be ignored as the incident wave creates an exponentially decaying field just below the surface and all energy is reflected, or the EM field propagates through the metal. This model was discussed in more detail previously at Equation 2.4.

3) The Drude model (Lossy) – The lossy version of the Drude model still takes into account the charge mass but adds a finite scattering time for the moving charges. This

model also considers the finite conductivity of metals at low frequency. This model was discussed in more detail previously at Equation 2.4.

4) The Drude-Lorentz model (Lossy) – A modified Drude-Lorentz model is the one utilized in the numerical simulation in this paper. This model improves upon the Drude model by taking into account the interband transitions of noble metals, which can increase the accuracy of simulations in the optical range. This model was discussed in more detail previously at Equation 2.5.

The Drude-Lorentz model can be simulated numerically by first including the Drude component as a Lorentz resonance at an extremely low frequency. The strength of the oscillator is then given a value. The curves for a lossy Drude-Lorentz model should bend at a scattering frequency. Below this scattering frequency, the bulk metal behaves as a resistive medium, whereas above that frequency it behaves more as an inductive medium, while still being highly reflective. The scattering frequency usually lies between 3-30 THz in most metals, with the scattering frequency for gold at ~17 THz.

The model for gold was obtained from [79] and listed in Appendix B. It can be further verified by calculating the optical reflectivity and comparing it with experimental data as done in literature. In general, it shows that the values are quite accurate in the NIR and visible range but has some inaccuracies as the frequency increases into the UV range.

2.2.2.2 **Stability of simulation**

For the simulation to be numerically stable, it is important to calculate the **critical frequency = $1/(\Delta t*\pi) = c/(\Delta x*S*\pi)$**, where Δx is the resolution and c is the speed of light. The Courant factor, S, as a default is set to 0.5 in MEEP (MIT Electromagnetic Equation Propagation simulation framework). For example, at a resolution of Δx = 50 nm, we get the **critical frequency** in the UV region: $3x10^{8}/(5x10^{-8}*0.5*3.14)$ = 3820 THz. When

utilizing the MEEP simulation framework, it can be observed that three conditions are needed for stability of the simulation:

1. The permittivity must be positive at the *critical frequency* and above.

2. A Lorentzian oscillator cannot be defined above the *critical frequency*. To avoid any issues, no Lorentzian oscillators should be defined at any value more than 0.75 of the critical frequency. For a critical frequency of 1000 THz, no Lorentzian oscillators should be defined above 750 THz.

3. In the geometry designed, there must be enough space between any resonator and any perfectly matched layers (PMLs).

The first and second conditions are reasonably easy to fulfil when metals are not used. It is also easy to prevent instabilities for simulations in the near-infrared or optical range, as a high resolution is often used anyway. Then the **critical frequency** lies somewhere in the far UV region where all materials have a permittivity close to one. Problematic cases can typically occur when computing the behaviour of metallic structures in the microwave or far-infrared region. The structure would have at least the size of a free-space wavelength, so it is not feasible to use the nanometric resolution. Instead, the Lossy Drude model can be modified for the metal so that the simulation will be stable even at relatively low resolution (large mesh size), of less than 5 unit cells per wavelength [84]. However, this work will focus in the Near Infrared (NIR) region and the simulations should be numerically stable.

2.2.3 Material of the dielectric resonator cavity

A considerable amount of research have reported the effects of the plasmonic antenna designs on NFIE, where certain designs can direct the plasmonic field and increase

the NFIE [17], [85], [86]. However, the influence of utilizing a dielectric cavity as a substrate and/or superstrate have not been explored as fully. These mentioned papers have touched upon the issue and discussed how the permittivity of the substrate to a plasmonic metal can significantly affect the plasmonic response due to the sensitivity of SPR. Yu-Ming reported that changing the substrate thickness also had an effect on the NFIE of a bowtie antenna that is placed upon a silicon substrate [17]. However, this has not been explored further and merely noted as a possible future work.

In the next chapter, the effects of truncating the supporting substrate so that it acts as a dielectric cavity resonator will be investigated for the previously chosen gold dipole. This should theoretically affect the effective permittivity at the surface boundary of the hybrid structure and hence affect the NFIE. Optimizing the effect through several theories should then allow for an increased NFIE. Therefore, the dielectric material used has a strong effect on the results of the combined hybrid structure. In this section, attention is paid to choose a material that is both effective in terms of increasing NFIE as well as practical to physically support the plasmonic antenna at the required frequencies. Throughout this part of research, industry standard materials are used in order to ensure the practicality of the proposed design. These materials have the combined benefits of being easily sourced, have fully-fledged material models as well as being more easily fabricated as they are already integrated into the fabrication process. The structures designed in the later chapters have resonances in the range of 150 THz to 300 THz. Among the industry standard materials found at ~150 THz which will be later utilized are Silicon Dioxide (SiO2) with a refractive index of n=1.5, gallium arsenide (GaAs) with a refractive index of n=3.3, and Silicon Nitride (Si_3N_4,) with a refractive index of n=2.05. Different materials with different relative permittivities have been considered to illustrate their effects on

NFIE. A higher relative permittivity, ε_r, means that the effective length of the dielectric cavity increases, and thus smaller designs can be employed. However, the key aim of this study is to increase the NFIE and the various parameters are optimized with this objective while keeping in mind the feasibility of the final design.

Table 2.6: High frequency and static relative permittivities [87]

	Static relative permittivity (ε_0)	**High frequency relative permittivity (ε_∞)**
Vacuum	1	1
Silicon Dioxide	3.9	2.25
TiO2	85	8.29
GaP	11.11	9.11
Gallium arsenide (GaAs)	12.94	10.89
Silicon Nitiride (Si_3N_4)	7.5	4.2
InAs	15.16	12.25
GaSb	15.69	14.44
InSb	17.88	15.68

Table 2.6 presents a number of dielectric material candidates with relative permittivities of 1 to 20. It is well-known that at optical frequencies, dielectric materials behave differently compared to lower frequencies due to the frequency-dependent nature of permittivity. This is often reflected in the terms static dielectric constant, $\varepsilon(0)$, and high-frequency dielectric constant, $\varepsilon(\infty)$. Although termed as such, in truth the dielectric constant, also known as the relative permittivity, is always variable based on the temperature and frequency. At lower frequencies, the permittivity is static enough that it can be stated as a single value and termed the "static dielectric constant". However, at higher frequencies, the real permittivity tends to go much lower. One example is the perovskite-related oxide, $CaCu_3Ti_4O_{12}$, which has a permittivity of ~10^5 at the kilohertz

range but has a permittivity of ~80 in the low infrared region [88]. This phenomenon can also be explained through the use of the Debye equations, which govern the dielectric permittivity behaviour.

In 1913, Debye described a relaxation model for phonons reacting to an external electric field. This was described in terms of relative permittivity as a function of frequency, which is encapsulated in the following Debye equations:

$$Re\big(\varepsilon_r(\omega)\big) = \varepsilon_r(\infty) + \frac{\varepsilon_r(0)-\varepsilon_r(\infty)}{1+\omega^2\tau^2} \tag{2.9}$$

$$Im\big(\varepsilon_r(\omega)\big) = \omega\tau\frac{\varepsilon_r(0)-\varepsilon_r(\infty)}{1+\omega^2\tau^2} \tag{2.10}$$

Equations 2.9 and 2.10 above describe the real and imaginary parts of the complex relative permittivity. The equations are both highly dependent on the frequency and describe that the imaginary part has a resonance, but the real aspect has a steady decline as frequency increases. At the same time, high permittivity semiconductors at optical frequencies have fundamental limitations due to the effect of interband transitions of electrons, which absorbs the energy of the incident light [89]–[91]. This absorption reduces the quality factor and even leads to increased heating of the material, which is contrary to the purpose of using such materials in the first place. This leads to the conclusion that a lower relative permittivity would have advantages for the proposed designs. However, a relative permittivity that is too low will lead to much larger dielectric cavities to get the same effective length of the dielectric material. A balance must be achieved to get a dielectric cavity that has a strong enough NFIE at our target frequency, while still keeping the relative permittivity as low as possible. As a result, simulations have been carried out for relative permittivities up to 50 for dielectric materials operating in the optical frequency range.

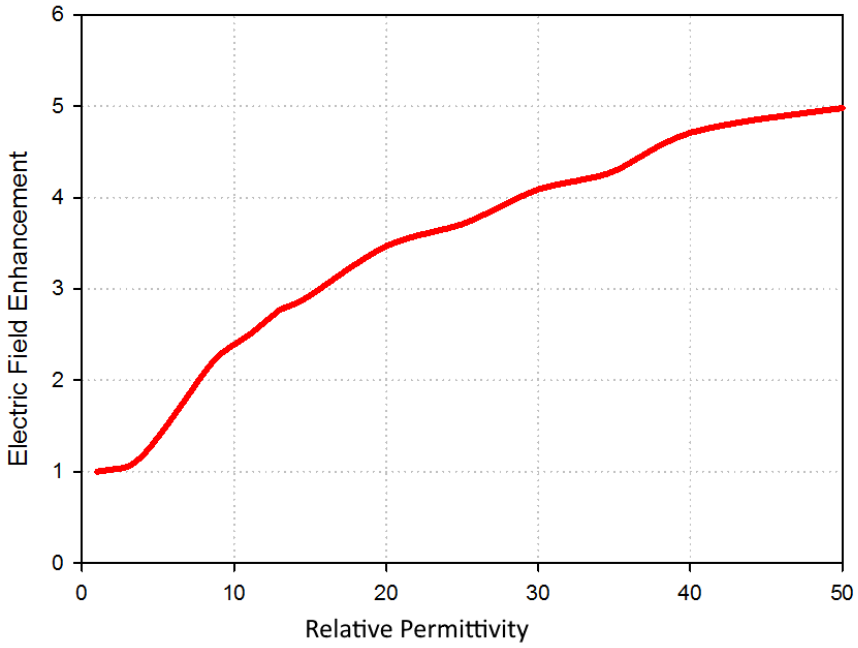

Figure 2.8: Increase of electric field enhancement across various dielectric constants

A dielectric substrate has been simulated with the respective length, width, and height of 1200, 1200, and 50nm. A plane wave has been induced upon the structure and the maximum NFIE on the surface has been monitored for each relative permittivity over a frequency range of 100-300 THz. Figure 2.8 displays the changes in the electric field as a function of relative permittivity variations. It is observed that the electric field increases as the relative permittivity increases in a roughly linear fashion. Further data can be found in Appendix E. A relative permittivity of 10 - 20 is found to be ideal for maximum NFIE while still being limited by readily available optical dielectric materials.

One dielectric material that is commonly used for optical applications is gallium arsenide (GaAs) with a relative permittivity of 12.94 at microwave frequencies and ~11 at optical frequencies. This has been chosen as our main material for the dielectric cavity. It is both readily available as an industry standard and also available as a simulation model in CST, which allows for more accurate results. It was important to select this substrate as

opposed to the Silicon Dioxide substrates used in some other works, as this work will design a dielectric nanocavity, which requires a high degree of isolation. Therefore, a high index is necessary to increase the efficiency of the cavity and ensure that as little light as possible is allowed to escape. GaAs has also been successfully used as a substrate by [92] for gold plasmon effects. Therefore, it should be an acceptable choice for this dissertation.

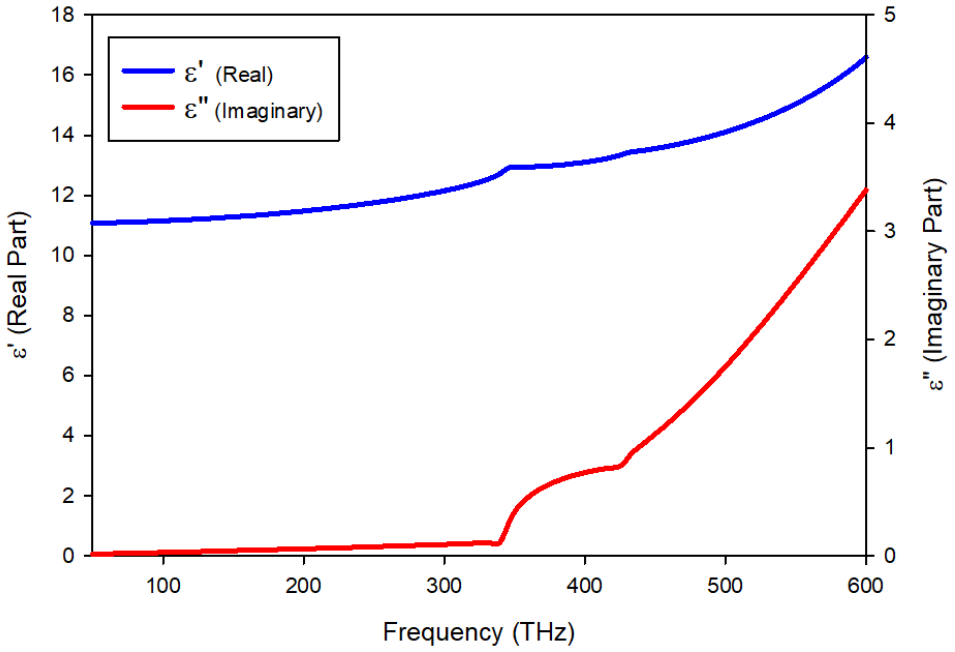

Figure 2.9: Complex permittivity of Gallium Arsenide

The data used to model the complex permittivity of GaAs is taken from the Adachi model [93] and is plotted out in Figure 2.9. Further data can be found in tabular form in Appendix C.

2.3 Designs and dimensions

2.3.1 Plasmonic antenna

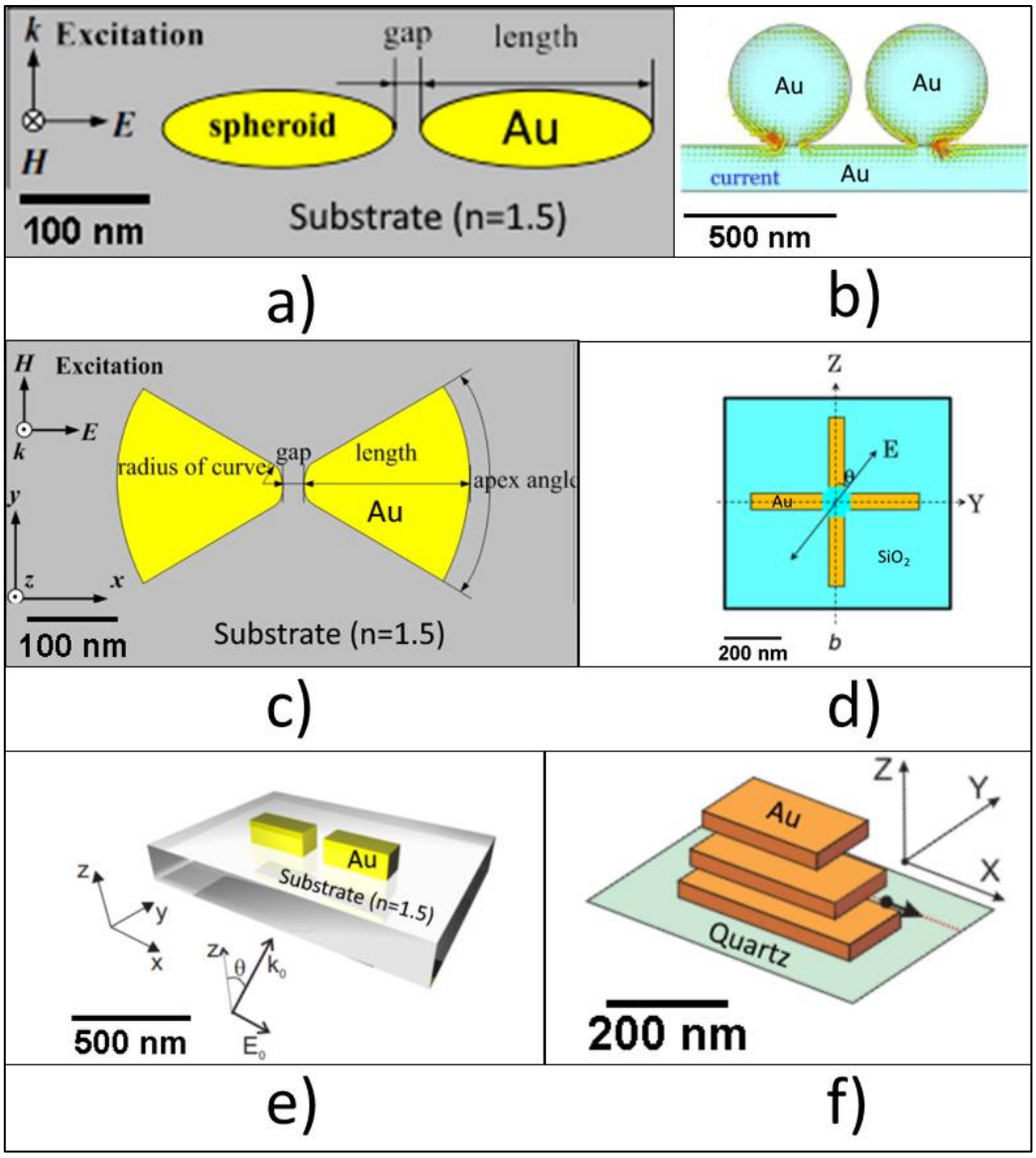

Figure 2.10: Examples of published designs for plasmonic antennas for a) coupled spheroid [17], b) coupled sphere [38], c) bowtie [41], d) crossed dipole [42], e) dipole [94], and f) Yagi-Uda [39] designs.

Figure 2.10 illustrates examples of published plasmonic antenna designs in current literature. Most of these designs have been the product of transplanting microwave antenna designs and exploring their behaviour when scaled down to the optical regime. They mostly

explore the effect of nanoantenna design on the NFIE. The results confirm the principles explained in Chapter 1. At optical frequencies, a few different effects come into play that may serve to increase the NFIE of a plasmonic antenna. The results from literature are shown in Table 2.7.

Table 2.7: Results of various plasmonic designs in the literature

Design	**Max Enh (V/m)**	**NFIE (V^2/m^2)**	**Simulation /Experiment**	**Wavelength (nm)**	**Notes**	**Source**
Coupled Sphere on Gold Slab	170	28.9k	Simulation	3000	10nm gap	[38]
Bowtie on silica	60	3600	Simulation	1200		[40]
Bowtie Aperture	7	49	Simulation	630		[40]
Crossed dipole	14	196	Simulation	1200		[42]
Dipole over gold layer	70	4900	Numerical (FDTD)	785		[46]
Dipole	30	900	Experimental	900	10nm gap	[37]
Gold Nanorod	22	500	Experimental	6000	2000nm antenna length	[47]
Coupled gold sphere on silver grating	40	1600	Experimental	N/A	5nm gap	[48]
Yagi-uda Array	16	256	Numerical	1500		[39]
Nanosphere array	50	2500	Experimental	1000		[49]
Nanosphere array	1300	1.69×10^6	Numerical	380	Gap less than 2nm	[51]
Coupled Dimer array in Fabry-Perot cavity	9×10^6	8.1×10^{13}	Numerical	N/A	Fabry-Perot cavity	[43]

Table 2.7 demonstrates that the resonance of a simple dipole nanoantenna can yield a maximum NFIE of ~900 V^2/m^2 for a gap size of 10nm when considering no other sources of enhancement other than the dipole. The work of each source has been discussed in more detail in Chapter 1 and has summarized how scholars have gained improved intensity enhancements using different antenna designs. When including simulation and numerical analysis, NFIE results of up to 8.1 $x10^{13}$ V^2/m^2 have been published. However, when only experimental results are considered, the reported value falls drastically to around ~2500 V^2/m^2. Numerical and simulation results should still be considered, but in conjunction with certain assumptions. For example, the second final entry lists a nanosphere array using numerical simulation to calculate a significant NFIE increase with a gap size less than 2nm, which is not always feasible, and does not take into account the damping effects for very small gap sizes that were discussed in Chapter 1. Chapter 1 also discussed fabrication techniques and found that most of the techniques currently used have a resolution of ~10nm. Some fabrication techniques can have an even higher resolution of below 5nm, but only work on certain designs or may introduce high shot noise when the resolution is forced to below 10nm. The final entry in Table 2.7 lists a design utilizing a coupled sphere placed in a Fabry-Perot cavity which acts as a pump to supply a much stronger incident light on the plasmonic antenna. This design is calculated through numerical analysis which assumes perfect reflectivity to gain an extremely high Fabry-Perot enhancement. The Fabry-Perot design is not mutually exclusive from this dissertation and will be included in Chapter 4 after a dielectric cavity is optimized in Chapter 3. The effects of reduced gap size and use of Fabry-Perot cavities will be investigated in Chapter 3 and 4 respectively. A complete analysis of the antenna designs shows that when the gap size is maintained at or above 10nm and no Fabry-Perot cavities are used, the strongest recorded NFIE is 28.9k.

The effects contributing towards increased NFIE were discussed in chapter 1 and considered when evaluating the ideal antenna design for this dissertation. Although a bowtie showed the strongest results, in the end a dipole was chosen as it had a high NFIE due to coupling and the longitudinal plasmon resonance, but still embodied simplicity and could be used for easy comparisons against published data where a large number of publications use dipoles. In terms of dimensions, a working frequency of ~150 THz with arm lengths of circa ~100nm is feasible based on experimental data from published journals [83].

2.3.2 Dielectric cavity

Previous works by Yu-Ming have shown that the thickness of a dielectric substrate can strongly affect the NFIE [85]. The NFIE for a plasmonic dipole was investigated for a variety of substrate thicknesses, starting at a thickness of 50nm to 200nm. NFIE increases were found as the substrate thickness was increased but the reason behind the phenomenon was left unanswered as a future work. Other scholars have utilized a dielectric material as a superstrate rather than substrate and results have shown that the presence and refractive index of the dielectric material can drastically affect the results in terms of NFIE [86], [95]. The dielectric superstrate was theorized to act as a lens that could focus the plane wave to a certain extent. This behaviour however cannot explain the effect of a substrate on NFIE since the substrate would be at the other end of the incident plane wave but can still increase the NFIE.

This work therefore explores how the substrate can increase NFIE in the next chapter, Chapter 3. The thickness of the substrate is optimized, and the width and length of the substrate are truncated to form a cavity and optimized between 500 × 500 nm to 2000 × 2000 nm. The optimum substrate/cavity dimensions are found and the theory behind it

explained further. Figure 2.11 illustrates the design of the dielectric cavity with a plane wave in the z-axis, shown by the purple arrow facing down, and a probe placed in the centre of the cavity surface, shown by the green crossed arrows.

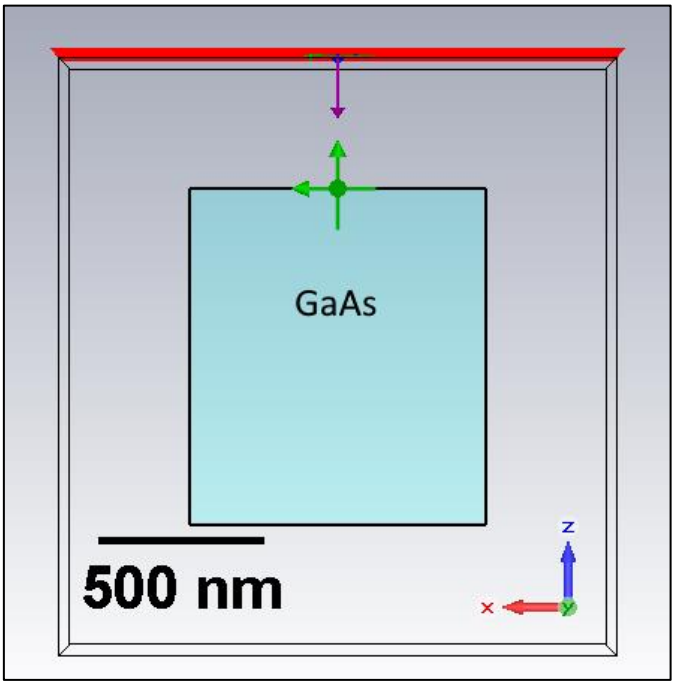

Figure 2.11: Dielectric cavity design with plane wave and probe.

2.4 Other considerations

To obtain the maximum resonance of the incident light on the plasmonic antenna, the incident light must be polarized to match the antenna polarization. Research in this field has overwhelmingly shown that the strongest plasmonic resonance is the longitudinal plasmonic resonance which is parallel with the long axis of the dipole [10], [23], [96]. To maximize the recorded NFIE, the electric-field of the incident plane wave is always placed parallel to the longest axis of the dipole nanoantenna.

The frequency range of the simulation is set between 100–200 THz based on the following reasons. The plasmonic response of gold is often quoted as 550 THz, or a

wavelength of 550nm, and most of the literature quotes results with resonance frequencies between 300–400THz, which occurs due to the frequency shift caused by the surrounding materials or substrate, where the substrate used typically has a relative permittivity of ε_r=2.25, or due to the effects of coupling or lengthened antenna. Chapter 1 described how lengthening a gold sphere into a spheroidal shape decreases the resonance frequency and coupling two spheroids would effectively increase the antenna length thus reducing the resonance frequency further. The choice of GaAs as a substrate has significantly shifted this frequency from 300-400THz down to 100-200THz depending on the length of the antenna.

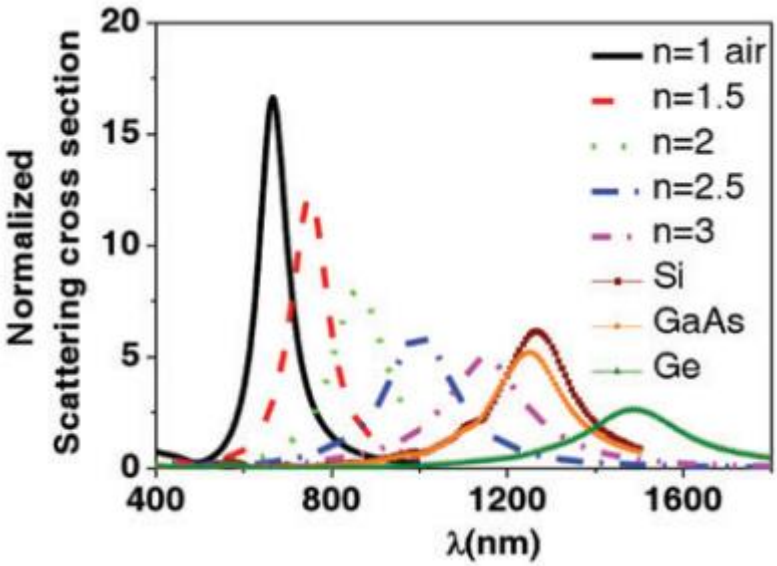

Figure 2.12: Resonance frequency and scattering cross-section of a coupled gold dimer antenna for different substrate refractive indices [97].

Figure 2.12 illustrates how the introduction of a substrate of various permittivity can shift the resonant wavelength higher, which means that the resonant frequency is lowered. The quality factor of the resonance is also affected, and the increasing permittivity spreads the resonance peak over a larger bandwidth, thus reducing the quality factor.

2.5 Conclusion

Chapter 2 has identified the methods used in this dissertation to design, simulate and optimize plasmonic antennas with strong NFIE. FDTD has been chosen as a method of numerical analysis, wherein some code has been created to automate the calculations involved. The generated results from numerical analysis would then be compared against commercial electromagnetic solver software. The software decided upon were MATLAB and CST, with HFSS used for occasional comparison. To simulate these designs in CST, gold was chosen for the plasmonic material and the Brendel-Bormann (B-B) model was used that gives more accurate results as compared to the commonly used Drude model. The B-B model was compared against published experimental data which proved its accuracy. The material for the dielectric structure was chosen as gallium arsenide which is commonly used at optical frequencies and has a relatively high relative permittivity at these frequencies and a material model based on experimental data was utilized.

Finally, although the bowtie design for a plasmonic antenna can yield higher NFIE, it makes for harder fabrication and is also not as commonly used in the literature which makes a dipole antenna a better benchmark. The data generated from the use of a dipole antenna can be more easily compared against a number of works in literature which reduces the possibility of error in our numerical analysis and simulations. Chapter 3 will continue by utilizing the assumptions laid out in Chapter 2 and designing an optimized structure with high NFIE.

(This page is intentionally left blank)

Chapter 3: Optimization of a Nanoantenna Above a Dielectric Resonator

In the previous chapter, a gold dipole plasmonic antenna has been chosen as a reference upon which improvements of NFIE have been investigated. As mentioned in the earlier, the potential of improving the NFIE by truncating the supporting substrate so that it acts as a dielectric cavity resonator will be investigated in depth. A number of parameters have been studied to maximize the NFIE and simulations have been carried out on each parameter to obtain the ideal settings. This combined structure is in the form of a **hybrid antenna**, with a gold plasmonic dipole placed on top of a dielectric cavity resonator.

The first part of the chapter is focused on the parameters of the dielectric cavity as well as how the cavity couples to the plasmonic metal. The parameters studied include the thickness, surface area and permittivity and are optimized to give a strong NFIE within certain limitations of frequency range and dimensions. Once the NFIE is optimized, the phenomenon is studied and explained based on antenna and plasmonic theories. A simpler method to determine the dielectric cavity dimensions is proposed and compared against published results. This represents one of the key contributions of this dissertation. The second part of the chapter optimizes the gold dipole placed on the dielectric cavity, which includes optimizing the dipole's arm length, type of metal, dipole thickness and gap size in-between the dipole arms. These parameters have been optimized and discussed in terms of their effects on the plasmonic resonance. The dielectric cavity has been coupled to the

dipole as both substrate and superstrate and the NFIE results have been studied. The dipole has also been replaced with a bowtie to show how other antenna designs can take advantage of the proposed dielectric cavity resonator as a substrate. Bowtie designs have also been compared against published results to determine the accuracy of the simulations. A maximum NFIE result of 37k has been achieved for a gold dipole on a dielectric resonating cavity compared to 88k for the bowtie antenna. This clearly indicates what sort of enhancement in the light intensity can be achieved by simply truncating the supporting substrate to act as a dielectric resonator cavity. It should be noted that the proposed configuration is much simpler and easier to fabricate compared to those reported in the literature with less light enhancement of the light intensity. The results have been compared against those published in current journal papers and the differences have been discussed.

3.1 Plasmonic resonance of a dipole

The plasmonic response of a dipole is first recorded on a square substrate with a width of 1000nm, thus having a surface area of 1000nm x 1000nm. This surface area places the dipole far enough from the edges of the substrate that the SPR of the dipole will not be greatly affected by the change in substrate permittivity. In this situation, the plasmonic response of the dipole is concentrated within a 20nm*20nm*20nm cube and a distance of 500nm to the edge of the substrate can be considered relatively large. This step is to find the resonant frequency of the dipole when placed at the boundary of two materials of different permittivities, namely gallium arsenide (GaAs) and vacuum. Figure 3.1 illustrates a nano-dipole with respective arm length and thickness of 90nm and 20nm that is placed on a gallium arsenide (GaAs) substrate with a thickness of 50nm. A plane wave has been used as an excitation source and an electric field probe has been placed in the centre of the dipole gap to measure the strongest point of resonance. The use of GaAs as a substrate also

tunes the resonant frequency of the dipole to a lower frequency compared to the plasmonic frequency of gold.

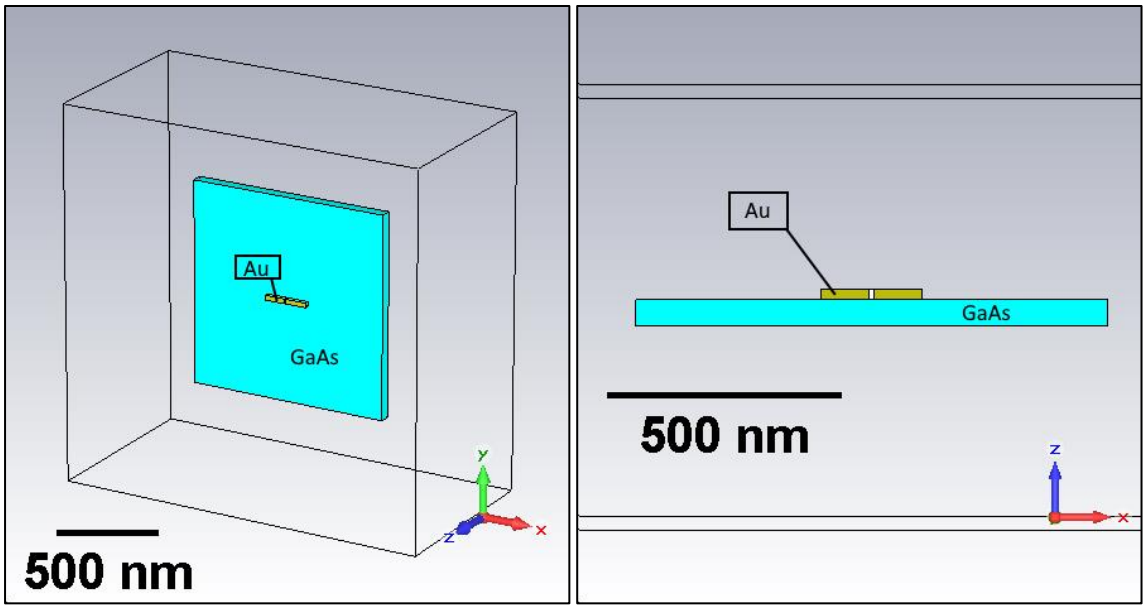

(a) (b)

Figure 3.1: A dipole above a dielectric substrate; (a) top view (b) side view.

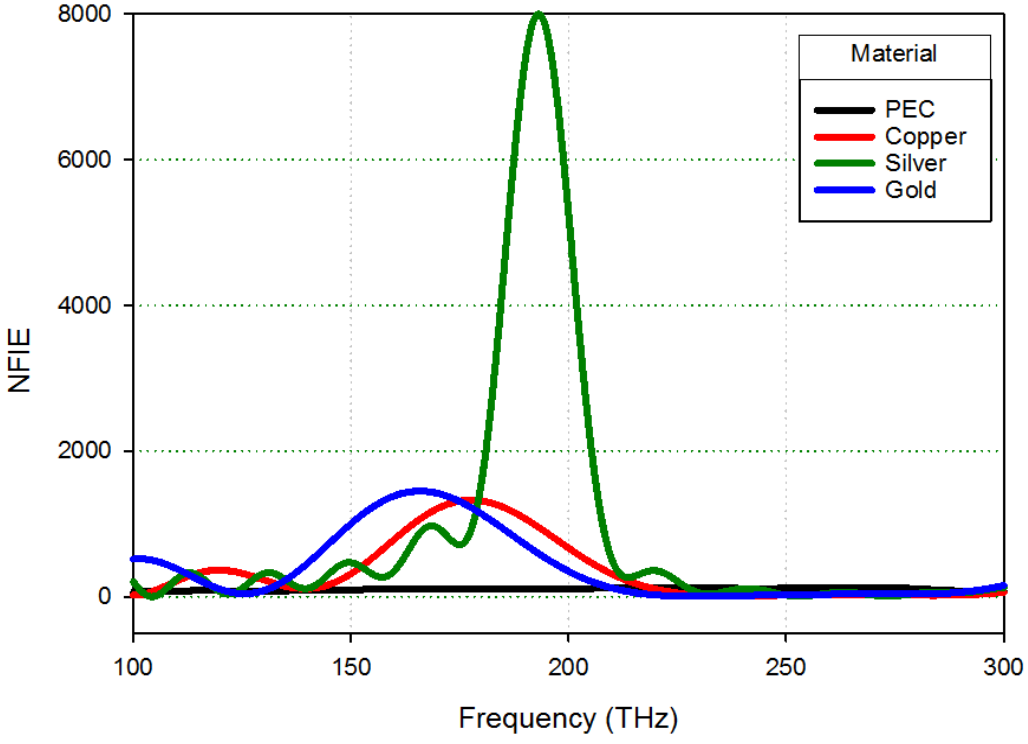

Figure 3.2: NFIE of a dipole of various metals on a 50nm thick GaAs substrate

To record the plasmon resonance and to verify that the recorded electric field is directly due to plasmonic resonance, a number of metals have been compared. In CST, material models for gold, copper and silver based on experimental data were imported and a model for a Perfect Electric Conductor (PEC) was also used. The PEC material has the useful property of being a perfect conductor while not having a plasmonic response. The use of PEC can therefore quickly differentiate any effects that may occur due to the plasmonic property of metal rather than conductive property of metal.

From Figure 3.2, it is clear that when PEC is used, the dipole gives an extremely weak NFIE of 125 V^2/m^2, where some intensity enhancement occurs, but which is entirely due to the antenna design absorbing a small part of the incident optical wave. On the other hand, replacing the PEC with gold or copper provides a significant NFIE improvement to ~1750 and ~1400 at the resonance frequencies of 165 and 177 THz, respectively. The strongest improvement has been attained through the utilization of silver, which increased the NFIE to ~8000. The use of silver over gold can drastically improve NFIE as Figure 3.3 illustrates.

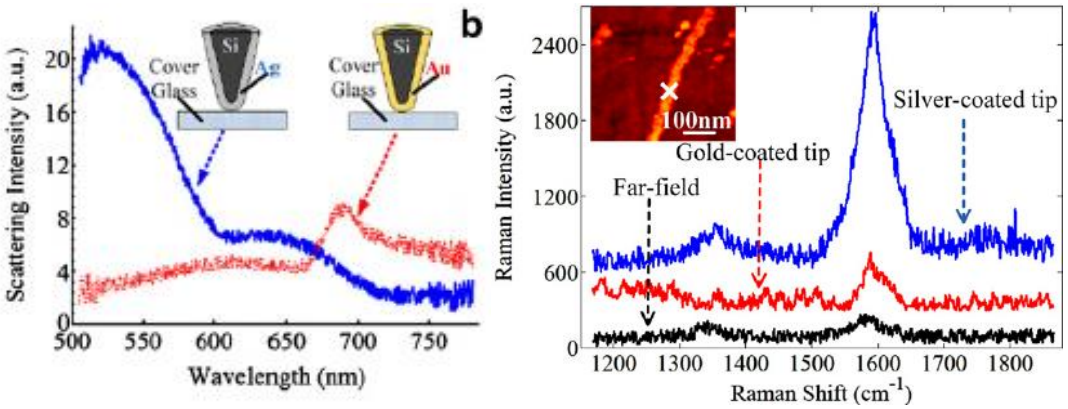

a) b)

Figure 3.3: Comparison of silver and gold tip designs by a) [98] and b) [99]

The work by Kumar [98] and Zhang [99] have demonstrated how the use of silver over gold can significantly increase the plasmonic intensity enhancement. However, we have previously discussed the issue of silver oxidation in Chapter 1 which makes gold a more commonly used plasmonic material since it is more resistant to oxidation than silver. The gold dipole in Figure 3.1 exhibits a clear plasmonic NFIE response that can be further improved. An earlier study [17], which has been discussed in Chapter 1, has demonstrated that varying the substrate thickness can improve the NFIE. The next step is therefore to optimize the dielectric substrate by truncating the size and height as well as adjusting the relative permittivity.

3.2 Dielectric cavity optimization

It has been reported in earlier studies that varying the permittivity would also affect the NFIE. As has been discussed previously, the plasmonic effect is rather sensitive to the parameters of the target material. This is the basis on which plasmonic super-resolution microscopy has high sensitivity and accuracy. A number of publications have studied the effects of the dielectric substrate but have focused on the dielectric constant impact rather than dimensions. [35], [100]. For example, in [100] it has been reported that the presence of the dielectric substrate can strongly influence the plasmon modes of a plasmonic nanoparticle and splits the plasmon modes to be parallel and perpendicular to the surface, which corresponds to the transverse and longitudinal plasmon modes that were previously discussed. Scholars have expanded on this work and investigated the NFIE of a silver nano-sphere above a dielectric substrate with varying nanoparticle sizes and substrate properties [35]. The results in [100] have been reinforced and it has been shown that the NFIE generally increases when the refractive index of the substrate increases and when the gap between the nanoparticle and substrate decreases. The nanoparticle size has a maximum impact on the NFIE which was shown to be dependent on frequency. In the same paper,

the NFIE strength of dielectric and metallic substrates have been compared and it has been reported that comparable NFIE was obtained for a silver nanoparticle with a radius of 25 nm above a silicon substrate and a gold substrate. However, the NFIE of a silver nanoparticle with a radius of 50 nm above a silicon substrate was stronger than the NFIE of a silver nanoparticle with a radius of 25 nm above a gold substrate. This demonstrates that there is a resonance, or mirroring, which occurs with dielectric substrates that can be equal to, or stronger than, the NFIE exhibited by gold substrates under certain conditions. However, both works of [35] and [100] have only optimized the dielectric substrate by optimizing the refractive index, n, without considering the impact of varying the substrate dimensions. On the other hand, in reference [17] it has been reported that the light intensity can be increased from 600 to 1000 V^2/m^2 by varying the substrate thickness for a particular nanoantenna from 50 to 200 nm. However, further investigations were left to future works and the full extent of the NFIE has not been investigated.

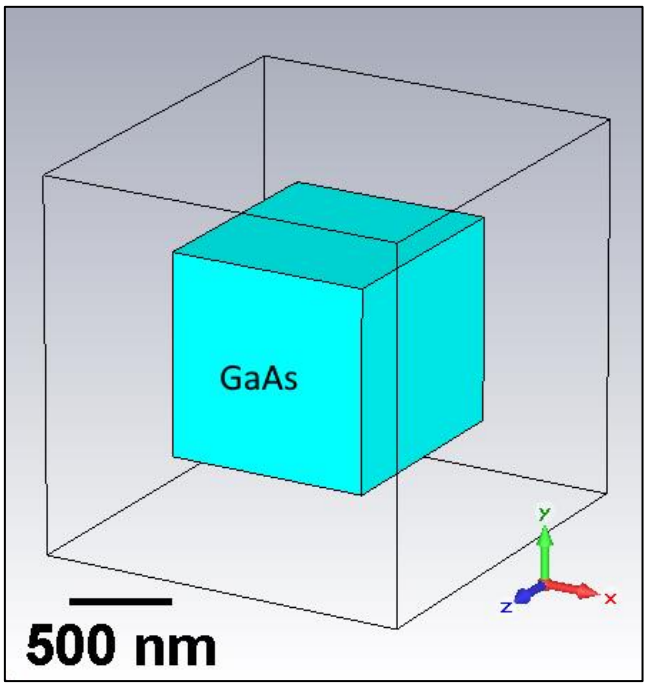

Figure 3.4: Simulated model of a dielectric cavity

Therefore, the substrate width and length have been truncated and the effect of the surface area on the NFIE has been investigated in this work. Figure 3.4 presents a simulated GaAs dielectric nano-cavity that has been designed initially as a cube with sides of 1000nm length. The dimensions have been optimized and the NFIE response has been recorded. To simplify the results, the design of the dielectric cavity had been limited to having a square surface by varying the width and length equally, and the structure exhibited a resonant frequency at 146 THz for a surface area of 880 × 880 nm with a thickness of 1000 nm when optimized as in Figure 3.5 and 3.6.

Although this is not a plasmonic NFIE in nature, it still describes a resonance effect for a near-infrared plane wave on a dielectric nano-resonator. If the nano-resonator can be coupled effectively with a plasmonic nanoantenna, the total NFIE can be increased substantially since the plasmonic antenna will be placed in the vicinity of a stronger localised field. It should be noted that in the absence of the nano-cavity, this sort of field intensity can be only achieved by increasing the strength of the incident plane wave to ~7 V/m, which is impractical. These design parameters have been employed and the dielectric cavity width and length were set to 880nm.

The impact of the dielectric cavity thickness has been studied as illustrated in Figure 3.6 for a square surface area of 880 × 880 nm. It can be observed from these results that a few resonance peaks exist with a maximum NFIE at a thickness of 1000nm.

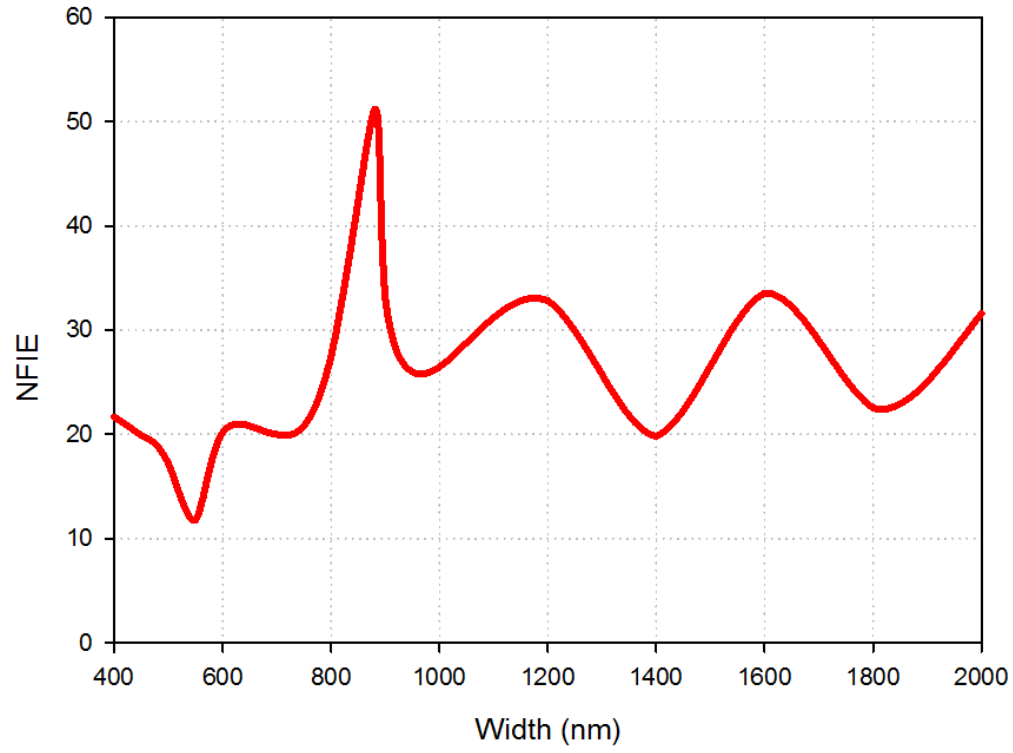

Figure 3.5: NFIE for a dielectric cavity with a square surface and various width as well as a thickness of 1000 nm

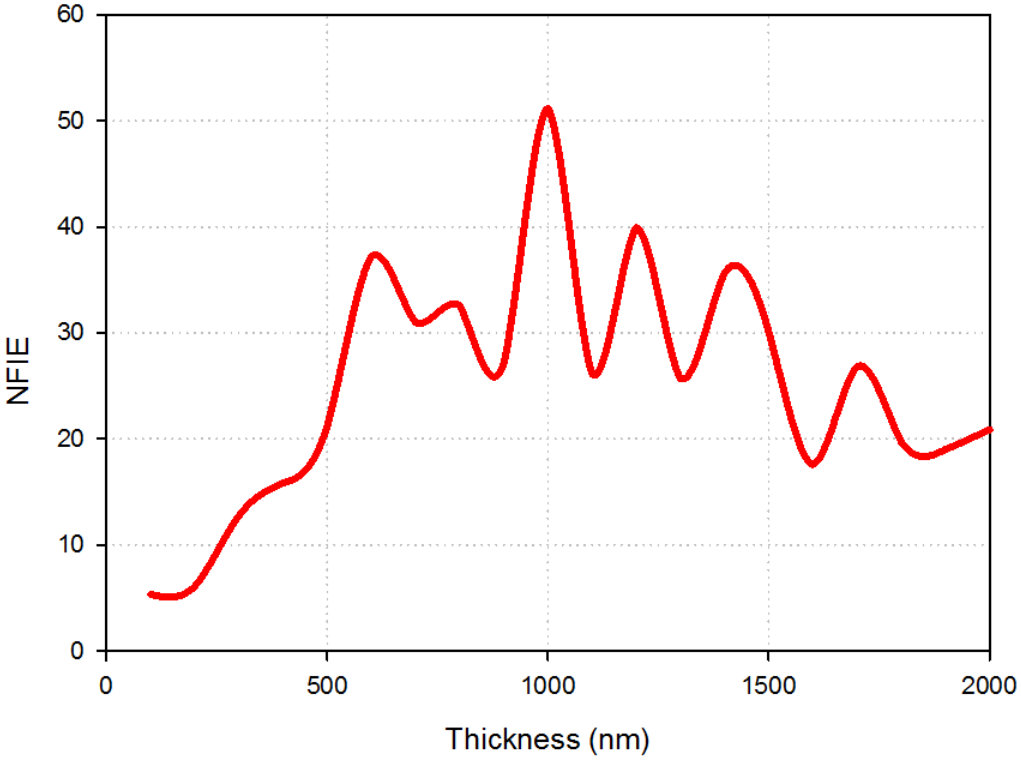

Figure 3.6: NFIE for a dielectric cavity with various thicknesses and a square surface size of 880nm x 880nm.

It should be noted that only two publications have been found that discuss the effects of substrate thickness at optical frequencies. One paper reported that changing the substrate thickness influences the results but did not pursue the research further, leaving it open for future work [17]. Another study has noted that the effective refractive index of the substrate changes according to thickness but does not delve deeper into the concept nor does it discuss the reasons [101]. The concept of effective length has been discussed in [102], where it has been reported that the refractive index as well as length of a refractive material will affect the propagation of an electromagnetic wave, where the time taken for the wave to propagate through a substance is:

$$t = \frac{nL}{c} \tag{3.1}$$

The behaviour of the dielectric cavity is of interest as the exact behaviour and relation of a dielectric cavity with a nanoantenna has so far not been discussed in detail in the literature, where most publications use a substrate instead. This gap in the current literature is the original inspiration for this work. However, the concept of effective length [102] means that the permittivity can also be adjusted, which would have the same effect as scaling the physical dimensions of the nano-resonator in all directions.

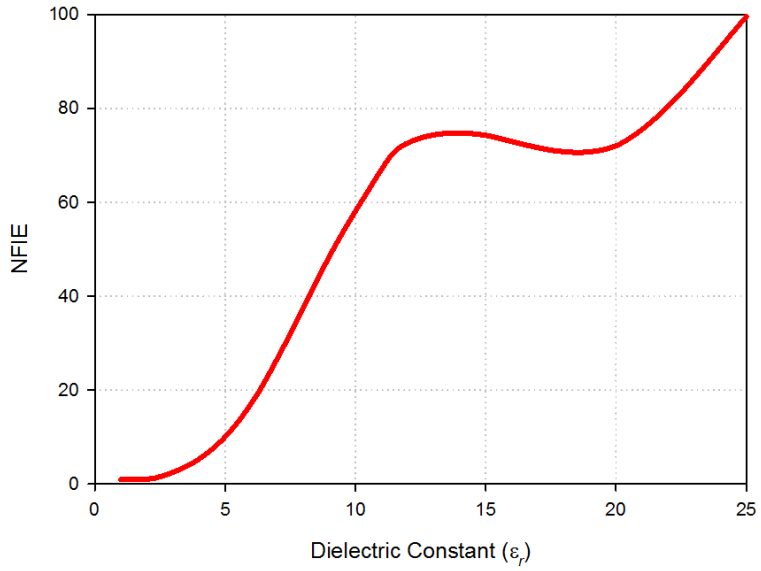

Figure 3.7: NFIE for the dielectric cavity with varying dielectric constants

Chapter 2 put forth the issue of low permittivity materials in the optical range. The simulations carried out were therefore focused in the relative permittivity range of ε_r =1 to 25. Figure 3.7 demonstrates that there is a local resonance peak at $\varepsilon_r \approx 12$ which would be useful due to the energy loss effects prevalent at higher permittivities as discussed in Chapter 2. Of the commonly used dielectrics for optical fabrication, gallium arsenide seems to have the closest properties to that peak. GaAs is known to have a static dielectric constant of 12.94 at lower frequencies. However, at optical frequencies, this behaviour changes and the dielectric constant at ~150THz is ~11 [82]. Although this value is not exactly the local maximum shown in Figure 3.7, it is high enough that it should create the intensity enhancement that is being pursued. Higher permittivities have been shown in Chapter 2 to have higher energy loss due to interband transition effects, which cause energy loss in the form of heating as well as reduced quality factors [89]–[91].

In the first part of this chapter, the plasmonic response of a gold dipole was verified in comparison to a PEC dipole. In the second part, a dielectric cavity is designed, and the dimensions optimized to improve NFIE. This goal must be carried out with relation to the

previous dipole nanoantenna since the aim is to couple them. First, the permittivity was varied, and values were obtained around $\mathcal{E}_r$ = 10 to 15 which would give strong results without the use of high dielectric constants. The problem with high dielectric constants was explained in chapter 2 where it was shown that at optical frequencies, very high permittivity materials above $\mathcal{E}_r$= 15 are very hard to obtain. The surface area and thickness of our rectangular dielectric cavity were then optimized which yielded a design of 880×880×1000nm with $\mathcal{E}r$ =~11. For higher accuracy, a material model for GaAs was used which uses experimental data fitted to the Adachi model (Appendix C).

The presented results confirm that a dielectric cavity demonstrates strong resonance characteristics where a maximum NFIE can be obtained by optimizing certain parameters. This is reminiscent of the behaviour of certain antennas in the microwave region and an attempt to explain this property is made. Multiple peaks have been noted when varying the surface area and the thickness and it hints at the presence of multiple modes. A dielectric cavity resonating with multiple modes is also found in the microwave frequency region. The most obvious theory when dealing with such resonant characteristics is the concept of Standing Wave Ratio (SWR based on the transmission line theory, and Dielectric Resonator Antennas (DRAs).

SWR denotes a superposition resonance which occurs when an incident plane wave is trapped in the cavity and is reflected internally against the outer surfaces. This can be visualized as the wave reflecting between the dielectric material walls and causing superposition, thus creating standing waves. When this phenomenon occurs in dielectric cavities at the microwave region, it creates resonant modes that can radiate, and the structure is called a Dielectric Resonator Antenna (DRA). A DRA is usually fed by an aperture, microstrip, or probe and radiates a far-field effect. From the above effects, it has

been found that the dielectric substrate seems to have strong characteristics at certain resonant frequencies which resemble the behaviour of a DRA, which supports our hypothesis, even though it behaves as a receiver instead of a transmitter. However, to validate this theory, the results obtained in CST simulation should be compared against the calculated results for a DRA. The equations for a DRA are readily known, and this allows us to compare both results. The dielectric cavity used is based on the DRA equations.

3.3 Modes of a Dielectric cavity

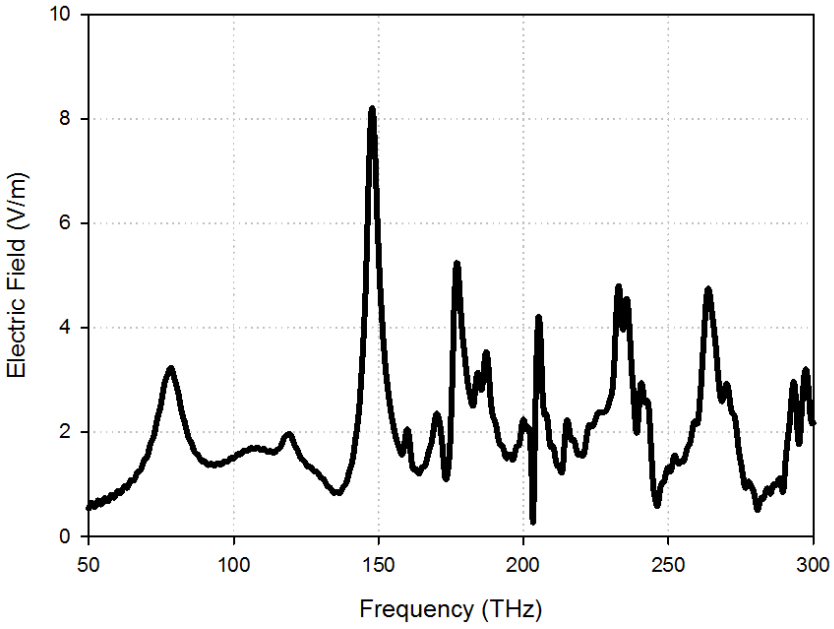

Figure 3.8: Resonance peaks of the proposed dielectric cavity corresponding to resonance modes

A dielectric cavity of dimensions 880nm×880nm×1000nm was analysed using the aforementioned DRA equations and the resonance modes were calculated. The dielectric cavity was then investigated in CST Microwave Studio to verify if the same resonance modes would occur. Figure 3.8 illustrates the resonance peaks of the proposed dielectric cavity, which at first glance, seems to correspond with some of the calculated resonance modes. However, to ensure no errors were made, each peak was investigated to confirm the resonance mode.

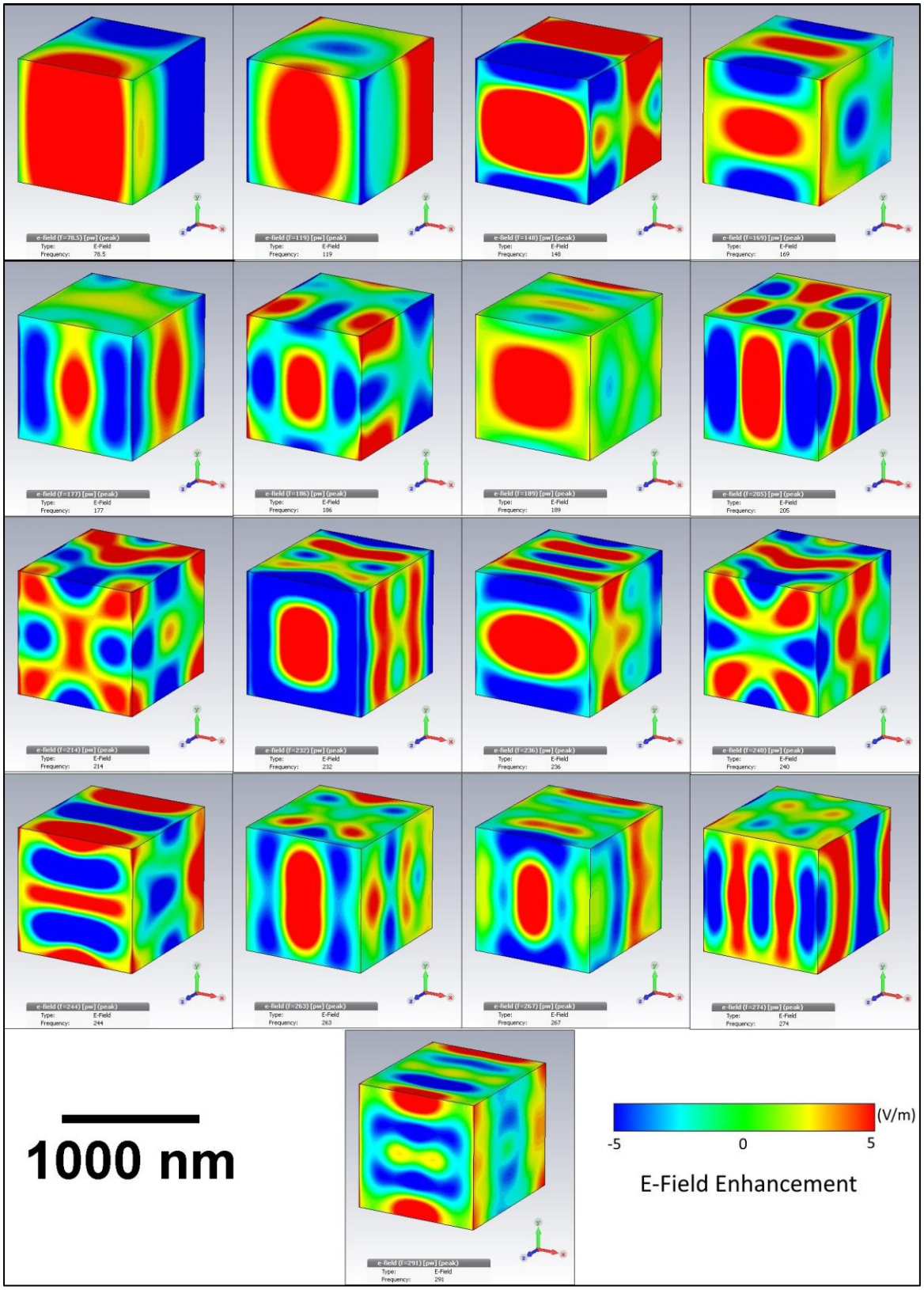

Figure 3.9: Field distribution at the resonance modes for the proposed dielectric cavity over a frequency range of 78.5 to 291THz. All cubes consist of GaAs with dimensions of 880 x 880 x 1000 nm.

Table 3.1: List of resonance modes for the proposed dielectric cavity based on numerical analysis and simulations

TE			Numerical Analysis Frequency (THz)	Simulation Frequency (THz)	Error (%)	Simulation Field Strength (V/m)
m	**n**	**p**				
1	**1**	**1**	86	78.5	8.7	3.2
1	**1**	**2**	116.6	119	2.1	2
2	**1**	**1**	124.1	-	-	-
1	**2**	**2**	147	148	0.7	8.2
2	**2**	**1**	153	-	-	-
1	**1**	**3**	154.7	-	-	-
1	**3**	**1**	169.5	-	-	-
2	**2**	**2**	172.1	-	-	-
1	**2**	**3**	178.7	169	5.4	2.3
3	**1**	**2**	186.9	177	5.3	5.2
2	**3**	**1**	191.7	-	-	-
1	**1**	**4**	195.9	189	3.5	3.5
2	**2**	**3**	199.8	-	-	-
3	**2**	**2**	207.2	186	10.2	3.1
3	**1**	**3**	212.8	205	3.7	4.2
1	**2**	**4**	215.4	-	-	-
4	**1**	**1**	217.8	-	-	-
3	**3**	**1**	223.8	-	-	-
2	**3**	**3**	230.8	-	-	-
1	**4**	**2**	231.6	-	-	-
2	**2**	**4**	233.2	-	-	-
2	**4**	**1**	235.4	-	-	-
3	**3**	**2**	237.3	-	-	-
1	**1**	**5**	238.7	-	-	-
1	**3**	**4**	244.4	236	3.4	4.5
2	**4**	**2**	248.2	-	-	-
1	**4**	**3**	252.9	244	3.5	2.5
1	**2**	**5**	254.9	-	-	-
3	**3**	**3**	258.1	-	-	-
2	**3**	**4**	260.3	-	-	-
3	**4**	**1**	262.2	-	-	-
5	**1**	**1**	267.3	-	-	-
4	**2**	**3**	268.2	-	-	-
2	**2**	**5**	270.2	-	-	-
3	**4**	**2**	273.8	-	-	-
5	**1**	**2**	278.6	-	-	-

3	**1**	**5**	279.9	-	-	-
4	**1**	**4**	280	274	2.1	1.1
5	**2**	**1**	281.8	-	-	-
3	**3**	**4**	284.7	-	-	-
4	**3**	**3**	292.1	-	-	-
5	**2**	**2**	292.6	-	-	-
3	**2**	**5**	293.8	-	-	-
4	**2**	**4**	294	-	-	-
4	**4**	**1**	295.7	-	-	-
5	**1**	**3**	296.6	-	-	-

Figure 3.9 illustrates the resonance modes which were found at each visible peak obtained in CST. Each resonance mode is clearly seen and can be linked to the corresponding calculated mode and listed in Table 3.1. However, some diagrams did not have clear modes and were left ignored. A glance at Table 3.1 shows that although many modes are calculated, not all the modes have a strong resonance peak, and are thus not distinguishable. The error difference between the simulated and calculated modes is shown and the error difference is usually ~3% with a single abnormality with a 10% frequency shift error. The electric field strength of the clear modes is also recorded, with the strongest enhancement occurring for the TE_{122} resonance peak at 148THz with a recorded electric field of 8.2V/m for an incident plane wave with electric field strength of 1V/m. This Dielectric Resonant Cavity (DRC) has been utilized in this dissertation to increase NFIE in various ways.

3.4 Optimizing a Dipole Nano-antenna

The main reason for choosing a strip dipole as our plasmonic antenna is the simplicity of such a structure. Ideally, the NFIE improvement is not limited for a particular antenna type and can demonstrate the validity of an approach using a basic antenna configuration initially, and then confirm the generality by studying more complex

geometries. To that end, the dipole does not really need much optimization. Therefore, a strip dipole has been placed at the centre of a dielectric cavity with dimensions of 880 × 880 × 1000nm made using gallium arsenide with an ε_r=11 at ~200 THz.

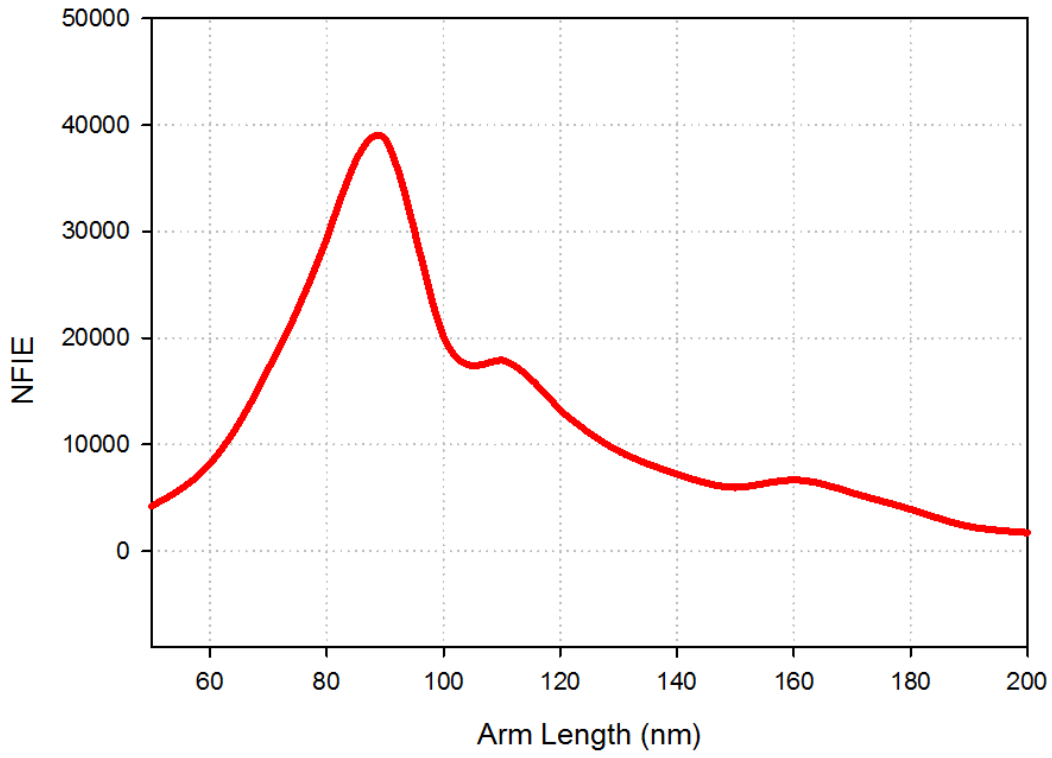

Figure 3.10: Effect of varying dipole arm length on the NFIE at 146THz for a dipole coupled to the TE_{122} DR mode

The dipole arm length has been varied as illustrated in Figure 3.10, where it can be noted that a strong resonance has been achieved with an arm length of 90nm, giving a total dipole length of 180nm, which corresponds to ~0.09λ_o. This would be surprising in the microwave region as the dipole is expected to have a resonant length of half the wavelength, i.e. 1000nm at this operating frequency. However, at optical frequencies, the plasmonic metals have complex permittivity and is effectively "shortened" as discussed by [103]. The effective wavelength scaling of the optical antenna creates a resonance at 146 THz for a dipole length of only 180nm.

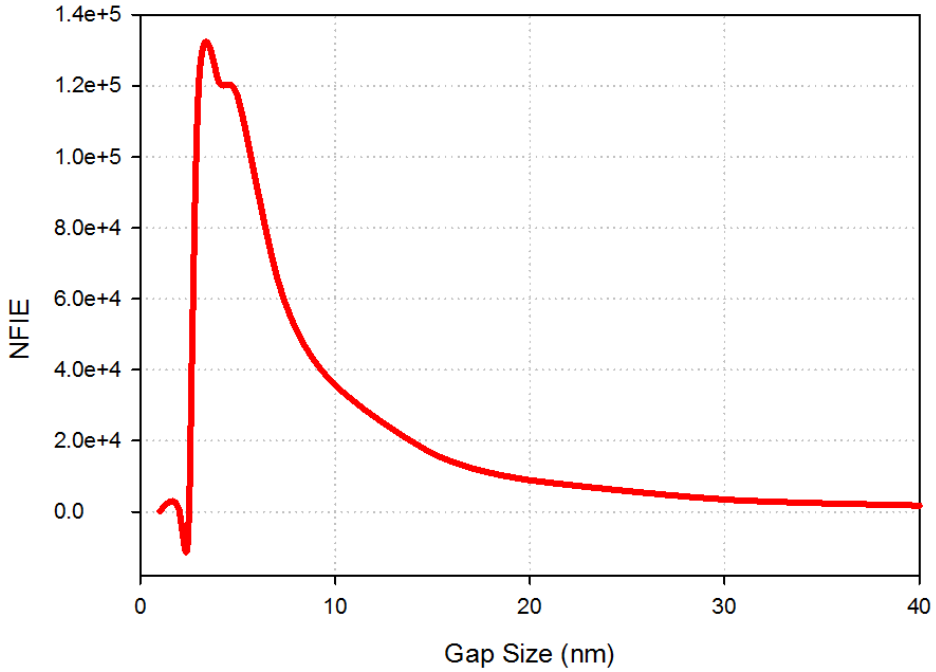

Figure 3.11: Effects of varying the dipole gap size on NFIE at 146THz.

Figure 3.11 demonstrates the dependence of SPR on the gap between the dipole arms. It is well-known that reducing the gap size of two plasmonic structures will drastically increase the NFIE in the gap due to the polarization of the dipole ends at the presence of an incident plane wave. This creates strong positive and negative ends which can couple, and the coupling increases exponentially as the ends come closer. This is reflected in the increased NFIE from 1600 to 130k as the gap size reduces from 40 down to 2nm. However, as the gap size becomes smaller than 2nm, the two separate arms start to behave as one large strip and the NFIE in the gap drastically drops. The gap size used consistently in this dissertation is 10nm, which serves multiple purposes. First, a 10nm gap yields a strong NFIE, while the dipole arms are still far enough apart that they don't act as a single dipole arm. Additionally, a 10 nm gap is often found in the literature for other coupled plasmonic antennas and would allow for a direct comparison of resultant NFIE. Furthermore, 10nm is a fabrication resolution that can be achieved by many fabrication methods and should be much more cost-effective than designs with 5nm gaps or less.

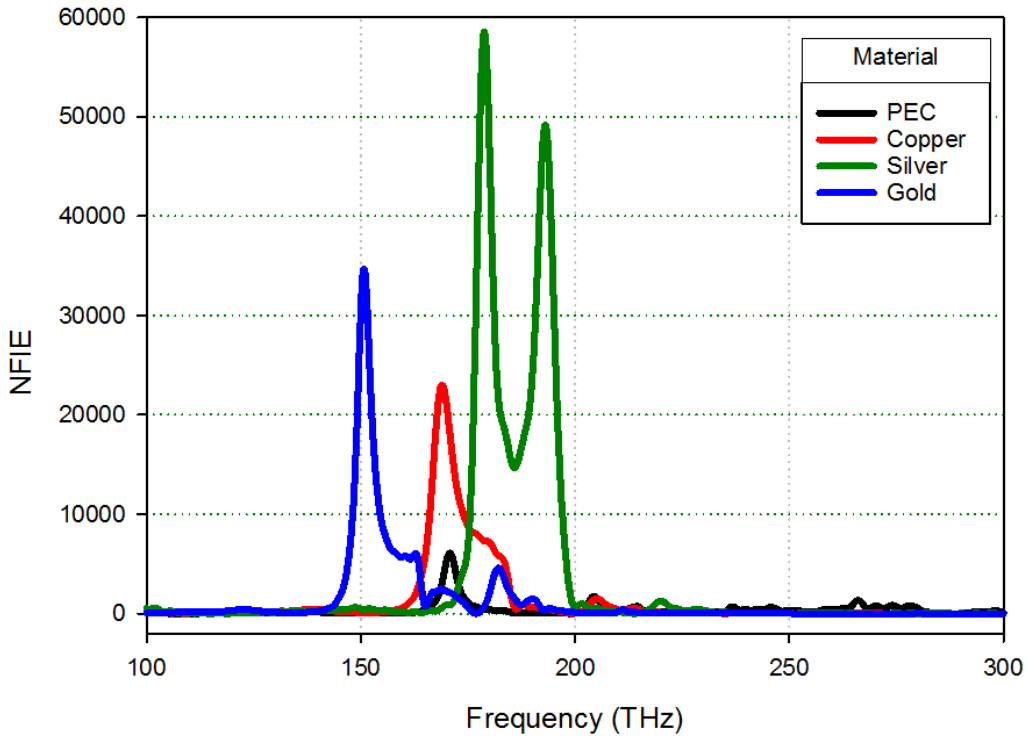

Figure 3.12: Effect of changing metals on NFIE

The effect of various metal types on a dipole has been explored earlier, but the interaction of the dipole with the dielectric cavity should be fully explored. The dipole material has been replaced with two other noble metals as well as a Perfect Electric Conductor (PEC). Figure 3.12 illustrates how PEC still does not have a plasmonic response, which keeps its NFIE at ~5k. Copper and silver have strong plasmonic responses, but they shift the resonant frequency and the dielectric cavity dimensions had to be scaled to couple with the dipoles resonant frequency when the arm length is maintained. The copper dipole offers a NFIE of 22k with silver having the strongest NFIE of nearly 60k. Although the NFIE for the gold dipole of 37k is not as strong as silver, this has already been discussed and the choice of gold due has been justified due to the oxidation effects of silver.

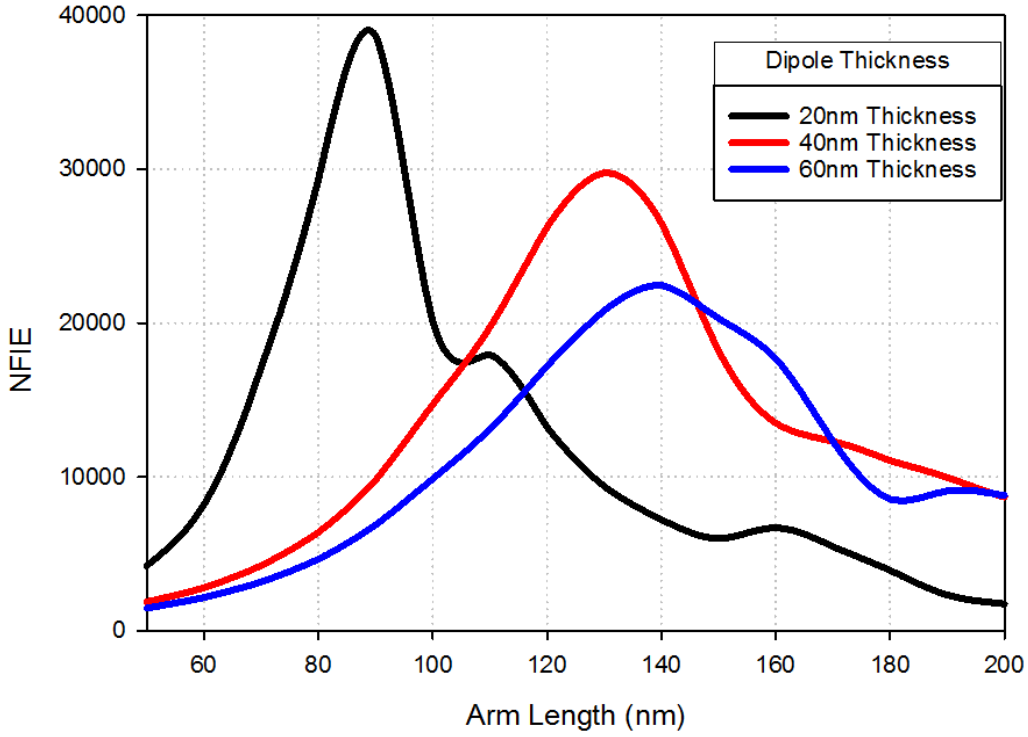

Figure 3.13: Effect of varying dipole thickness on NFIE at 146THz

The surface effects of SPR go down to a depth of 20nm [104]. It should be noted that there is an ideal thickness for each application of plasmonic metals. Particles that are too large, or too thick, allow for the excitation of non-radiative multipoles. Designs that are too small or too thin however, cannot enhance the field as well [105]. As the size approaches a few atoms, the definition of plasmon, which requires a large collection of electrons to oscillate together, does not hold. Figure 3.13 illustrates how at different dipole thicknesses, different dipole arm lengths are required to reach resonance. This is because the plasmonic resonance does not just depend on the length of the dipole, but rather has a non-linear relation with the aspect ratio, based on both length and thickness. A dipole thickness of 20nm is found to have a strong NFIE at an arm length of 90nm, which is used in this dissertation.

After optimizing both the dipole and the dielectric cavity, an NFIE of 37k has been accomplished, which is significantly higher than most other papers that have a typical NFIE of less than 5k. In the final design, a gold strip dipole with arm lengths of 90nm and thickness of 20nm, is coupled to the TE_{122} mode of a GaAs dielectric cavity of 880nm × 880nm × 1000nm, with a plane wave excitation source going down in the –Z axis facing the surface with the dipole in an orthogonal direction. Only three papers have reported NFIE that exceeds 5k. The first paper [51] achieves this by calculating theoretical results using gap sizes of less than 2nm, whereas this study utilizes a more practical gap size of 10nm. The second paper [43] uses a Fabry-Perot effect that is similar to lasers, where the incident light is focused strongly using dielectric mirrors, and this approach is explored further in Chapter 4. Finally, the third paper [38] has an NFIE of 29k, which is weaker than the result of this study, but is still significantly higher than other results in the literature. It should be noted that the reported enhancement in the third paper has been achieved by utilizing a gold substrate, which effectively creates an extremely large antenna surface, allowing the plasmonic antenna to catch a large amount of the incident light. Therefore, the result of this dissertation can be considered a significant achievement in terms of the NFIE obtained.

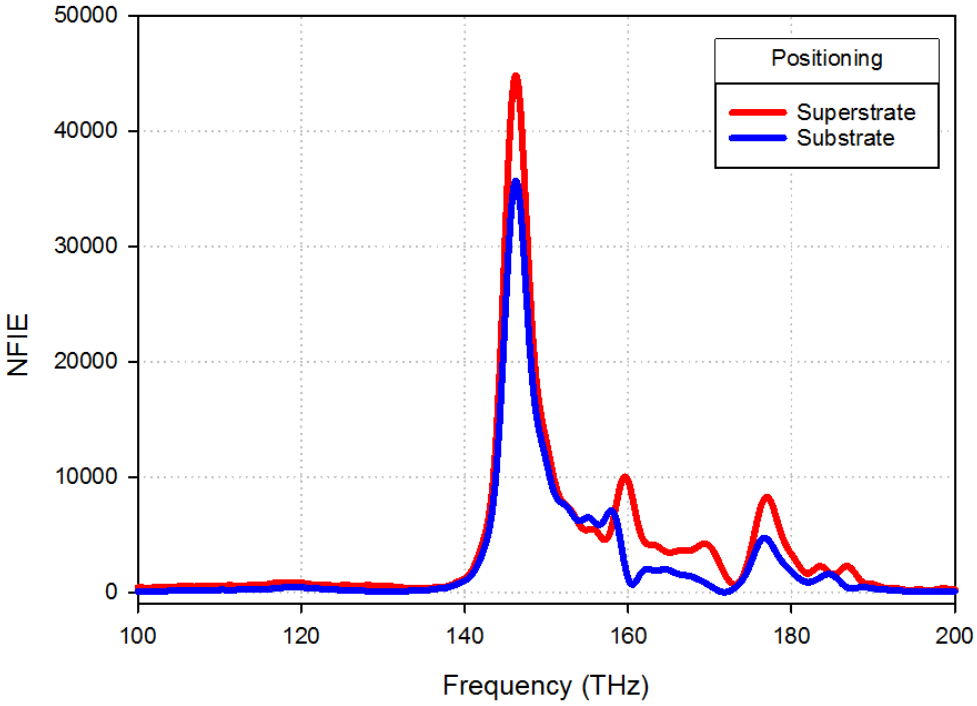

Figure 3.14: NFIE of a Dipole on the Dielectric Cavity

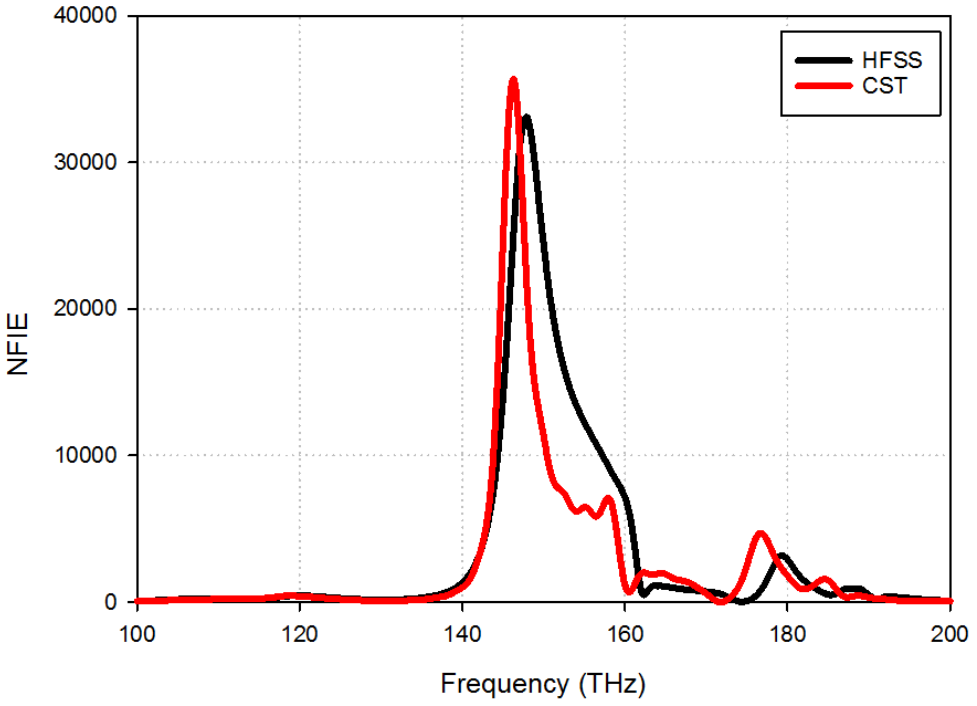

Figure 3.15: NFIE for a 180nm long gold dipole on a 880x880x1000nm dielectric cavity

It is important to note that the proposed cavity substrate supports the TE_{122} resonance mode with strong surface electric fields on both sides. Therefore, it can also be used as a superstrate when placed between an incident optical wave and the plasmonic dipole, where so far the dipole has been placed in between the plane wave and the dielectric resonator. This superstrate has also been termed as a superlens [106]. Using the same design as a superstrate provides a considerable increase in the NFIE from 37k to 45k as illustrated in Figure 3.14. The accuracy of the achieved results are supported by reproducing them using a different solver, namely ANSYS HFSS. With the same parameters and material models, CST had a resonance at 146THz with an electric field of E = 189 V/m that corresponds to a NFIE of 37k. On the other hand, HFSS results demonstrate a resonance at 147.5THz with an electric field of E = 183 V/m that corresponds to a NFIE of 33.5k. Comparing the two set of results in Figure 3.15 shows minor discrepancies of ~1% and 3% in the resonance frequencies and electric field, respectively. There is a possibility that a denser mesh could converge the results further, but differences are expected due to the different solving methods, where CST utilizes FIT while HFSS utilizes FEM as described in Chapter 2.

3.5 Bowtie nano-antenna

The proposed hybrid antenna configuration demonstrates a remarkable NFIE even when the dielectric cavity is paired with a basic dipole antenna. According to the literature, other antenna shapes can yield significantly higher NFIE results, particularly in the case of a bowtie design. Therefore, a gold nano-bowtie has been designed to resonate at ~150THz and positioned on top of the dielectric cavity. Figure 3.16 shows a bowtie designed with certain dimensions that are close to the size of the previously studied dipole. The bowtie has been designed with two equal sides of 107nm length in conjunction with an angle of ~30˚ that has been tuned to 31.6˚ to resonate at 146 THz. A tip radius of 5nm has been

used to simulate the imperfect tip of a real bowtie that cannot be infinitely sharp. This is important to temper the lightning effect that would be generated with a perfect tip, which would skew the results. The gap size of 10nm and gold thickness of 20nm have not been changed to maintain consistency in the results.

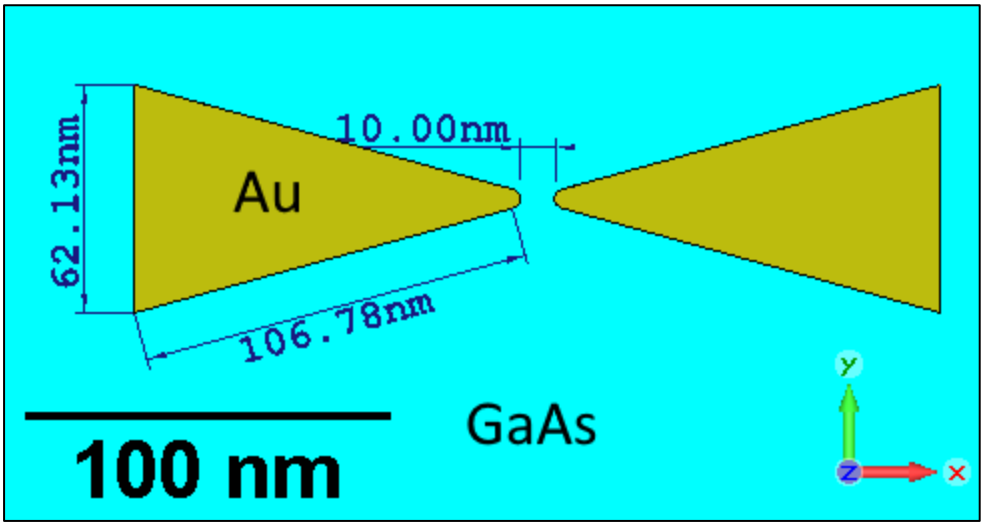

Figure 3.16: A gold bowtie on a GaAs dielectric cavity

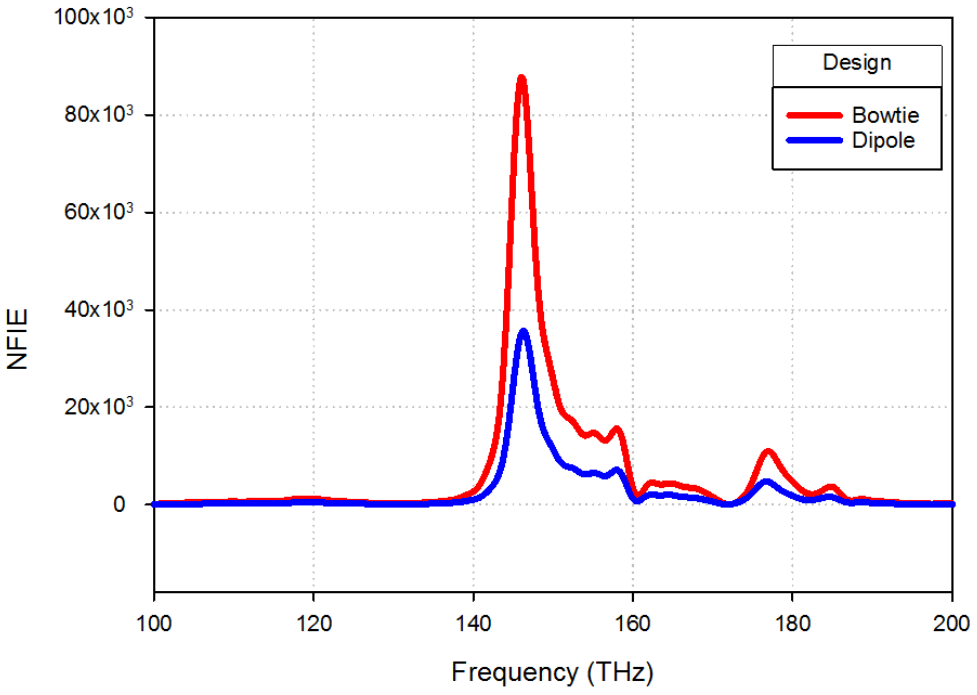

Figure 3.17: Effect of the plasmonic antenna shape on the NFIE

The NFIE has been simulated by placing a probe in the bowtie gap as demonstrated in Figure 3.16, whereas Figure 3.17 illustrates that the hybrid bowtie-DRA antenna yields a strong NFIE result of ~88k as compared to ~37k for the dipole when the dielectric cavity is used as a substrate. This is due to a significant 1.55 times increase in the electric field, which leads to a NFIE that is 2.4 times stronger due to the quadratic relation of electric field strength and NFIE. In order to further understand the relation between the two dipole and bowtie antenna designs, both antennas have been simulated once again by replacing the DRC with a 50nm thick GaAs substrate with a width and length of 3000nm × 3000nm.

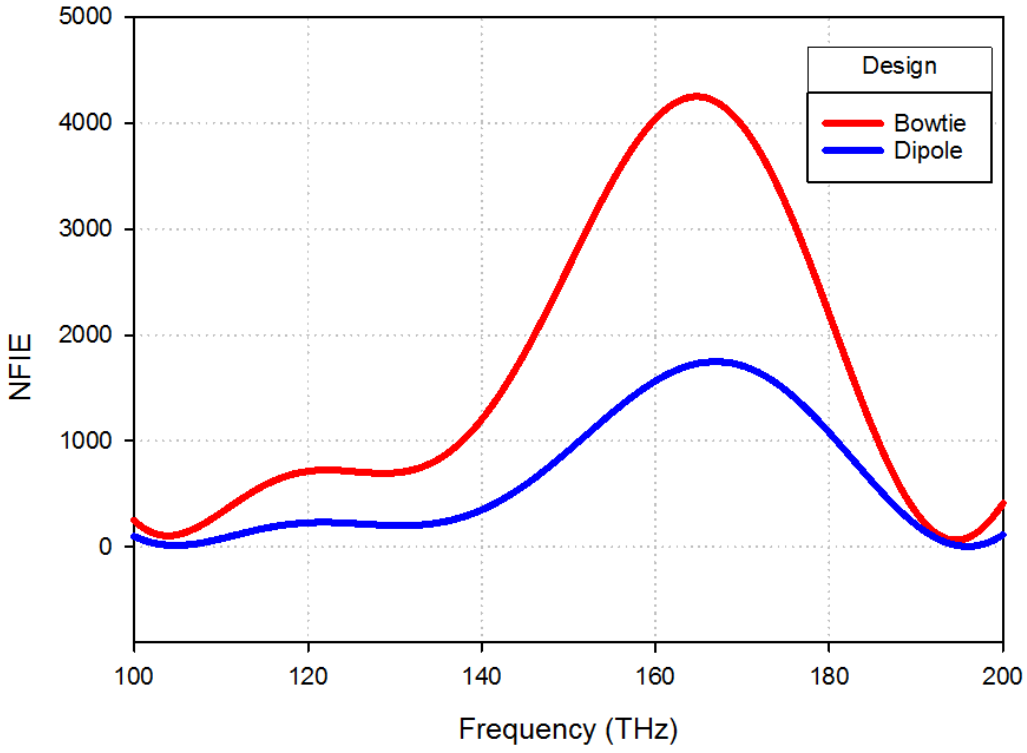

Figure 3.18: NFIE response of plasmonic antenna designs on a 50nm thick GaAs substrate

Previously, a linear relation has been noted between the NFIE of the cavity and the NFIE of the hybrid structure Figure 3.18 shows that changing from a dipole to a bowtie improves the NFIE from 1750 to 4250, an increase by a factor of 2.4 times which is similar to that of Figure 3.17. Therefore, it is clear that the dielectric cavity is amplifying the

incident plane wave by a factor of ~4.6 through concentrating the electric field it onto hotspots, where the plasmonic antenna is positioned. These antennas, whether dipole, bowtie, or any other design, capture the optical energy and causes electron oscillations on the surface, thus causing plasmonic resonance. The relation between the strength of the squared incident plane wave and the strength of the NFIE is clearly found to be linear.

3.6 Conclusions

The parameters that govern the light enhancement of a plasmonic dipole have been studied by other scholars when the dipole is placed on a substrate with infinite dimensions. In this study, a dielectric cavity has been utilized as a substrate. Investigations demonstrated that strong resonant electric fields could be created on the surface of a dielectric cavity, which could be coupled to a plasmonic antenna. This effect has been studied and a design has been produced for a hybrid dielectric cavity and a plasmonic dipole that would resonate together in the ~150 THz frequency region. The combination of dipole and dielectric cavity provided a significant improvement of the NFIE from 1750 to 37k by utilizing a GaAs dielectric cavity instead of a GaAs substrate, which is a clear improvement of 21 times when coupled with the TE_{122} resonance mode of this cavity. Repeating the study for a bowtie on a substrate and on a dielectric cavity also showed a 21 times improvement from 4250 to 88k. This shows first of all, that the improvement due to the cavity can be combined with other NFIE improvement techniques. It also shows that the demonstrated improvement follows a clear relation and can be calculated in advance. The incorporation of a dielectric cavity increases the NFIE of other plasmonic antennas by a factor of 21 as well, as long as the same frequency and incident light conditions are met.

(This page is intentionally left blank)

Chapter 4: **Dielectric Mirrors and Lenses for Further Light Intensity Enhancement**

In the previous chapter, it has been demonstrated that the plasmonic effect is dependent upon focusing incident light into subwavelength locations and therefore can be enhanced in the vicinity of a strong light spot. The presence of a dielectric cavity has a considerable impact on focusing the incident light and delivering more light “per square inch” to the acting plasmonic antenna. Techniques that enlarge the surface area of the plasmonic antenna to capture a stronger incident light, such as lengthening the dipole and utilizing a bowtie, have also provided further increase in the NFIE but may shift the resonance frequencies further from a target operating frequency whereas the method discussed in Chapter 3 of a dielectric cavity can preserve it. Therefore, it is of interest to study other techniques of focusing incident light to the plasmonic structure without any changes to the plasmonic antenna itself. This chapter investigates dielectric mirrors and lenses as methods to concentrate the incident optical wave.

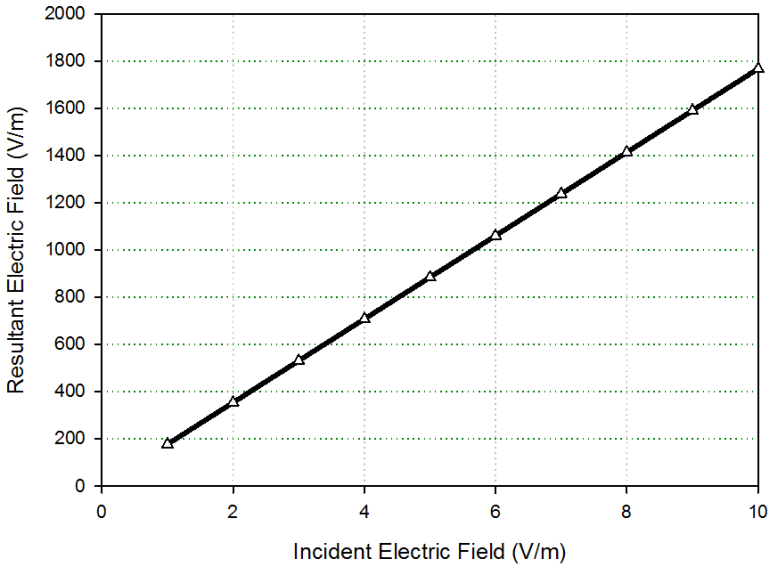

Figure 4.1: Electric field enhancement for increasing incident light

In Chapter 3, it has been demonstrated how the stronger coupling between dielectric cavity and plasmonic antenna has increased the electric field in the nanoantenna gap by a factor of ~4.6, which corresponds to improving the NFIE by ~21 times. The question then arises as to whether a direct increase of the incident light strength would also yield a linear increase in the focused electric field. Figure 4.1 illustrates the resultant electric field measured in the gap of a gold dipole with arm lengths of 90nm and thickness of 20nm on a GaAs dielectric cavity of 880x880x1000nm at ~150 THz, as the incident electric field as varied. A direct increase of the incident optical field strength from 1 to 2, or 3 V/m changes the electric field in the gap from 180 to 360, or 540 V/m. This is a linear increase and demonstrates that the dielectric cavity is clearly focusing the incident light when utilized as a substrate or superstrate and that other techniques to focus the incident light are therefore expected to also increase the NFIE of a nanoantenna. Various structures that are capable of focusing the incident light have been investigated in this chapter to identify other methods of increasing NFIE. This includes metallic and dielectric mirrors, lenses as well as Fabry-Perot cavities.

4.1 Metallic Mirrors

A straightforward approach of doubling the incident light is through the use of a ground plane or reflector that acts as a metallic mirror. At frequencies lower than the THz range, it is a standard practice to utilize metallic ground planes in numerous antenna configurations. However, high ohmic losses in the ground plane can be introduced at optical frequency ranges. On the other hand, mirrors based on reflective coatings exist but report a reflectivity of between 94 – 98% [57], which is considered lossy when compared to dielectric mirrors with a potential reflectivity above 99.9% [67]. The use of such a mirror can effectively double the incident light acting upon the nanoantenna. Ideal Perfect Electric Conductors (PEC) can simulate mirrors that reflect the incident plane wave without any loss and have double the electric field at a distance of a quarter wavelength above the PEC surface due to phase changes during reflection. The tangential electric field on the PEC surface itself should be zero due to out of phase cancellation effects. Furthermore, the presence of a mirror would also create an image of the hybrid dielectric cavity and nanoantenna configuration. In order to preserve the dielectric cavity size and its resonance mode frequencies, the dielectric cavity height must be halved when placed above a ground plane. This arrangement has been simulated in CST with an ideal metallic mirror by introducing an “electric boundary” condition at the xy plane as illustrated in Figure 4.2.

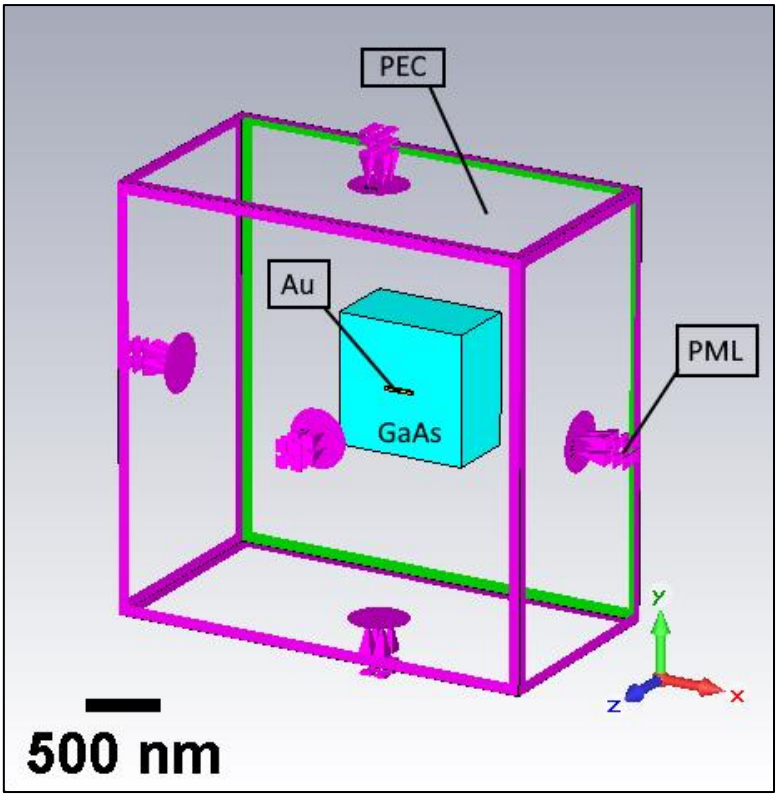

Figure 4.2: Original structure mirrored across the z-axis using an electric boundary in CST

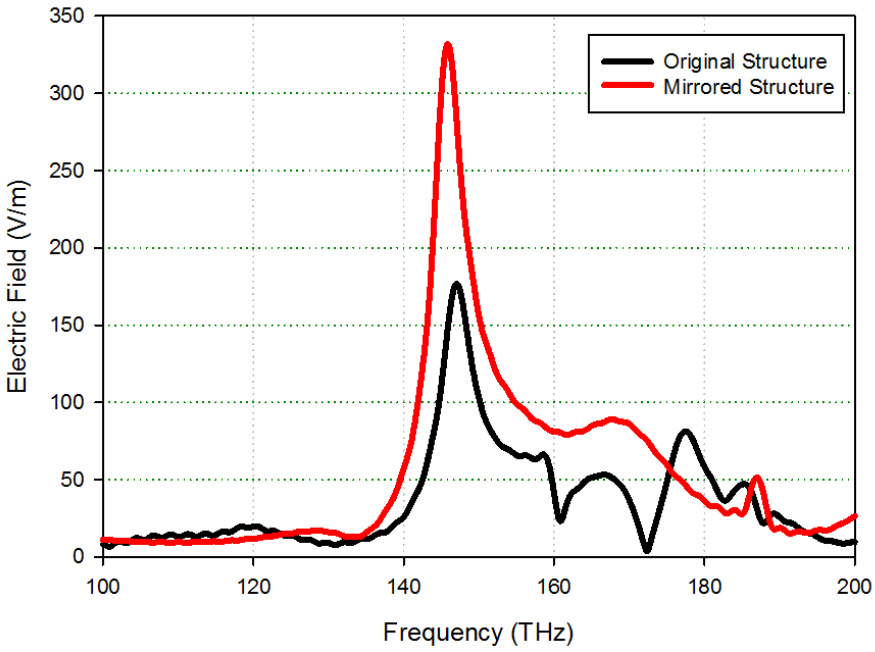

Figure 4.3: The electric field in the dipole gap for the original optimised structure and that of a reduced height structure on a ground plane

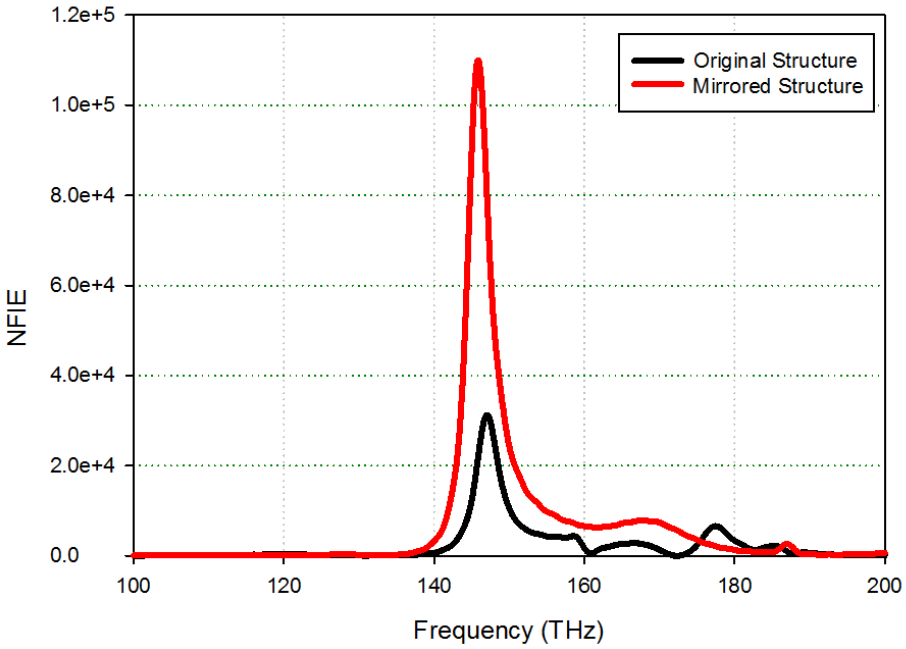

Figure 4.4: NFIE of the mirrored structure

The results in Figure 4.3 indicate that this design nearly doubles the electric field from 180 V/m to 330 V/m while reducing the total structure height by half to 500 nm due to the mirroring properties of the electric boundary while still maintaining the excited mode of TE_{122}. This is consistent with the earlier hypothesis where a doubling in the incident electric field is expected due to mirror effects therefore quadrupling the NFIE to 110k as can be observed in Figure 4.4. However, the thickness of the structure is 500nm whereas ¾ wavelength at 150 THz in lossy GaAs is roughly equivalent to 450nm. The doubling effect can occur both at the quarter wavelength and three-quarter wavelength mark, but the thickness discrepancy between 450 to 500 nm reduces some of the effects, thus causing the mirrored structure to have an electric field of 330 V/m. Some of the losses can also be attributed to losses due to using a lossy GaAs model. A thickness of three-quarter wavelength could be achieved, but this would then require scaling the dielectric cavity, thus shifting the resonant frequency and reducing the coupling with the gold dipole. Therefore, the small losses due to this discrepancy is acceptable at this point unless other designs are

utilized that allow both resonance with the gold dipole and with an ideal thickness to utilize the quarter wavelength effect. This is attempted later in this chapter when pursuing the concept of a low-profile dielectric cavity.

4.1.1 Mirrored structure on a Ground Plane

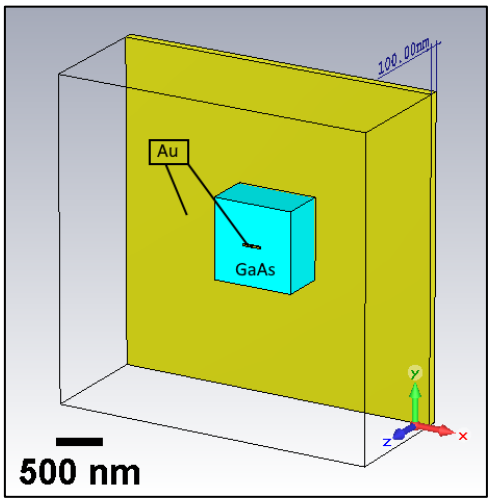

Figure 4.5: The half-structure mirrored using a gold ground plane

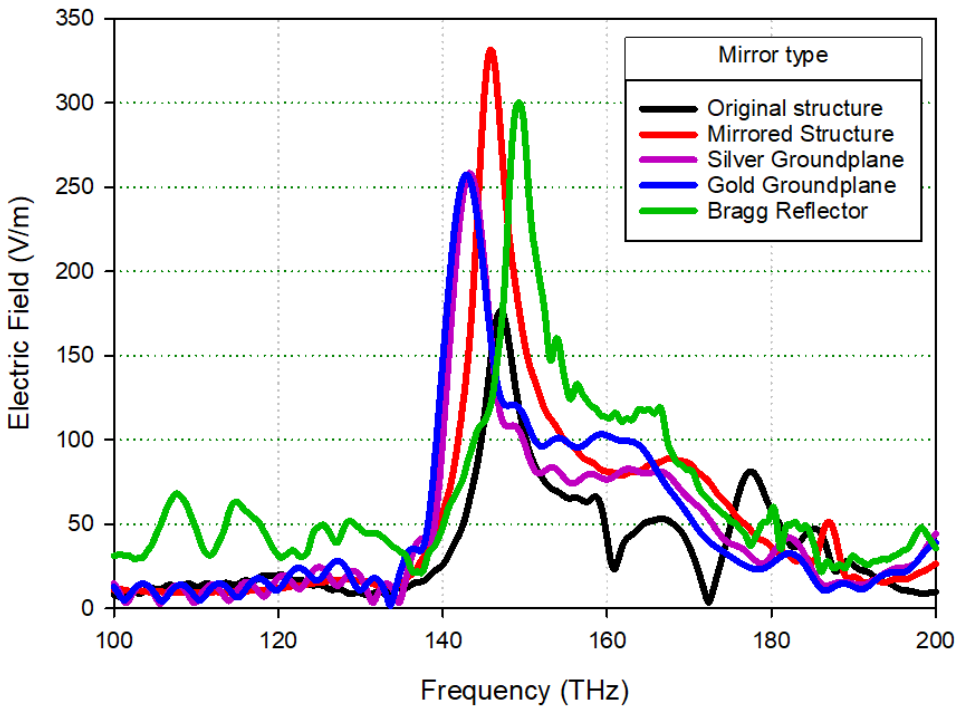

Figure 4.6: Comparison of the electric fields of various mirrored configurations.

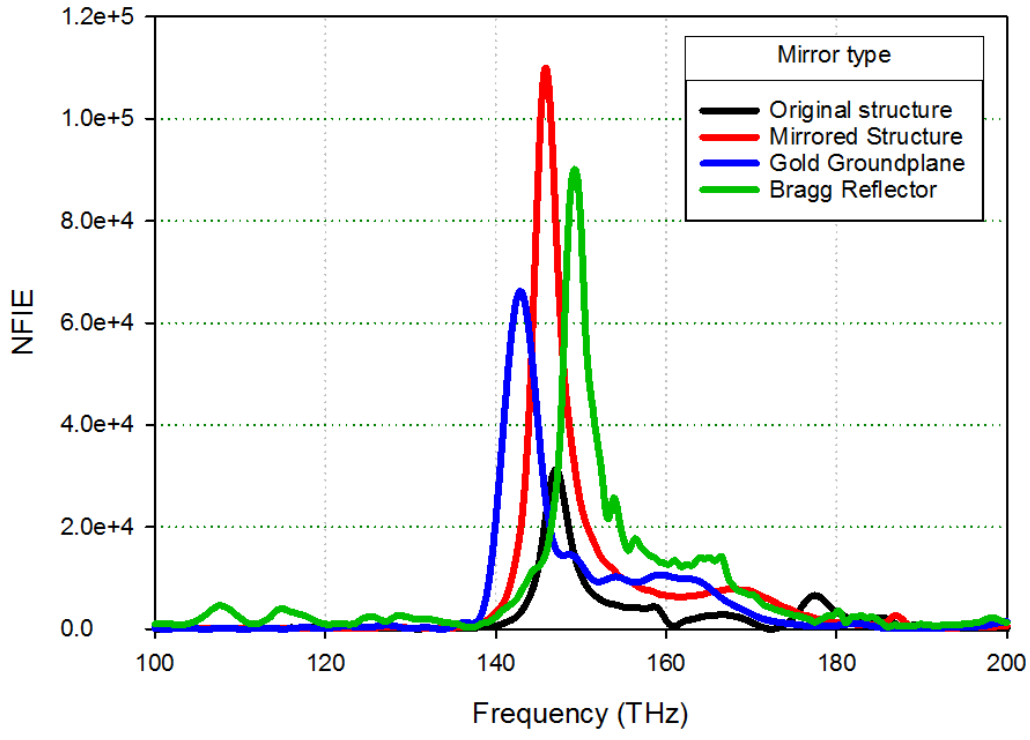

Figure 4.7: NFIE of the various mirrored configurations.

The electric boundary in the design, or PEC ground plane, was replaced with a gold ground plane of a thickness of 100 nm and utilizing the same gold model as the gold dipole. This yields a strong electric field in the dipole gap as demonstrated in Figure 4.6 of ~260 V/m, which is less than that presented earlier owing to the metallic nature of the mirror that is associated with extremely high losses in the frequency region of interest. It is interesting to note that the use of a silver ground plane gives nearly identical results, which is due to the distance of the ground plane from the dipole, whereby most of the surface plasmon resonance from the ground plane has disappeared and does not affect the electric field in the dipole gap. The resultant NFIE is displayed in Figure 4.7, although the NFIE for a silver ground plane is omitted since it is functionally equivalent to the gold ground plane. Although the metallic ground planes have high loss when compared to the ideal mirrored structure, the total electric field and subsequent NFIE when introducing the gold reflector is still higher than that of the original structure with the added benefit of a lower profile.

The gold ground plane can behave as a plasma in this frequency region and therefore requires a certain thickness to prevent electrons from merely piercing through to the other side which would exacerbate the losses even more.

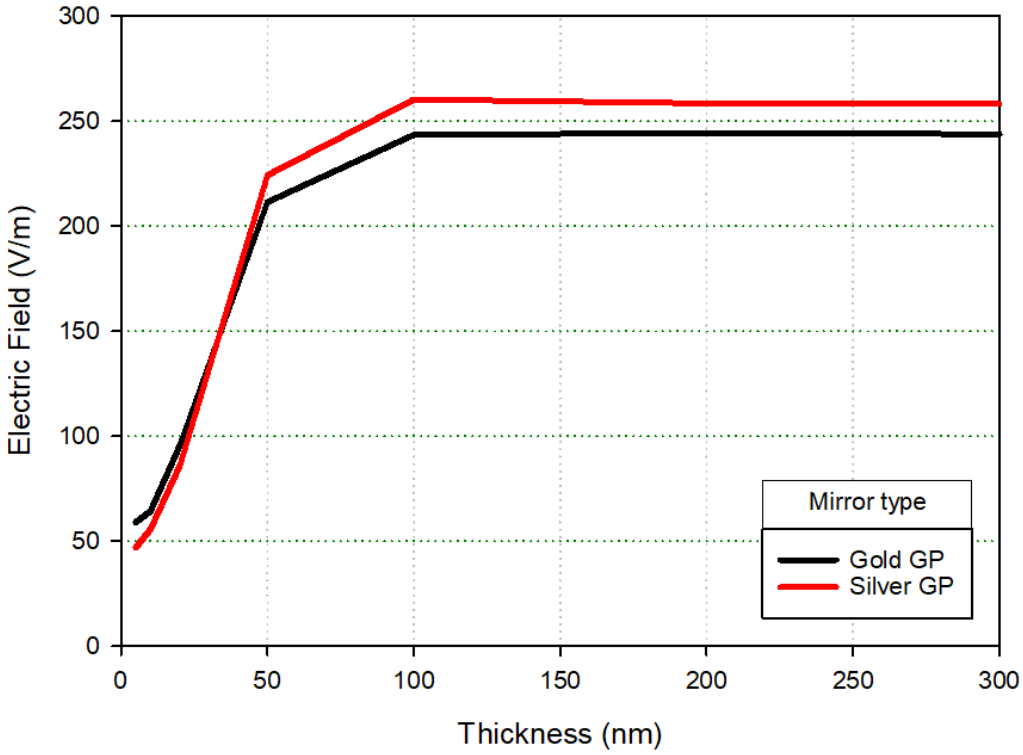

Figure 4.8: Effect of ground plane thickness on the resultant electric field

This is proven by conducting some simulations which show that at 5nm thickness, the gold ground plane is not very effective, and it approaches full effectivity as the thickness goes over 100nm as described in Figure 4.8. In comparison, the absorption coefficient, α, of gold is 7.4666x10^5/cm and for silver is 7.8642x10^5/cm. This was found using the extinction coefficient, *k*, values from our gold and silver models and calculating absorption coefficient, $\alpha = 4\pi k/\lambda$. This translates into corresponding absorption depths of ~13.4nm for gold and ~12.7nm for silver, at which depth the light would drop to 1/e (~36.8%) of its original intensity, giving a transmittance of T = 36.8%. To reduce the transmittance to T<0.1%, it is calculated that the absorption depth must be multiplied by roughly 8 times as

depicted in Table 4.1. At this calculated thickness, nearly all the incident light is either reflected by the ground plane or absorped due to plasmon resonance, both of which would increase the NFIE of the gold dipole.

Table 4.1: Calculated Transmittance of Gold and Silver ground planes using Absorption Coefficients

Gold Ground Plane		**Silver Ground Plane**	
Thickness (nm)	**Transmittance, T (%)**	**Thickness (nm)**	**Transmittance, T (%)**
13.4	36.80%	12.7	36.80%
13.4 x 2 = 26.8	13.54%	12.7 x 2 = 25.4	13.54%
13.4 x 3 = 40.2	4.98%	12.7 x 3 = 38.1	4.98%
13.4 x 4 = 53.6	1.83%	12.7 x 4 = 50.8	1.83%
13.4 x 5 = 67.0	0.67%	12.7 x 5 = 63.5	0.67%
13.4 x 6 = 80.4	0.25%	12.7 x 6 = 76.2	0.25%
13.4 x 7 = 93.8	0.09%	12.7 x 7 = 88.9	0.09%
13.4 x 8 = 107.2	0.03%	12.7 x 8 = 101.6	0.03%

Thicknesses of 200nm or more have marginal increases in effectivity which is why a thickness of 100nm has been chosen for this dissertation. Other publications have used similar thicknesses for similar reasons as shown by [107].

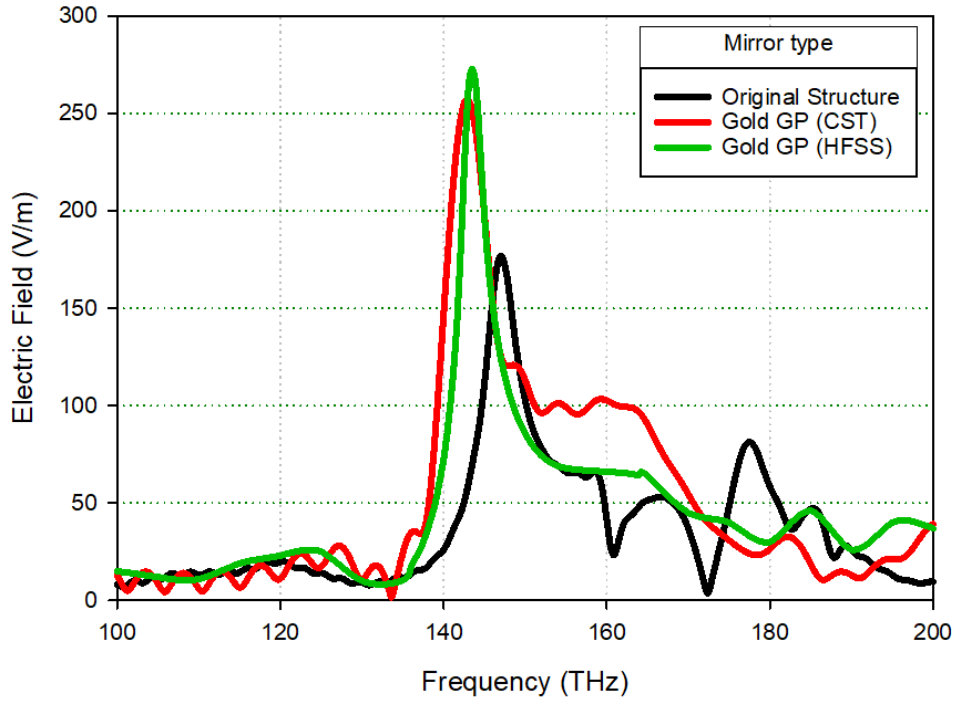

Figure 4.9: The electric field in the dipole gap for two electromagnetic solvers for a mirrored structure on a gold ground plane

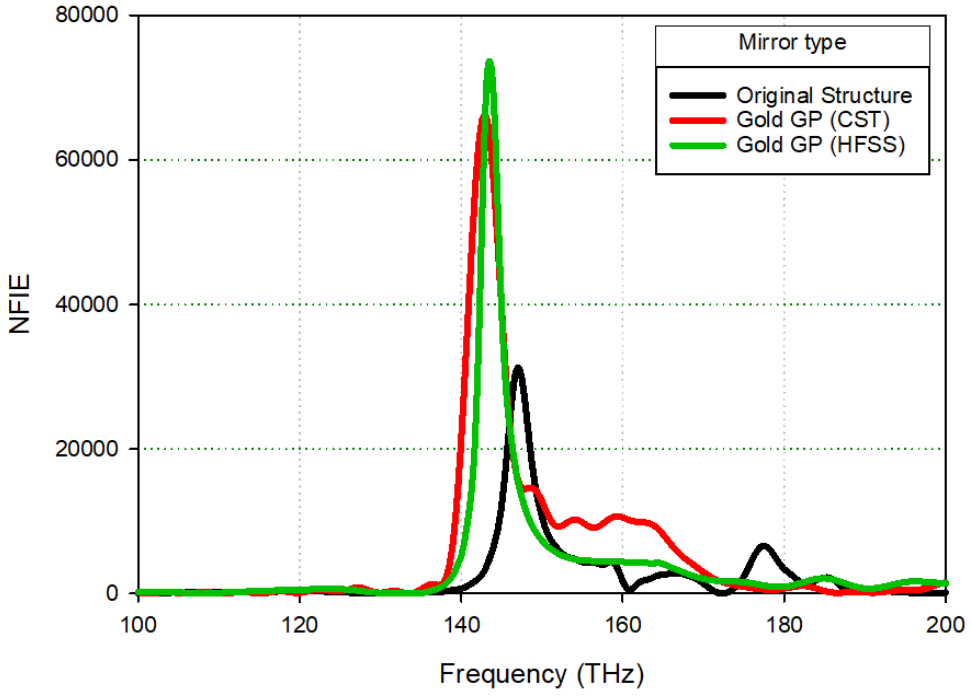

Figure 4.10: NFIE for two electromagnetic solvers for a mirrored structure on a gold ground plane

The accuracy of the results obtained in CST is further supported by simulating the same structure in HFSS and a small difference is obtained where HFSS has a maximum electric field of 270 V/m at 143 THz as opposed to CST with a maximum electric field of 260 at 142 THz as illustrated in Figure 4.9. The NFIE results from both electromagnetic solvers are subsequently 68k in CST and 73k in HFSS as displayed in Figure 4.10. There is a discrepancy, but the error can be attributed to differences in mesh size that can easily account for the 7% NFIE error. The relative consistency in the results supports the results of the simulations and could be tested experimentally in future works.

4.1.2 Mirror along X-axis

The hybrid dipole and dielectric cavity structure can also be mirrored along the side axis to halve the volume in a different way which is visible in Figure 4.11. The side-mirrored structure with an ideal electric mirror doubles the electric field from 180 V/m to 360 V/m as expected. However, the gold side mirror has large losses that are attributed to its highly lossy nature, as well as the angle of the incident light which is not optimal for reflection on the gold surface in this frequency range, and this reduces the resultant electric field to 170 V/m which is a value below that of the original structure. The results in Figure 4.12 clearly indicate how the side-mirrored structure with a gold GP has inferior NFIE compared to the original DRC, but the difference in enhancement is not large while still having an advantage in terms of volume reduction. Although the use of a side mirror shows promise, it requires a mirror that can perform well at perpendicular angles which can be explored in future works.

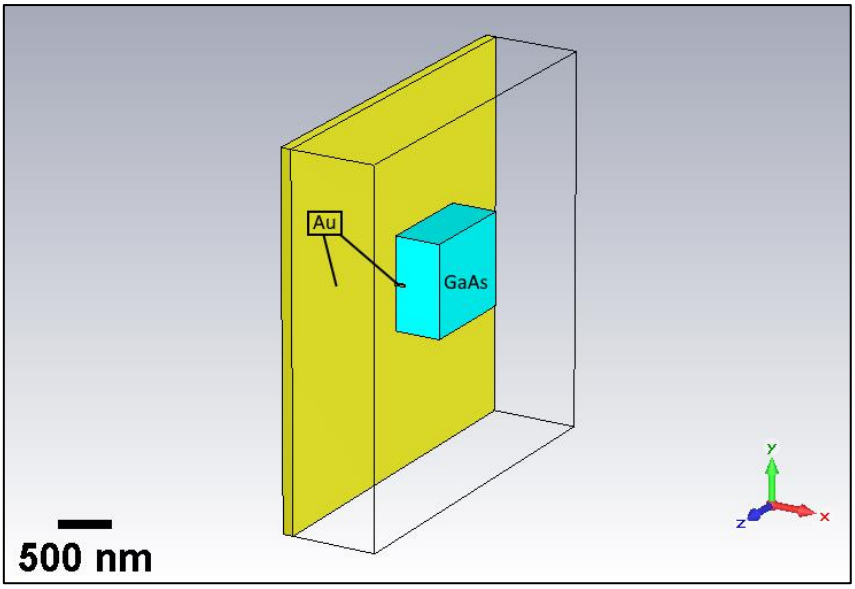

Figure 4.11: Proposed structure mirrored with a gold sheet along the side-axis

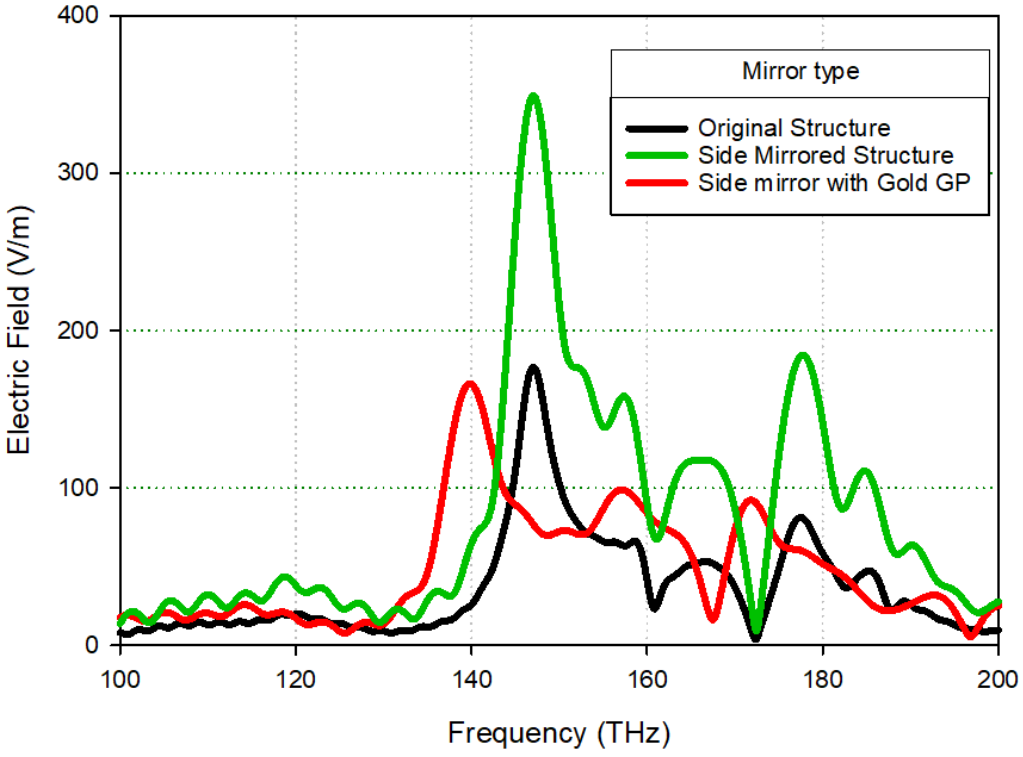

Figure 4.12: Resultant electric field for the structure mirrored along the YZ-plane

The use of metallic mirrors as both a ground plane mirror and a side mirror have shown that it is possible to halve the volume of the proposed structure while still maintaining or even improving NFIE. This effect can be generalised to other nanoantenna designs, and the bowtie design is simulated to confirm this.

4.1.3 Mirrored Structure with Bowtie Nanoantenna

Mirroring a structure with a gold bowtie on a dielectric cavity, as seen in Figure 4.13, yields the same conclusions that were previously found with a dipole, which is that a perfectly mirrored structure can double the electric field and that the use of a gold ground plane introduces losses to the design. Figure 4.14 and 4.15 show a significant increase in electric field to 560 V/m and NFIE to ~320k for a gold bowtie and GaAs DRC over a gold ground plane. Although metallic mirrors can improve the NFIE, there are still high losses associated with these materials. Therefore, to further improve the NFIE with mirrors, alternatives to metallic mirrors must be used that have high reflectivity, and promising candidates for this are dielectric mirrors such as Bragg reflectors and photonic crystals.

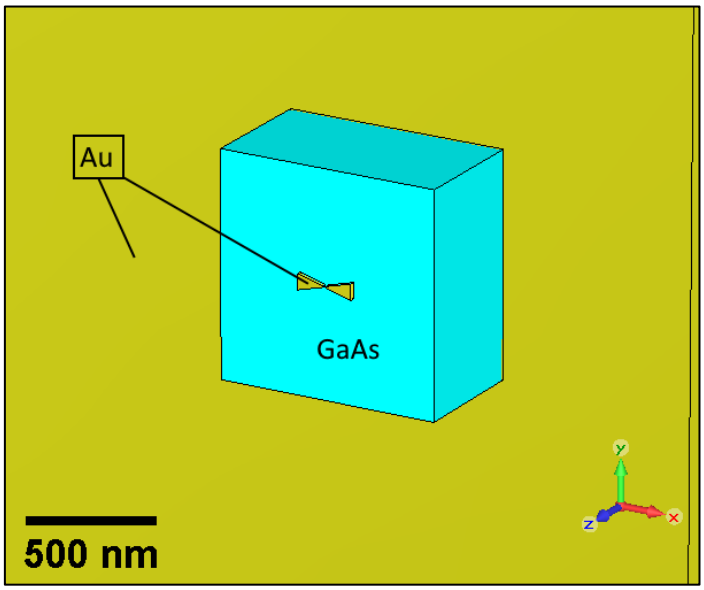

Figure 4.13: Bowtie on a dielectric cavity mirrored on a gold ground plane

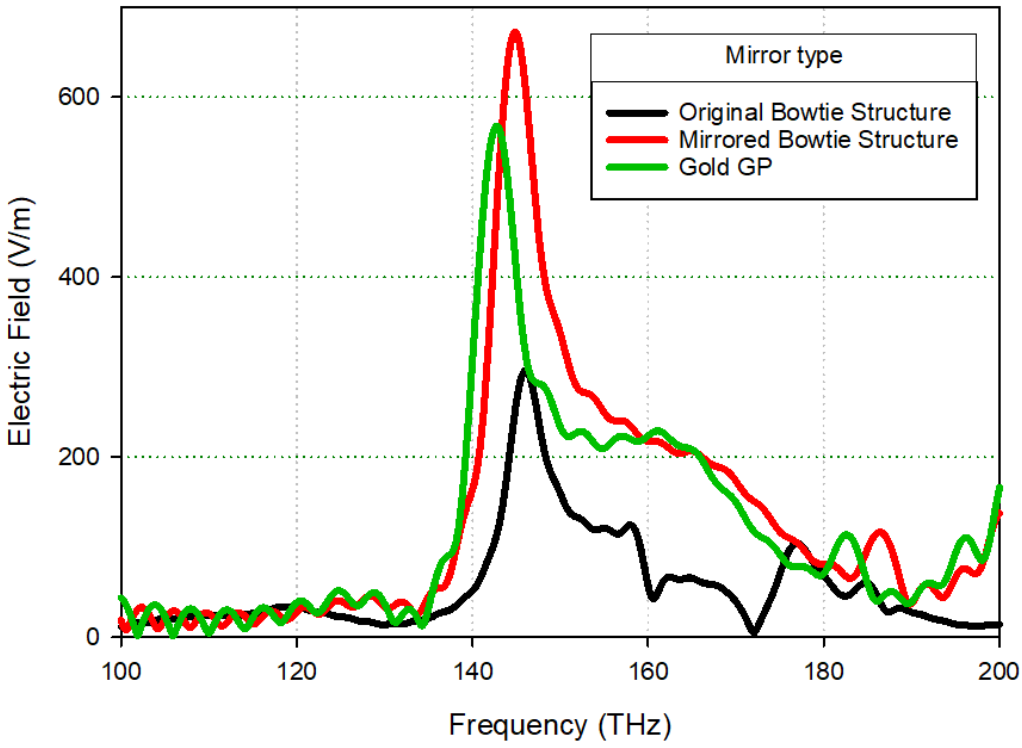

Figure 4.14: Resultant electric field for the bowtie structure mirrored with a ground plane

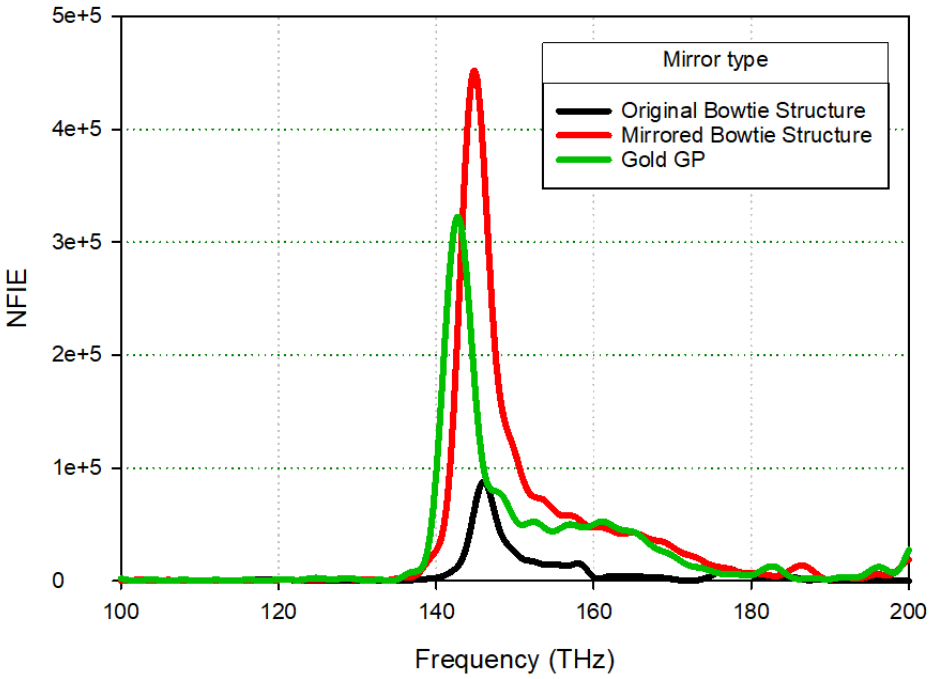

Figure 4.15: NFIE of the bowtie structure mirrored with a ground plane

4.2 One Dimensional Dielectric Mirror: Bragg Reflectors

Distributed Bragg Reflectors (DBRs) are designed based on the partial reflectance that occurs as light travels from a medium of one index to another. A single layer of a dielectric surface can only reflect a small amount of the incident light, but the use of multiple stacks of alternating high and low index medium materials can have very high reflectivity of >99.9%. The reflections are kept in-phase with constructive interferences by making sure that the thickness of each layer is tuned to a quarter wavelength of the target resonant frequency. The DBR has already been discussed in Chapter 1 and it has a strong limiting technical factor, which is the functional angles of reflection. Due to its design, light that enters the DBR at different angles have a probability to be reflected in another direction which does not assist the intended constructive interference. Even worse, at certain incident angles, the light may not be trapped and may exit the DBR in another direction [108], [109]. This is dependent on the angle of incidence and can be undesirable but is irrelevant for certain applications where the incident angle can be configured to ensure maximum reflectivity. The optimized structure from Chapter 3 has been placed on a Bragg reflector with a low-index top layer which has the effect of positioning the dipole a quarter wavelength above a ground plane, thus doubling the incident electric field.

Figure 4.16 illustrates the proposed configuration with a low-index top layer DBR beneath the hybrid plasmonic nanoantenna and dielectric cavity structure. The low-index top layer has a refractive index of n=1.5, whereas the GaAs cavity has an index of n=~3.3. The large difference in the refractive indices increases the isolation of the dielectric cavity and nanoantenna combination whilst still providing a dielectric mirror that reflects the incident light and theoretically doubles the strength of the light incident upon the nanoantenna. The number of DBR layer pairs is set to 7 with a surface area of 3000 x 3000 nm^2 and the thickness of the low index layers is calculated to be 333 nm while the thickness

of the high index layers is calculated to be 151 nm. The reflectivity of the DBR is calculated to be R>99.99% based on Equation 1.17 and 1.18.

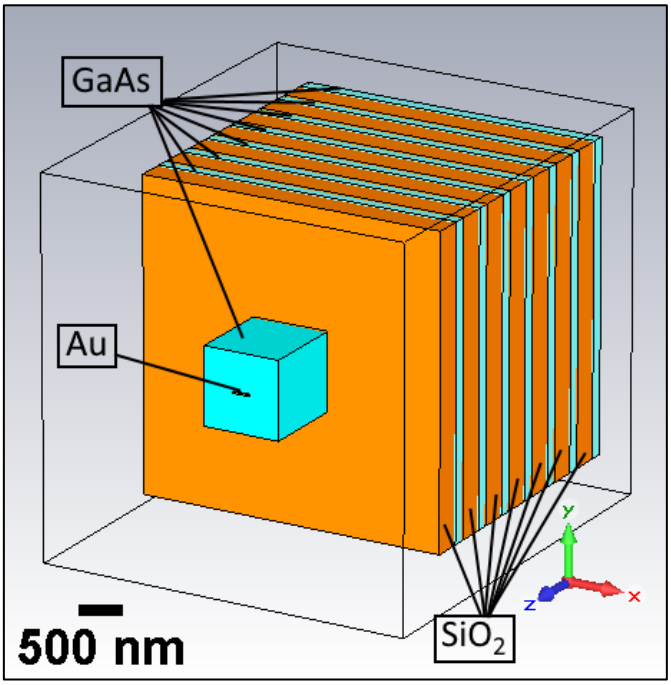

Figure 4.16: Proposed structure on a low-index top layer Bragg reflector

Table 4.2: Calculated Reflectivity of Bragg Reflector

Number of layer pairs, p	Admittance, Y	Reflectivity, R (%)
1	15.97	77.820
2	77.30	94.957
3	374.15	98.937
4	1810.90	99.779
5	8764.77	99.954
6	42421.51	99.991
7	205320.10	99.998

A near 100% reflectivity should have doubled the electric field in the nanoantenna gap from 180 to 360 V/m. However, the coupling between the dielectric cavity and BR

causes some losses and distorts some of the reflected light, which leads to the result shown in Figure 4.17 where it is noted that replacing the gold ground plane by the Bragg reflector has noticeably improved the electric field in the nanoantenna gap from 260 to 300 V/m. This is a measurable improvement of 15% and this improvement is exacerbated in Figure 4.18 leading to a NFIE of 90k for the DBR design compared to a NFIE of 65k for the gold mirror design. The dielectric mirror has advantages in terms of reduced metallic losses, but still has losses from the maximum theoretical result obtained using a PEC mirror with a NFIE of 100k. This is due to a number of factors, not least that the DBR low-index layer has been simulated using an experimental lossy model for silicon dioxide, and the high-index layer utilizes the same lossy gallium arsenide experimental model used for the DRC. These lossy models distort the reflected frequency and reduce the coupling effects due to resonance shifts. The design has also only been optimized in increments of 10 nm to replicate the fabrication capabilities of most current technologies, even if changes of 1 or 2 nm might have given higher gains. This is in addition to the impact of coupling between the DBR and dielectric cavity, which alters the optimum reflectance. Due to these factors, the structure with the DBR is unable to couple properly at resonance between the various components, which leads to the suboptimal results in Fig 4.18, which must be noted are still significantly better than the results utilising a gold mirror.

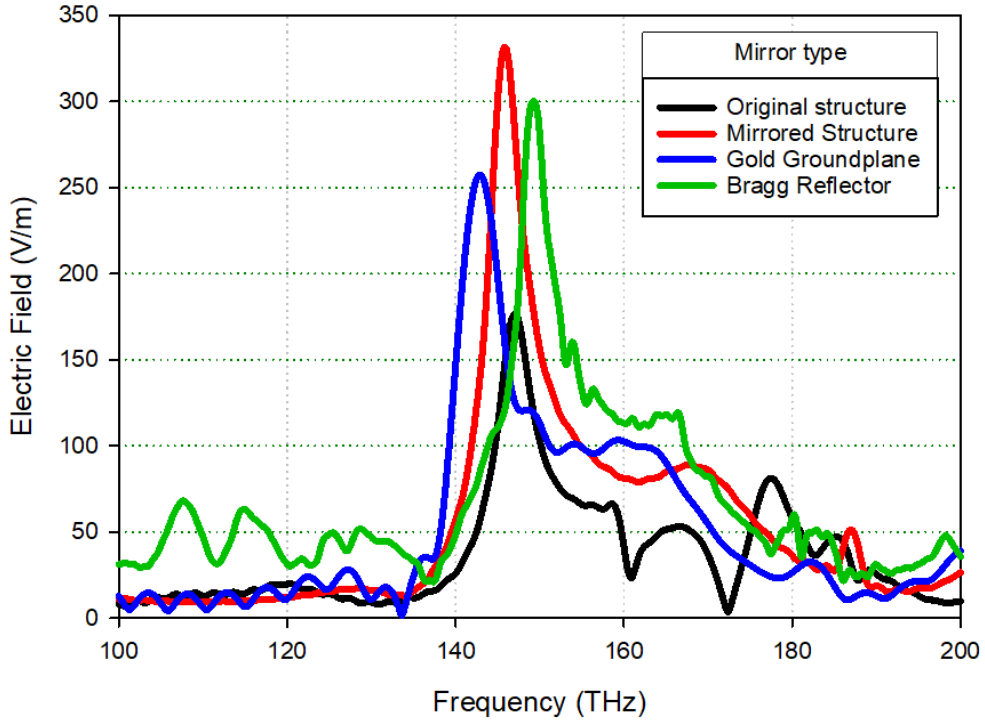

Figure 4.17: Electric field comparison of various design types

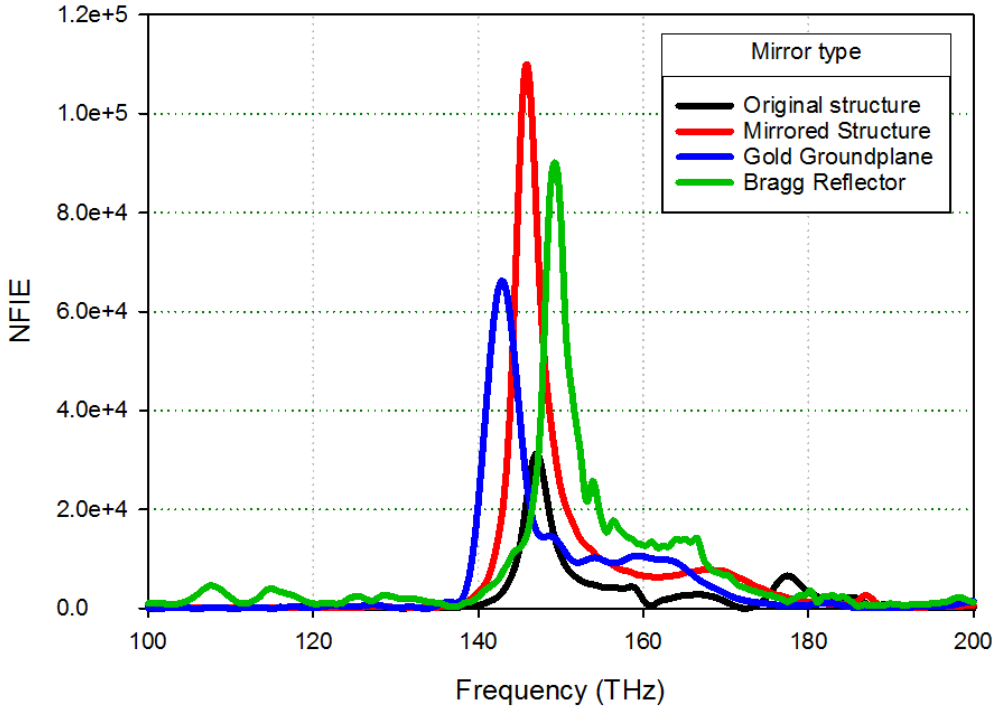

Figure 4.18: NFIE comparison of various design types

The one-dimensional dielectric mirrors have limitations in terms of the functional reflection angle. Even a slight deviation of 5 degrees in the incident light angle cannot be tolerated and could result in a total loss of, or significant reduction in, the reflectivity. Several more angle independent photonic mirrors have been proposed in the form of mutli-dimensional photonic mirrors [110], [111]. However, this work does not focus on multi-dimensional photonic crystals and assumes their performance is comparable to or lower than that of the Bragg reflectors with the added bonus of having high reflectance over a wider range of incident angles. In fact, some studies have reported the performance of two and three dimensional photonic mirrors at a reflectance of ~90% [112], which is weaker than the maximum performance of Bragg reflectors that can have reflectance of >99.9%.

4.3 Low profile dielectric cavity

The use of mirrors in the proposed design is able to cut the thickness in half. However, it is well-known that the maximum value of an electric field is at a quarter wavelength above an electric ground plane. At the operating frequency, this would be equivalent to 500 nm in vacuum, or ~150 nm of effective length when the relative permittivity of gallium arsenide is considered. A dielectric cavity of this thickness would be considered a low-profile design when compared against the DRAs from which they were inspired. Low profile dielectric resonator antennas are useful in certain applications where the thickness of the design is important and could negatively affect performance. However, as the nanoantenna gets closer to the ground plane, the image effects become more apparent. It was previously shown [113] that the image dipole can have strong effects on the source dipole and these interactions had to first be confirmed in the simulations to understand the subsequent results.

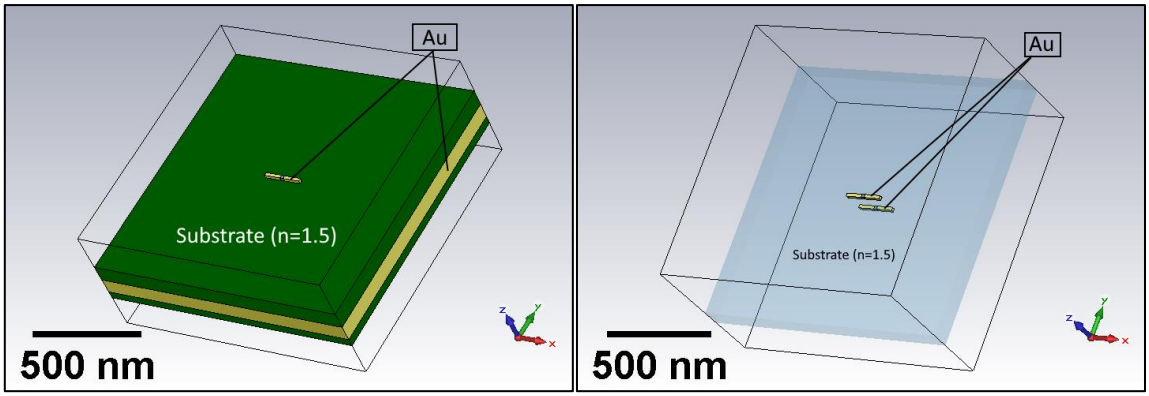

a) b)

Figure 4.19: Design of a gold dipole nanostrip above a) a ground plane and b) a second dipole nanostrip.

The first design in Figure 4.19(a), has a dipole nanoantenna excited by a plane wave that was placed on a thin substrate of $\mathcal{E}_r = 2.25$ and thickness of 100 nm above a gold ground plane with a thickness of 150nm. The thickness of the substrate was varied between 15 nm to 200 nm, which, with the image effects, equalled a separation distance of 400nm between the source and image dipole. The maximum electric field in the gap was recorded to understand the coupling effects between source and image dipole. In the second design in Figure 4.19(b), two source dipoles were separated by a substrate where the thickness and the separation distance were varied.

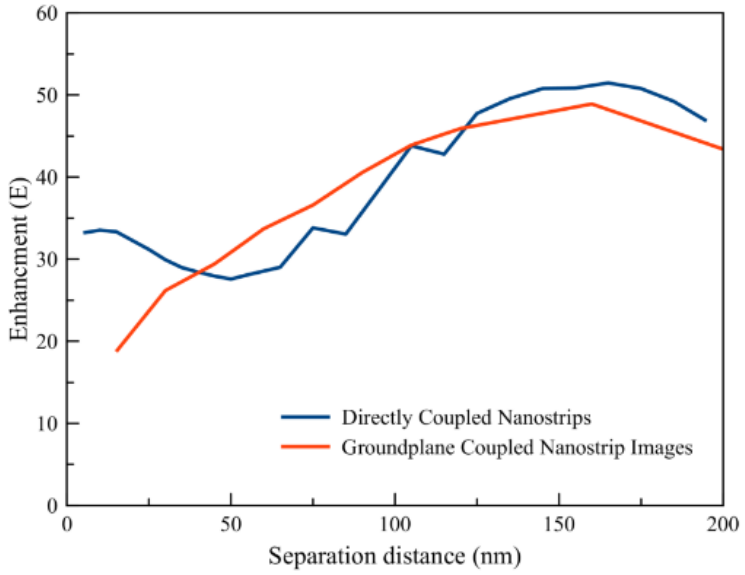

Figure 4.20: Comparison of directly couple nanoantennas against image coupled nanoantennas

Figure 4.20 illustrates that the behaviour of both designs is strongly correlated thus showing that the nano-dipole above a ground plane does follow coupled image theory. A secondary analysis can also be made that the coupling yields the strongest effect at a separation distance of 165 nm from the ground plane, or 330 nm between the two dipoles, with a resonance frequency of ~300 THz. Traditional antenna theory places a half-wavelength minimum spacing between two array elements which is in line with the results obtained where the effective distance after including the dielectric substrate is:

$$\ell_{eff} = \ell \times n \tag{4.1}$$

The effective separation is thus equal to 330 x 1.5 = 495 nm which is equivalent to half the wavelength at 300 THz, which is 1000 nm. The low-profile dielectric cavity is therefore found to have array effects due to coupling with the image through the ground plane.

Based on these results, the original proposed structure is too thick at 1000nm and even the mirrored structure is still too thick at 500nm. To obtain the image coupling effect, the low-profile dielectric cavity resonator must have a thickness of ~150 nm when placed above a ground plane. Utilizing the MATLAB script found that to obtain higher TE modes at lower thicknesses, the surface area of the resonator must be enlarged to compensate for the volume lost from the thickness. Numerical analysis and simulations showed that a low-profile dielectric cavity would have a strong resonance at 150 THz with dimensions of 3000 × 3000 × 300 nm. The thickness of 300nm would be halved to 150 nm when a ground plane is employed. The parameters were optimized through simulation and a mode was found at ~140 THz for a low-profile (LP) cavity made from GaAs with dimensions of 2800 x 2800

x 340 nm. This design could be placed above a ground plane and the thickness halved to have the dimensions of 2800 x 2800 x 170 nm as shown in Figure 4.21.

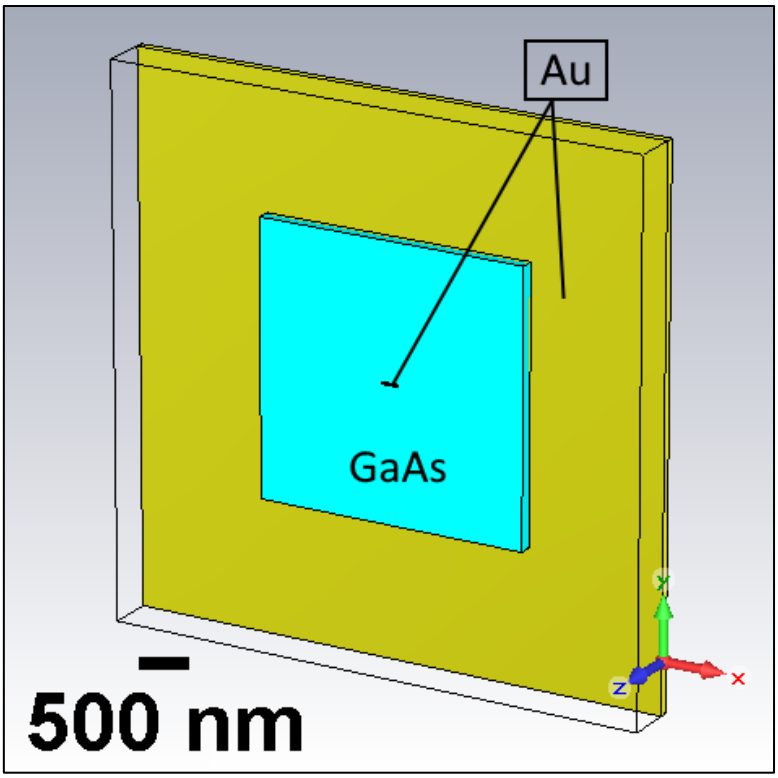

Figure 4.21: Low-profile dielectric cavity on a ground plane and coupled to a gold dipole

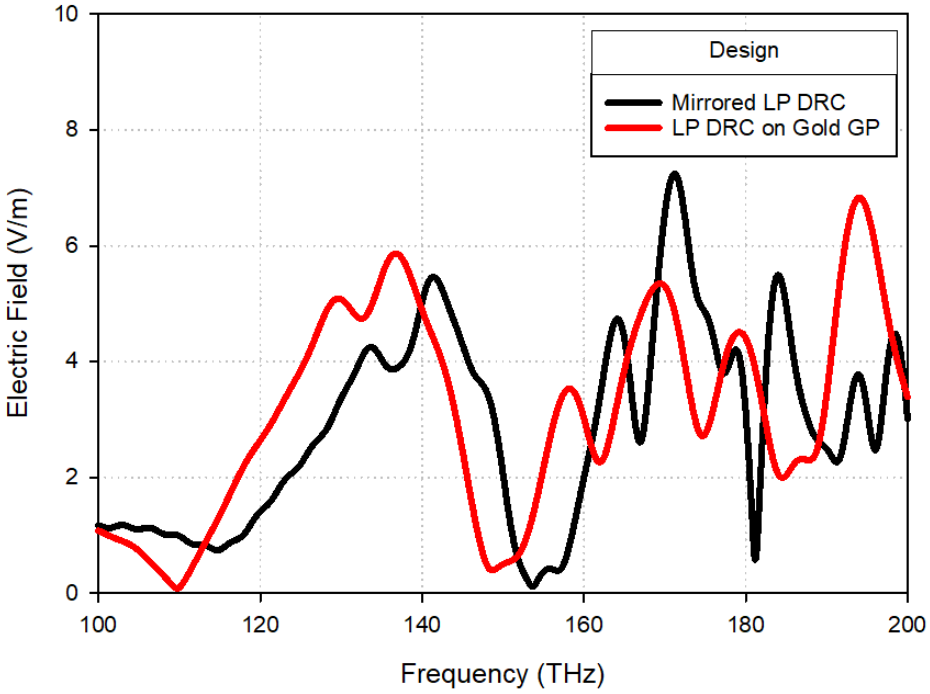

Figure 4.22: Resultant electric field of the low-profile cavity with ideal electric mirror and gold ground plane.

The LP cavity design was mirrored and a resultant electric field of ~5.5 V/m was found for an ideal ground plane made of PEC and the simulation was also run for a gold ground plane as illustrated in Fig 4.22. The reduced thickness of the LP DRC brings the DRC surface close to the ground plane with a distance of only 170 nm, which is close enough to be affected by the plasmon resonance of the gold ground plane. Therefore, the LP cavity on a gold GP shows an increased electric field as compared to the ideal ground plane. This is in stark contrast to the proposed DRC in Chapter 3, where the thickness of 500 nm prevented any plasmonic effects from affecting the DRC surface or the gold dipole on the surface. It was therefore expected that the gold GP structure would have a significant NFIE when coupled with a gold dipole.

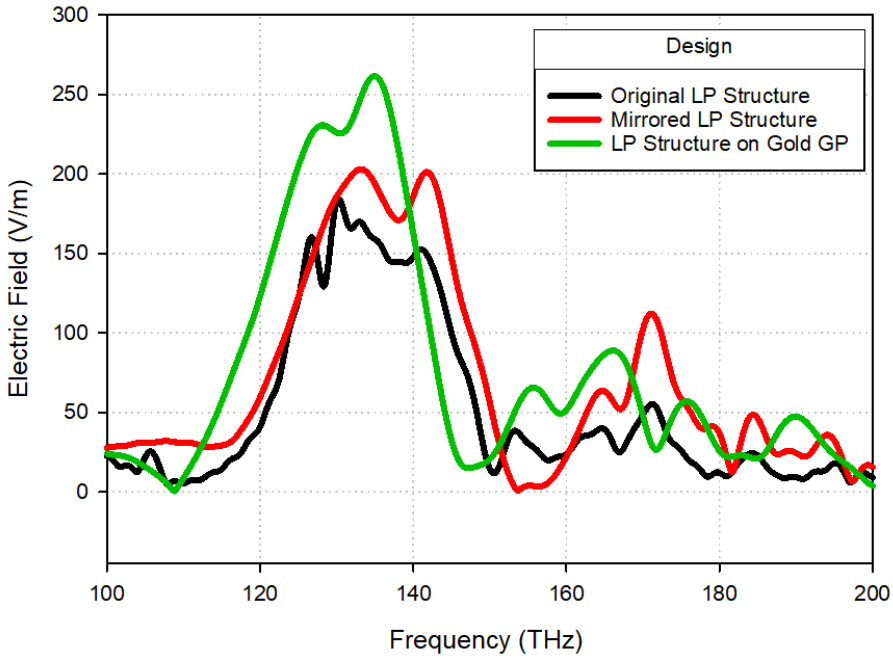

Figure 4.23: Resultant electric field of a gold dipole placed above a low-profile cavity over a ground plane.

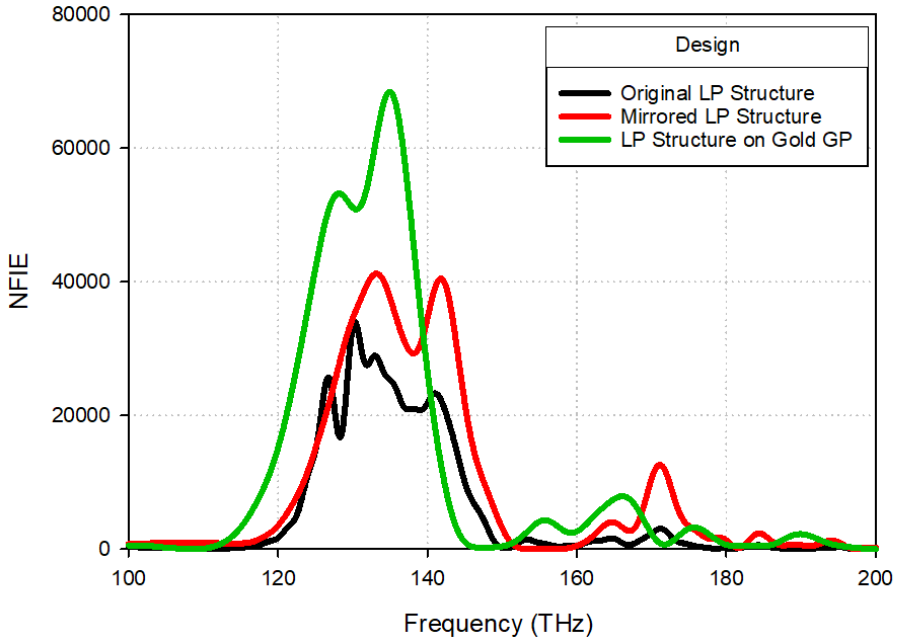

Figure 4.24: NFIE of a gold dipole placed above a low-profile cavity over a ground plane

The mirrored structure was coupled with a gold dipole on the LP cavity surface which yielded a NFIE of ~40k. This is close to the NFIE of ~37k obtained when coupling with the thicker dielectric cavity proposed in Chapter 3. To address real-world feasibility, the PEC ground plane is replaced with a gold ground plane with dimensions of 9000 x 9000 x 100 nm. However, this shifts the resonant mode of the cavity from ~140 THz to ~130 THz. The low-profile cavity of 2800nm × 2800nm × 170nm has an electric field amplitude of 6 V/m at ~135 THz as shown in Figure 4.22. This mode was coupled with the gold dipole and a resultant electric field of 260 V/m was obtained in Fig 4.23, corresponding to an increase of NFIE to ~68k as illustrated in Fig 4.24. This is still a lower NFIE when compared to the proposed DRC mirrored with a gold ground plane that achieved a NFIE of ~110k. Low-profile dielectric cavities could therefore be useful for certain applications where a trade-off can occur for half the NFIE at around half the thickness of 270 nm versus 600 nm.

4.4 Fabry-Perot Structures

In the previous pages, a single mirror has been used to accomplish further improvement in the NFIE. This concept can be extended by placing two mirrors on either side of a plasmonic antenna configuration to create the well-known Fabry-Perot resonator that is commonly used in lasers. The Fabry-Perot principle is based on creating a gap with mirrors placed at an optimum distance on both sides of a source, which should trap the plane wave in between the two surfaces, thus increasing the incident electric field considerably and consequently increasing the NFIE by a corresponding amount. A Fabry-Perot cavity can be created by implementing a Bragg reflector with a quantum dot emitter placed in the middle layers, which would effectively create mirrors on both sides of the emitter. However, this dissertation attempted to continue the previous design of utilizing a gold slab in order to reduce the thickness of the design. Placing gold slabs on either side of a gold dipole can create a Fabry-Perot cavity and a plane wave can be directed by the incorporation of slits or air gaps in the gold slab [63].

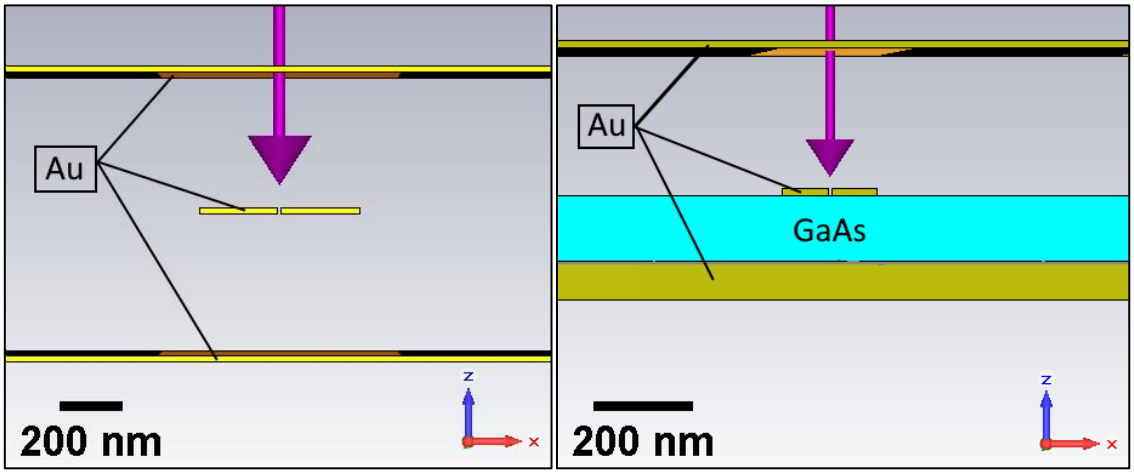

(a) (b)

Figure 4.25: Fabry-Perot design of a gold dipole between two gold slabs with a) an arm length of 250 nm, b) an arm length of 90nm and a low-profile dielectric cavity.

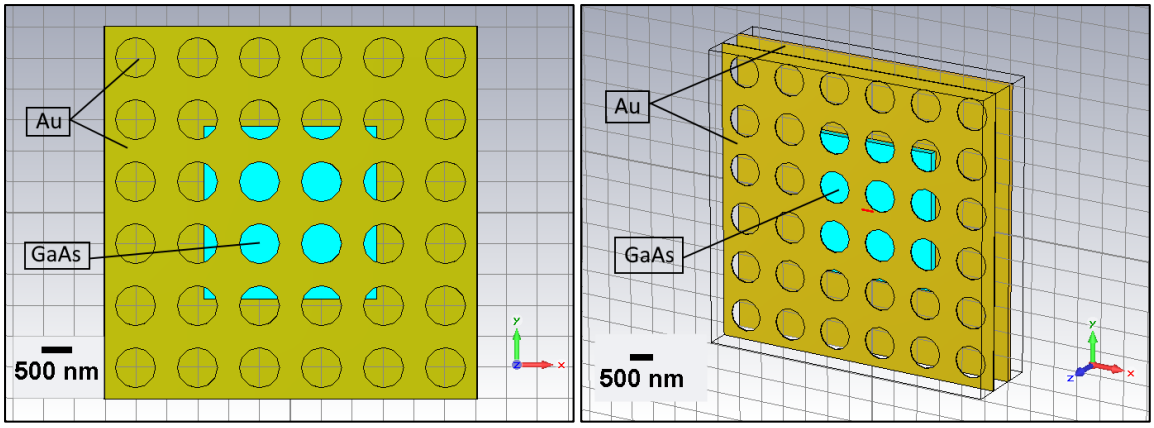

Figure 4.26: Air gaps in the gold slab to allow higher illumination [63].

The distance between the gold slabs is set to half the operating wavelength, and a gold dipole is placed in the centre at a quarter-wavelength above the lower ground slab, which is where the strongest resonance would occur [45]. The resonance frequency has been chosen as ~150THz which yields a wavelength of 2000nm and a gold slab separation distance of 1000nm. In simulations, the plasmonic properties of gold shifted the optimum separation distance to 850nm. A gold dipole with an arm length of 250 nm has been placed midway between the two gold slabs to resonate at the operating frequency as illustrated in Fig 4.25(a). Air gaps are required to allow illumination to pass through the top gold layer and is displayed in Fig 4.26.

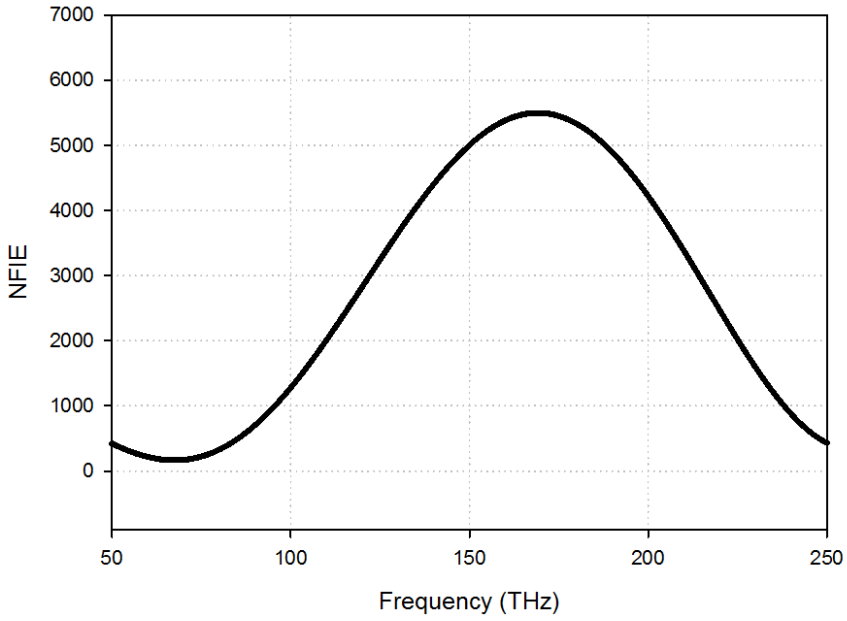

(a)

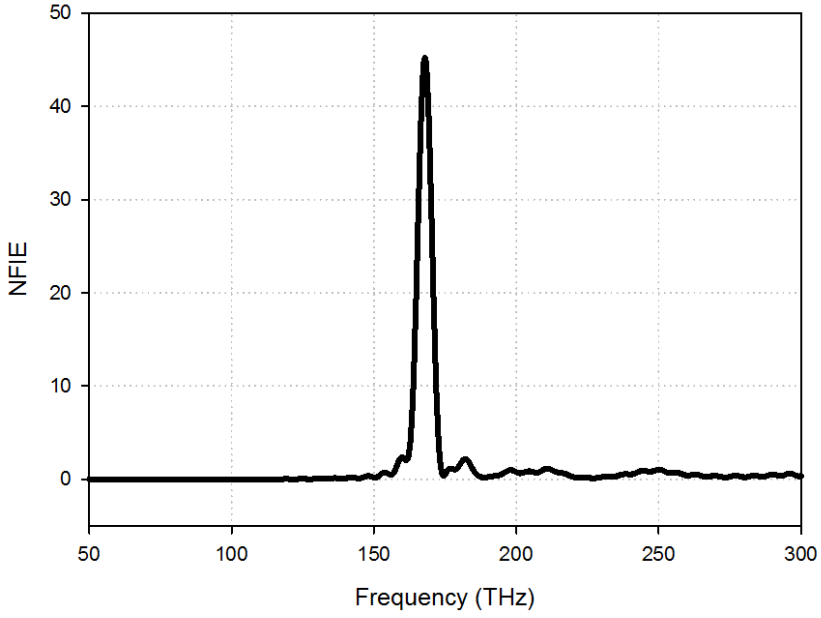

(b)

Figure 4.27: NFIE of a) an isolated gold dipole with arm length of 250 nm and b) an isolated Fabry-Perot cavity with separation distance of 850 nm.

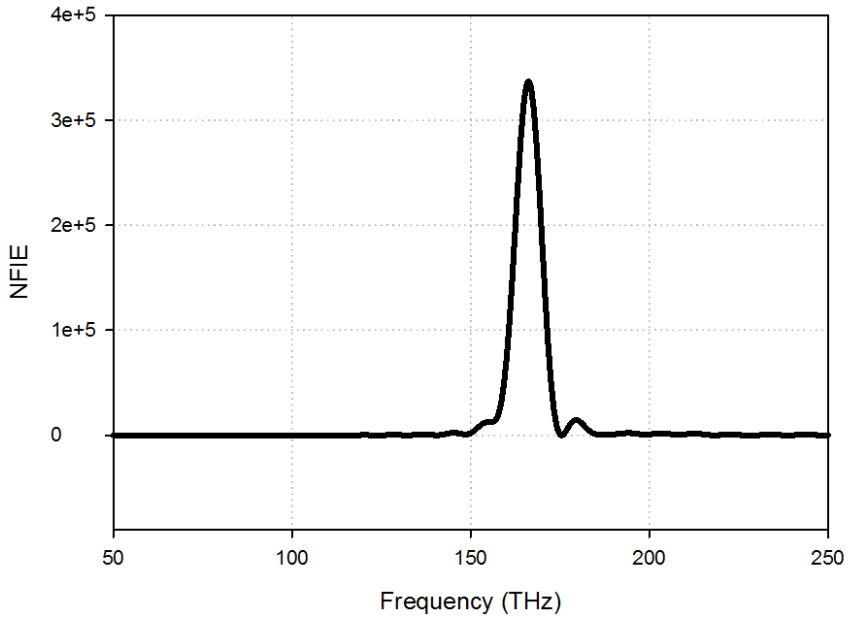

Figure 4.28: NFIE of a gold dipole with arm length of 250 nm in a Fabry-Perot cavity with separation distance of 850 nm.

Figure 4.27 illustrates a maximum NFIE of 5.5k for an isolated dipole compared to a NFIE of 45 for the Fabry-Perot (FP) cavity at the absence of the plasmonic dipole. However, when the dipole is placed at the centre of the FP resonator, an electric field of ~500 V/m would be expected at the nanoantenna gap, which corresponds to a NFIE of 250k at 160 THz as demonstrated in Figure 4.28. Theoretically, the combination of the DRC in a FP cavity would yield significant increases in NFIE. However, the relatively small size of a FP cavity places constraints in terms of the size and thickness of the dielectric cavity. Instead of the proposed DRC from Chapter 3, a low-profile dielectric cavity was placed below the gold dipole in the FP cavity as illustrated in Fig 4.25(b).

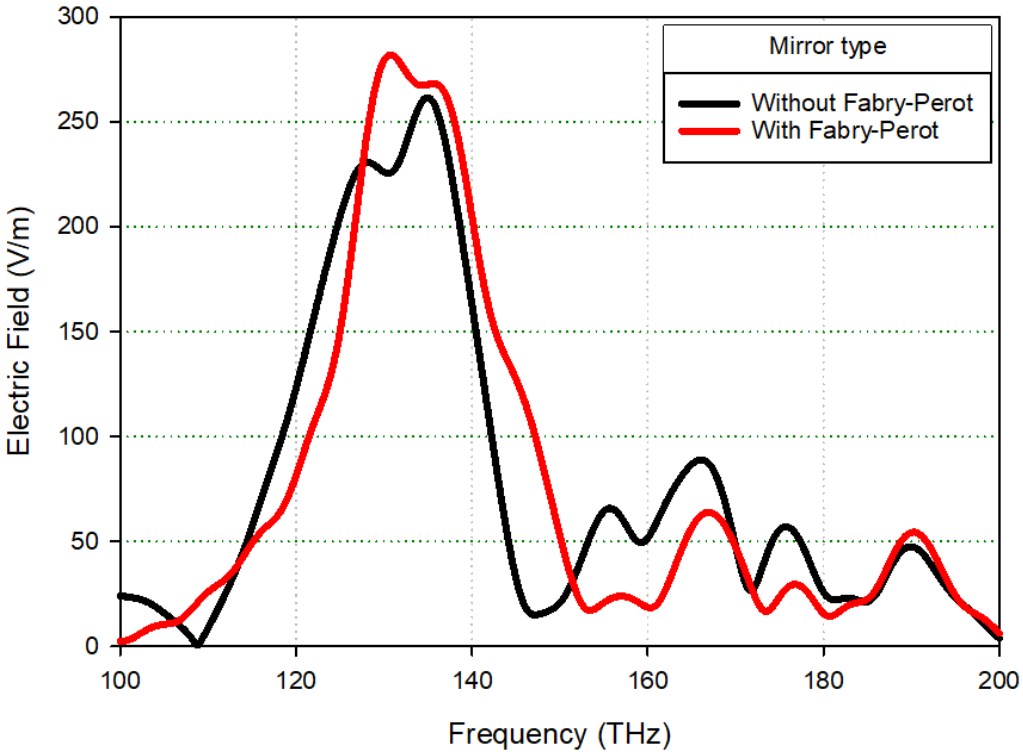

Figure 4.29: Resultant electric field for a LP cavity confined in a FP cavity

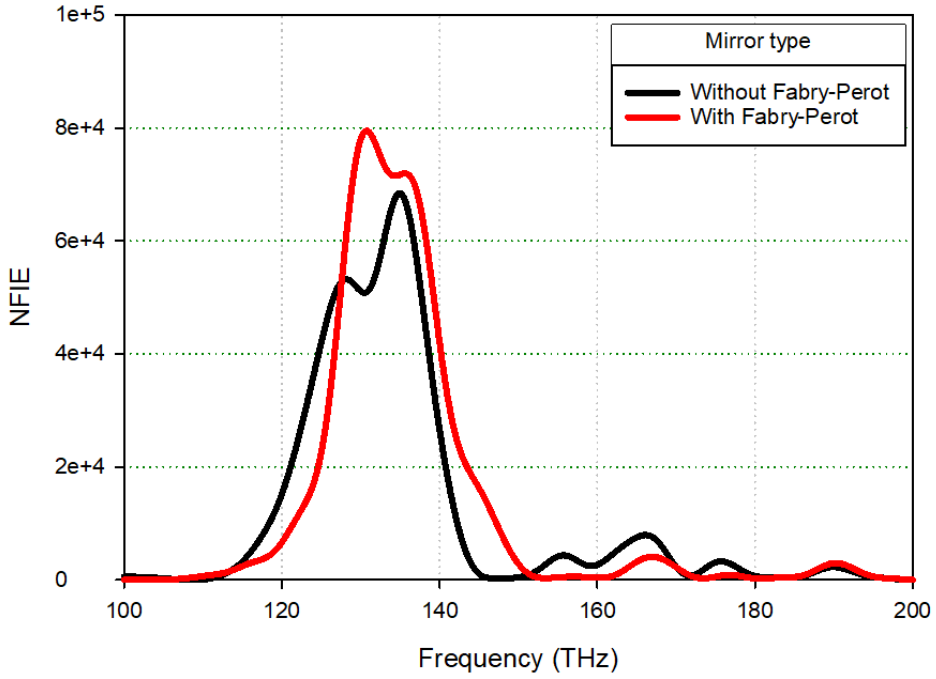

Figure 4.30: NFIE of a LP cavity confined in a FP cavity

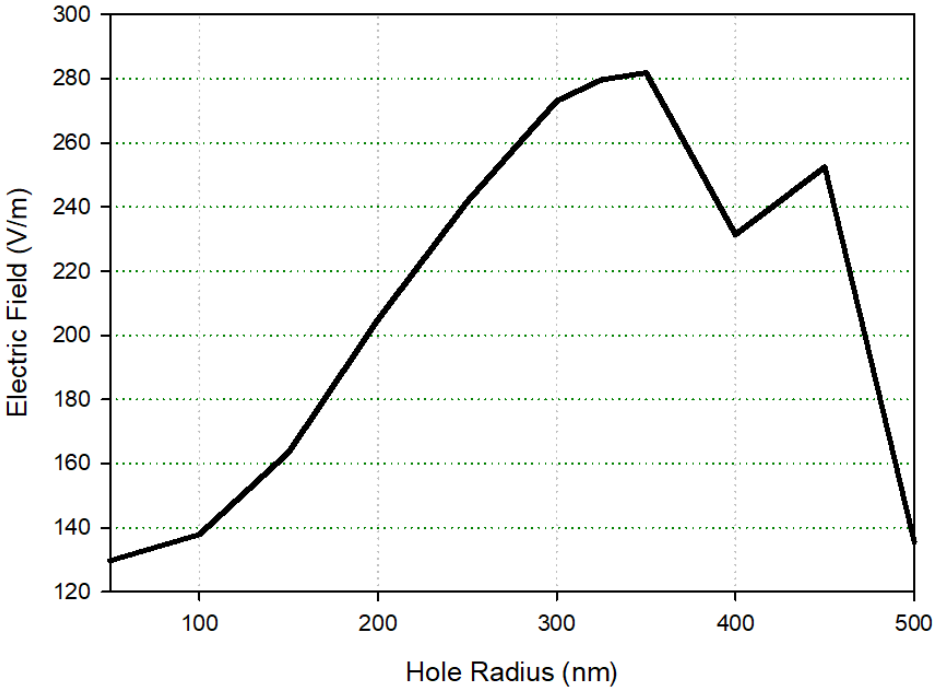

Figure 4.31: Effect of hole radius on the FSS to maximize the operation of the FP cavity

The introduction of the LP DRC was found to reduce the NFIE in the dipole gap unless the parameters were highly optimized. The dipole was configured with an arm length of 90 nm, and thickness of 20nm; the LP DRC was configured with GaAs, dimensions of 2800x2800x170 nm placed firmly against the lower gold slab; the lower gold slab had dimensions of 6000x6000x100 nm; the FP gap was set as 600nm; and the upper gold slab had holes of radius 350 nm at intervals of a=1000 nm. Two of these parameters require further analysis, namely the FP gap and the holes in the upper gold slab. The FP gap of 600nm comprises of a 430 nm air gap on one side of the gold dipole and a 170nm LP cavity on the other which is thin due to the refractive index difference of the GaAs material compared to air. The ideal gap should have been 550 nm + 166 nm but this has been shifted due to the plasmonic property of the gold slabs. The lower gold slab was used as a metallic mirror, but the upper gold slab was designed as a Frequency Selective Surface (FSS) to allow the input of incident light into the FP cavity. The FSS was optimized to reflect and

keep in the electromagnetic radiation at the operating frequency by setting the hole radius to 350 nm. Unfortunately, Figure 4.29 illustrates that even after optimization, the FP design that was applied did not have a significant increase in the resultant electric field and Figure 4.30 displays a NFIE of ~80k, which is still less than the mirrored DRC with NFIE of ~110k. In theory, a FP cavity should have increased the NFIE significantly, but all results indicate that the FP cavity design that was used was not optimal. Figure 4.31 illustrates attempts to improve the FP cavity by adjusting the FSS through varying the hole radius, but results show that shifting away from a radius of 350 nm would only reduce the resultant electric field further. Although this dissertation did not have significantly positive results when combining the LP and FP cavities, the theoretical background indicates that it should be possible and can be an avenue of future work.

4.5 Hemispherical Lens

Another method that could be used to increase the incident light is through the use of an optical lens. A lens design was adapted to the operating frequency range of ~150 THz and the results were predicted to have a significant increase.

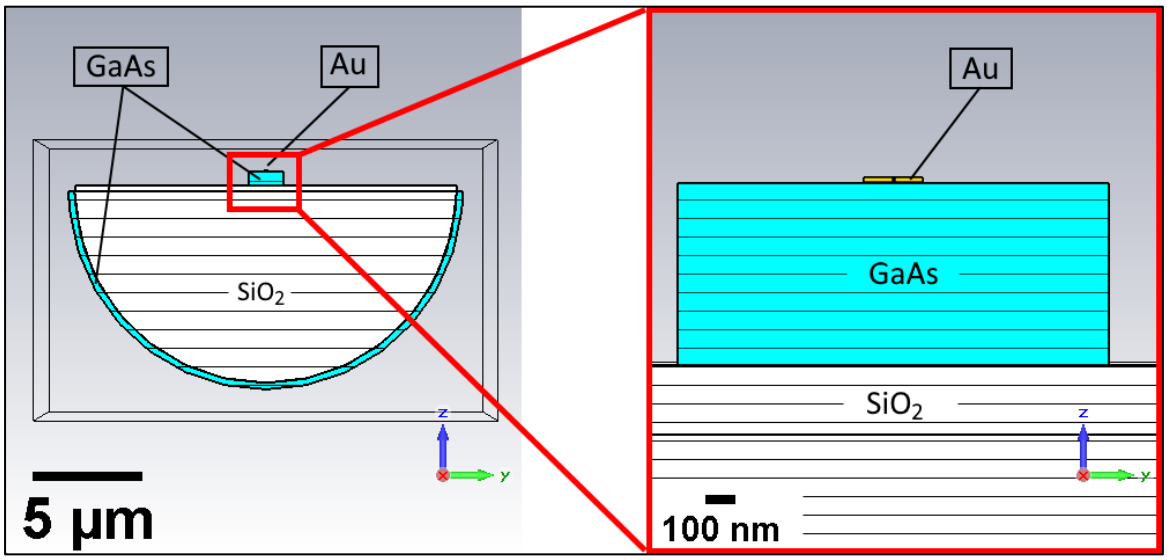

Figure 4.32: Optical lens coupled to a nano-dipole and dielectric cavity with plane wave travelling in the +Z direction

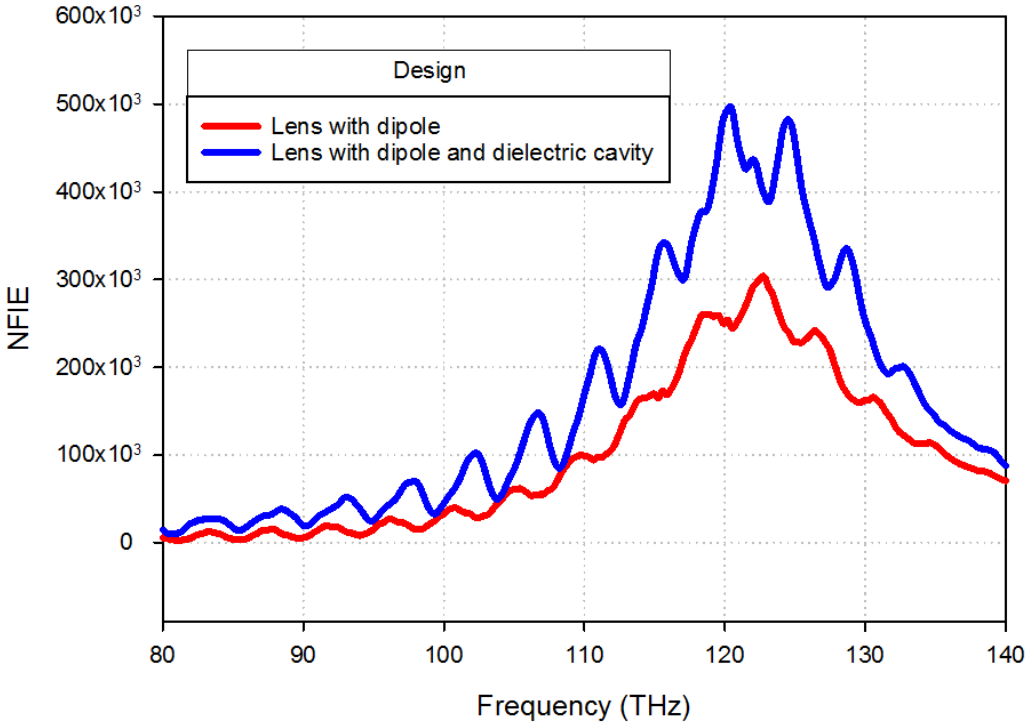

Figure 4.33: NFIE of a nanodipole and dielectric cavity coupled with an optical lens

A hemispherical lens with a radius of 8.6 µm was modelled to focus light at 150 THz as seen in Figure 4.32. The horizontal lines are due to the modelling in CST and have no significance. Instead, the design is based on a silicon dioxide hemisphere in a gallium arsenide shell. Additionally, a gallium arsenide rectangular dielectric cavity has been coupled on the flat side of the hemisphere. A gold dipole nanoantenna is further placed on the dielectric cavity. A plane wave was directed from below, travelling in the +Z direction, where the incident plane wave was focused by the lens, and further concentrated by the cavity and the gold dipole. The coupling of a dipole to the lens was found to increase the NFIE to 300k as illustrated in Figure 4.33. This further proves that light-focusing and light-trapping mechanisms are capable of linearly increasing the NFIE proportional to the increased incident light. An addition of the dielectric cavity in between the gold dipole and the lens enhances the NFIE further to 450k which is 12 times the NFIE obtained in Chapter

3 of 37k. Although this result is significant, the lens is extremely large as compared to the size of the plasmonic antenna and may not be ideal for most applications.

4.6 Conclusion

This chapter has further investigated the idea that the plasmonic enhancement can be directly manipulated in a linear and easily calculated manner through adjusting the strength of the incident light. Furthermore, various forms of light manipulation were investigated, including different types of optical mirrors as well as lenses, Fabry-Perot cavities and low-profile dielectric cavities. In each scenario, a large NFIE has been obtained by increasing the incident light on a gold plasmonic dipole. The results have supported the assumption of linear NFIE manipulation. It was found that each mechanism mentioned in this chapter is not mutually exclusive from the use of a dielectric cavity and the dielectric cavity proposed in chapter 3 can be inserted and combined with the mechanisms described in this chapter for even higher NFIE. Therefore, the results obtained in literature by other scholars who have used such mechanisms do not overshadow the proposed design in chapter 3, since the dielectric cavity in chapter 3 can be incorporated into those designs.

(This page is intentionally left blank)

Chapter 5: FDTD Numerical Simulation

The structures in the previous chapters have been simulated in two separate commercial electromagnetic solvers. However, an additional layer of corroboration would increase confidence in the final results. Experimentation was the first method considered but could not be carried out within the available timeframe due to logistical and financial issues. A numerical analysis approach was therefore considered, which could either be based on Method of Moments (MoM) or Finite-Difference Time-Domain (FDTD), which are the two viable solutions for creating a custom electromagnetic solver with the resources available to an individual.

MoM was first explored, utilizing FORTRAN and the Linear Algebra PACKage (LAPACK) framework. However, the code for LAPACK had not been updated for two years since November 2017 and there existed code conflicts with the code for this work.

An alternative was embraced, utilizing Python 3.7 and the MIT Electromagnetic Equation Propagation (MEEP) framework as well as the NumPy external dependency. This combination allowed for a flexible approach for numerical simulation while addressing the parameters of this work. However, this method does not use MoM but instead uses FDTD.

5.1 Finite-Difference Time Domain (FDTD)

A method of numerical analysis of plasmonic phenomenon that utilizes the FDTD method has been developed since 1966 [114]. It utilizes a conceptual design called the Yee Lattice that divides the electromagnetic flux into electric and magnetic vector field

components for each Maxwell's curl equations as well as utilizing staggered grids for both space and time.

When Maxwell's differential equations are examined, it is observed that the change in the electric field for the time derivative is dependent on the change in the magnetic field across space. Therefore, a time-stepping relation can be created that is the basis of the FDTD method where, at any point in space, the updated value of the electric field in time has been shown to be dependent on the stored value of the electric field and the numerical curl of the local distribution of the magnetic field in space.

Similarly, the relation can be reversed, and the magnetic field can be time-stepped. At any point in space, the updated value of the magnetic field in time is dependent on the stored value of the magnetic field and the numerical curl of the local distribution of the electric field in space. By discretely running iterations of the electric and magnetic fields, updated values can be obtained for each time-step that can simulate the propagation of a continuous electromagnetic wave. The corresponding data can then be stored in computer memory in a numerical grid for further processing.

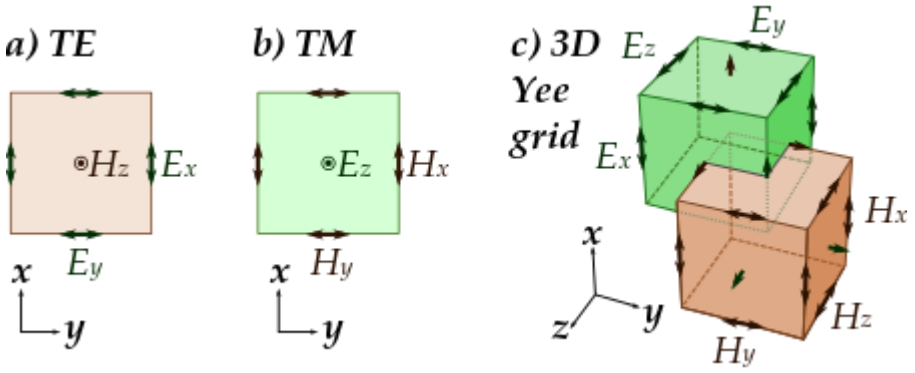

Figure 5.1: a) 2D grid of the electric field vectors b) 2D grid of the magnetic field vectors c) 3D staggered grid of both the electric and magnetic vector fields [115]

Figure 5.1 illustrates how a single Yee cell that is standardly used for FDTD is conceptualized, which consists of electric and magnetic field vector components that are set into a staggered grid design. A single cube is then designated as a voxel, with the magnetic field components placed normal to the faces of the cube while the electric field components are set as forming the edges of the cube. A complete Yee Lattice can be formed of multiple Yee cells, which creates a three-dimensional lattice. The interaction of an electromagnetic wave with this structure is controlled by mapping appropriate values of permittivity and permeability to each electric and magnetic field component.

This technique can be used for 1-D, 2-D, and 3-D FDTD techniques however, when multiple dimensions are considered, the time required for the calculations of the numerical curl will rapidly increase. This complexity was reduced by utilizing the concept of spatially staggering the electric and magnetic vector components into separate grids so that each electric field vector component was centred between a pair of magnetic field vector components, while each magnetic field vector component was conversely centred between a pair of electric field vector components. This method, known as the Yee Lattice, has proven to be very robust while simplifying the simulations a great deal, and remains at the core of many current FDTD software constructs. The Yee Lattice method is further improved by dividing the time steps into half steps whereupon the electric and magnetic field updates are staggered so that electric field updates can be conducted at a time-step between magnetic field updates, while the magnetic field updates are conducted in the time-step between electric field updates. This time-stepping method neatly eliminates the need to solve simultaneous equations, while furthermore yielding dissipation-free propagation of the electromagnetic wave. However, a negative effect of this method is that it limits the number of time-steps for each run to ensure numerical stability. Therefore, a large

simulation could require thousands of time-steps for completion, which places higher burdens on processing power and memory.

5.2 Using the FDTD method

The implementation of the FDTD solution of Maxwell's equations requires a computational domain to be established which defines the physical parameters over which the simulation is performed. The E and H fields can then be determined at every cell within the computational domain at any particular time-step. To aid this process, the space and time domains are divided into a number of cells according to the resolution required. The material of each cell in the domain is specified, by identifying the permittivity, permeability, and conductivity as required. Some of the materials typically used include free-space (used for air or vacuum), metals, or dielectrics.

However, in identifying the materials, there is a possible issue with declaring the permittivity of dispersive materials as discrete points, as the FDTD method requires the use of a curve equation to account for all possible points in a continuous plot. The discrete points of permittivity can instead be approximated using a formula, which can be from Debye, Drude, Lorentz or critical point terms. The table of permittivities for a particular material can therefore be divided into a number of sections, with the curve plot of each section being approximated by an equation. These equations do not have a meaning other than to approximate the permittivity curve plot of that material. This equation form can then be inserted into the Yee Lattice. However, this is simplified in our code due to the use of the MEEP external library which can take the permittivity values in tabular form and automatically construct the required approximation curve equations.

An electromagnetic source can be declared after the domain and the material models are confirmed. The source can be in a myriad of forms, including a current on a wire, or a

point source, or pulsed EM wave. FDTD can also be used to simulate light scattering from various shaped objects, as well as planar periodic structures and infinite periodic structures.

Since the E and H fields can be determined directly at any point, the output of the simulation can be stored as the E or H field at a point or a series of points within the computational domain. Running the simulation every time-step will evolve the E and H fields forward in time. The data from the E and H fields that are returned by the simulation can be further processed, whether after the simulation has ended or even while the simulation is ongoing. The FDTD technique robustly calculates the EM fields within a specified spatial region, which would limit it to near-field data. However, a technique can be employed using near-to-far-field transformations to also obtain scattered or radiated far-fields.

The FDTD method utilizes a particular algorithm to run the simulations, shown in Figure 5.2. The whole simulation area is first divided into discrete 3-dimensional unit cells with electromagnetic vectors (Yee Lattice) with each cell having its own initial conditions such as dielectric constant, permittivity, electrical conductivity, etc. In MEEP, the number of unit cells is based on the defined spatial resolution Δx, where a higher spatial resolution creates more unit cells per unit distance. The size of the discrete time-step Δt is defined by $\Delta t = S*\Delta x/c$, where S is the Courant factor, defined before the start of the simulation. Each cell then undergoes the flowchart shown in Figure 5.2. First, the E and H fields are obtained for staggered time steps, the H-field at $t=t_0$ and the E-fields at half a time-step before and after t_0.

This means that at runtime, t_0, the E and H are defined for every unit cell, with the initial conditions of E = 0 and H = 0, except at the defined sources. The sources defined in the model are given the appropriate values of E and H depending on the set parameters.

Next, the H-field at half time-step of $\Delta t/2$ after t_0 is calculated for all unit cells using the E and H-fields from previous time-steps. Afterwards, the E-field for all unit cells is calculated after $\Delta t/2$ using the E and H-fields from previous time-steps. Over each time-step, the transient fields from the source will propagate, thus changing the E and H-fields in the various unit cells. This completes one iteration of calculations. If the time is less than the ending time of the simulation, t_{fin}, then the next iteration is started and the calculations are repeated for the next time-step. This process continues until the time exceeds t_{fin}, upon which the algorithm ends.

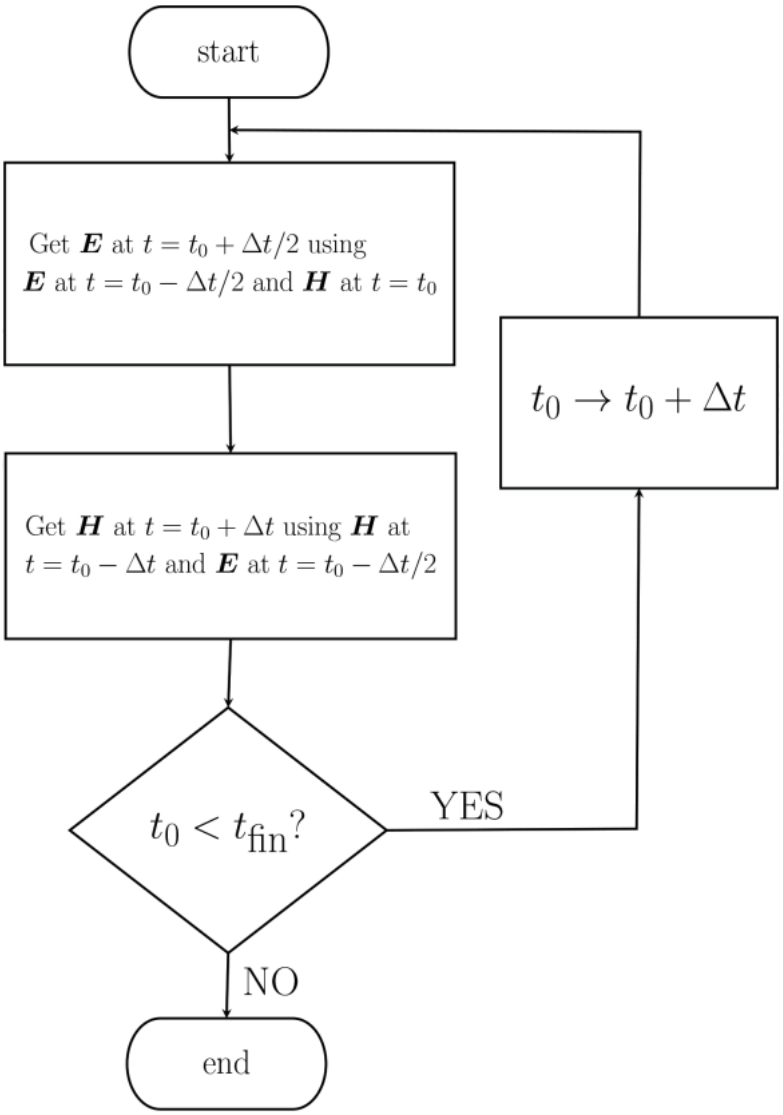

Figure 5.2: Flow of the FDTD algorithm

To increase the spatial resolution of the algorithm, the Yee Lattice grid sizes are made smaller, which increases the spatial resolution of the simulation, while simultaneously adding more points of calculation, thus increasing the required processing power and memory.

To achieve convergence, three factors can be checked which are PML thickness, spatial resolution and run-time. The method utilised for PML thickness and spatial resolution were to double the values until the results did not have significant changes. This was carried out in our simulations to ensure that the results converged.

For run-time, the issue is that the simulation must run for long enough that the transient fields have decayed sufficiently, due to processes such as PML absorption. This can be achieved by doubling the run-time until the results stop changing, however the MEEP external library that was used has a useful function called "*stop_when_fields_decayed*" that can check the fields in the simulation and stop it once the intensity of the transient fields fall below a certain value. This function was utilised in our code to ensure that the simulation ended only after the fields decayed below 10^{-6} of the original field intensity at the start of the simulation. In this case, t_{fin} in Figure 5.2 is replaced by the "*stop_when_fields_decayed*" function to determine the stop time of the simulation.

Another important aspect of the simulation is the boundary conditions, of which there are two main types;

a) **Surface Boundary Conditions.** These occur at the interface between two materials of different permittivities.

b) **Termination Boundary Conditions.** Only a finite volume of space can be simulated, therefore the simulation must always be spatially limited and terminated with certain boundary conditions.

For **surface boundary conditions**, the technique used in MEEP is the Surface Impedance Boundary Condition (SIBC) method [116]. The method takes a surface where 2 different materials meet and attempts to model it as an impedance. The surface with 2 materials (and 2 permittivities) is then removed and replaced with the impedance model. This works if the time-step of the simulation can be made small enough that the duration of an incident pulse and electromagnetic penetration depth into the material body is correspondingly small compared to the size of the material body. If this condition is met (time resolution is high enough), the incident wave can be considered to be travelling at the surface of the material. Some boundary layer approximations are then used to calculate the impedance of the surface and replace the original model [117]. This method is called the Surface Impedance Boundary Conditions (SIBC) method.

For the **termination boundary conditions**, MEEP supports 3 different types of terminations; Bloch-periodic, Perfect Matched Layers (PML), and Perfect Electric Conductors (PEC). Bloch-periodic boundaries are used for repetitive structures such as gratings or waveguides, where it is divided into small units and terminated with a Bloch-periodic boundary. This allows the user to simulate the entire structure with much lower computational resources. However, this method is not used in the dissertation.

PML boundaries were used in the simulation where the PML is an absorbing material placed at the boundaries with the special property of having zero reflections. The use of PML replicates what would happen to a transient field that radiated away into free

space and did not have any further interactions with the simulation. PML boundaries were used for all of the FDTD simulations.

The PEC boundary is simply a boundary of a perfect metal (zero absorption, zero skin depth, 100% electrical reflection, etc). This boundary was also utilized in the dissertation to replicate a perfect ground plane.

To summarize, the application of the FDTD method in MEEP requires defining certain initial conditions, parameters and boundaries, upon which the algorithm would divide the simulation into discrete Yee Lattice unit cells. The E and H fields for all points are then derived, and the FDTD flowchart is followed at progressions of half time-steps, $\Delta t/2$. When the simulation has run until the allotted time, or when the transient fields have all decayed, the simulation will stop. Finally, convergence of the results is obtained by doubling the resolution and PML thickness until the values do not have significant changes.

5.3 Simulation parameters and steps

The parameters used for gold (Aurum) were the modified Drude-Lorentz values as shown in Appendix B. These values were converted into the unit scale utilized in MEEP and implemented into the code. For the GaAs dielectric material, the experimental values as published in [93] were used. The complex permittivity used in tabular form is listed in Appendix C and a continuous plot of the values is presented under heading 2.2.3 in Chapter Two.

Next, the geometry of the design was defined, and was set as a dipole placed on a cavity design as described in Chapter 3. The dipole arm lengths were set to180 nm and the material set as gold, while the dielectric cavity size was 880nm x 880nm x 1000nm and

consists of GaAs. A sketch of the geometry is shown in Figure 5.3. A Gaussian source was used with a pulsed frequency centred at 150 THz with a frequency width of 3 THz per pulse.

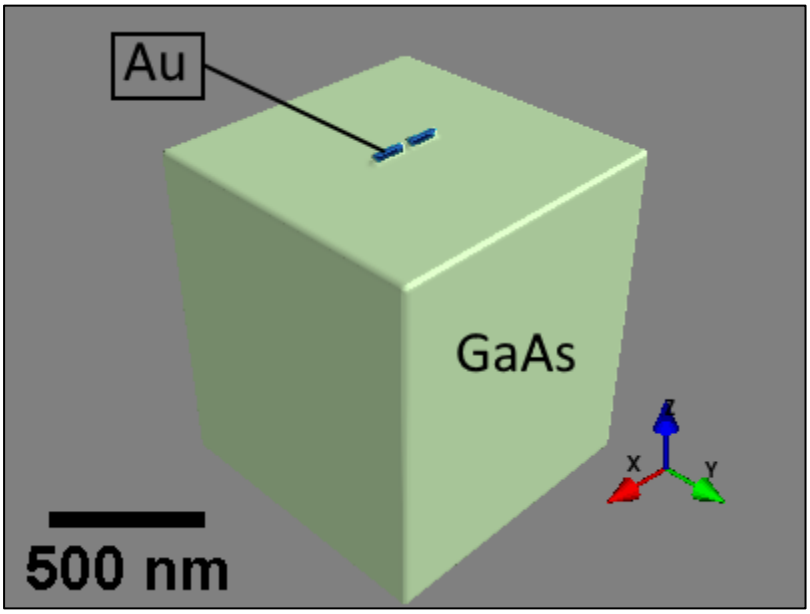

Figure 5.3: Graphical view of FDTD simulation geometry

The near-field intensity enhancement was obtained by placing a box in dipole centre gap and recording the electric field in the gap during simulations. The values were obtained from the dipole gap by recording the values from a 2nm x 2nm x 2nm cube in the centre of the gap, and the values were averaged across the volume measurement area. The data was recorded a distance away from the metal and dielectric surfaces to avoid complexities due to surface interactions. The simulations were run in batch form using unix (linux) batch processes for each iteration.

The results of the output were generated into hd5 files, which are database files used to store large quantities of data. This was crucial to store the large amount of electric and magnetic flux data for each point in the numerical simulation.

The simulations were repeated for a design where the cavity was halved to 880nm x 880nm x 500nm, and a PEC boundary was placed on the opposite side of the cavity to the dipole. This replicated the simulation as shown in Figure 4.5 (Chapter 4), where a ground plane was used to mirror the cavity and attempt to double the NFIE.

The results from the hd5 files were parsed and compiled. They were then normalized against the incident plane wave to calculate the enhancement that was obtained. This was also carried out using unix batch commands. The results for both designs were recorded and compared to the results obtained from commercial solvers.

5.4 Results from Numerical Simulation

From the FDTD code run in Python, the results in Figure 5.4 were obtained. The results of the numerical simulation utilizing FDTD has shown some variation from the results of HFSS and CST. However, the results are fairly identical in all three solvers, with the variation for FDTD mainly found as a frequency shift of around 10 THz. The results show a strong compatibility and are consistent between the three models. Where HFSS has a peak NFIE of ~33k and CST has a peak of ~37k, FDTD shows a peak of ~38k. The resonant frequency for HFSS is ~150 THz, while CST has it at ~145 THz, and FDTD has its resonance at ~155 THz. Overall, the differences are less than 10% and are attributed to the different modelling methods of each solver.

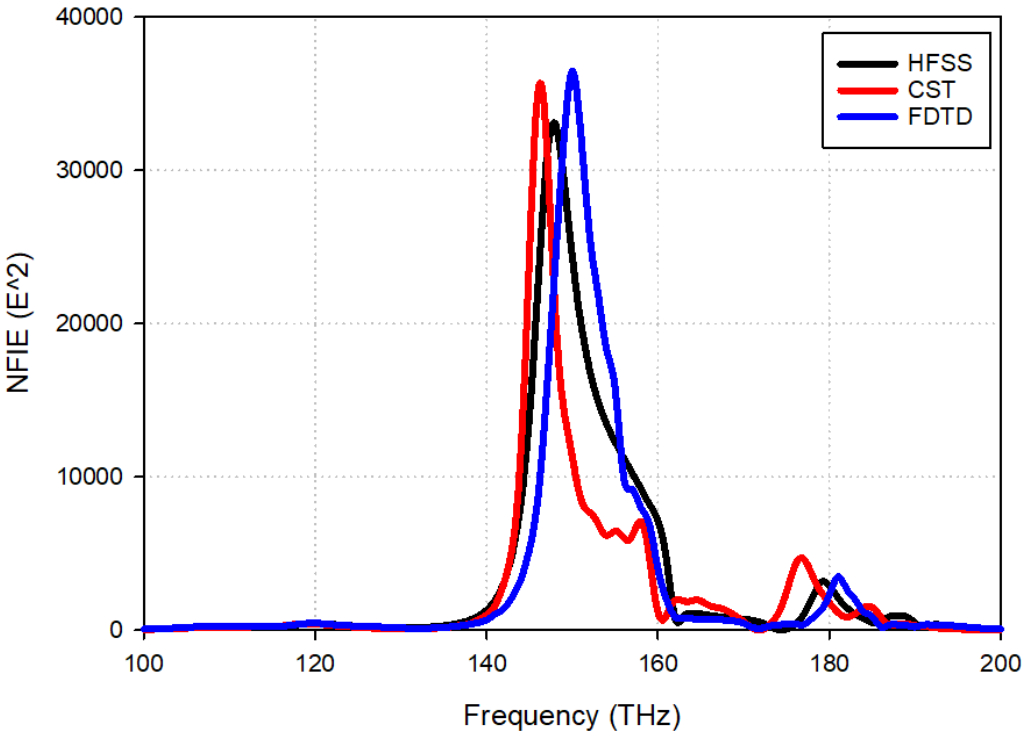

Figure 5.4: Results of various solvers for the NFIE for a 180nm long gold dipole on a 880x880x1000nm dielectric cavity

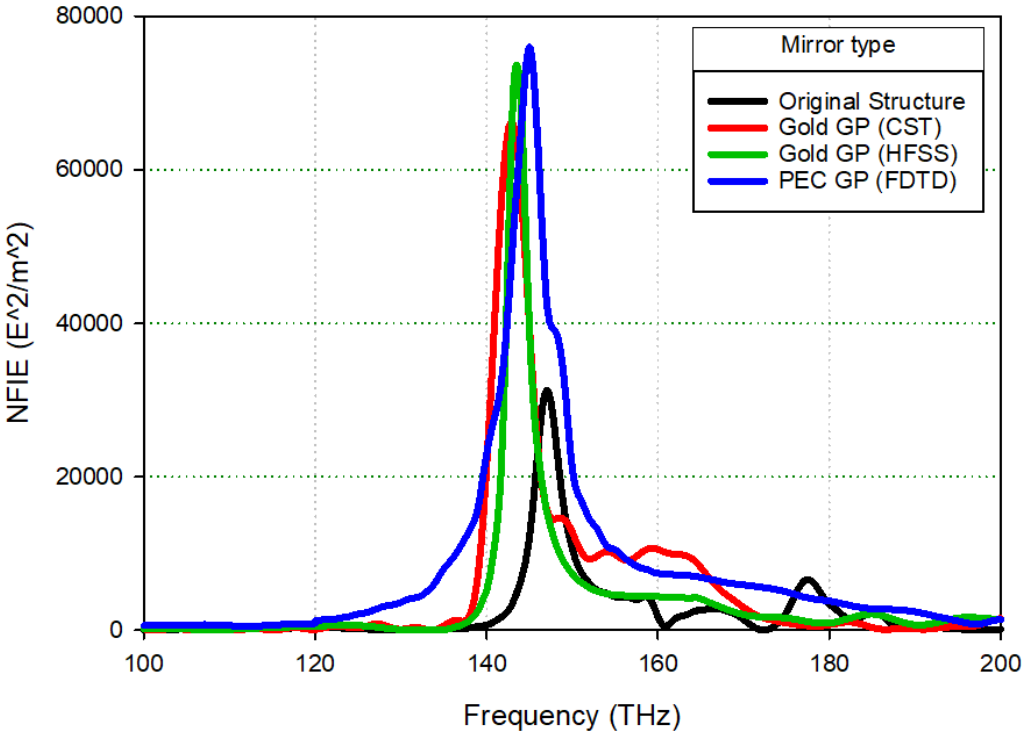

Figure 5.5: Results of various solvers for the NFIE for a 180nm long gold dipole on a 880x880x500nm dielectric cavity over a ground plane

The simulations were repeated for the same design placed on a ground plane, with the dielectric cavity halved in thickness to accommodate the mirroring effect of the ground plane. The results from FDTD in Figure 5.5 again show a strong agreement with the results from commercial solvers. The resonant frequencies have been slightly shifted, which is attributed to the mirroring effect of the dipole. HFSS has a resonance at ~145 THz, CST has its resonance at ~142 THz, and FDTD has a resonance at ~148 THz, which has a difference of less than 5%. In terms of amplitude, the use of the PEC ground plane in FDTD results in a higher NFIE of ~76k, whereas HFSS is slightly lower at ~73k and CST is ~68k. Overall, the results are positive with deviations of less than 10% to either frequency or amplitude.

5.5 Conclusion

In this chapter, the main focus was to establish whether the commercial solvers used in previous chapters gave accurate results. The accuracy of CST and HFSS should have been determined through experimentation, however, a lack of time and facilities prevented that option. The results were instead compared against numerical analysis.

Since the rise of computers, the numerical method Finite-Difference Time-Domain (FDTD) has been used as a numerical simulation method. The introduction of the Yee Lattice method has also increased its efficiency. The Yee Lattice FDTD method was therefore implemented utilizing the external dependencies MEEP and NumPy while coding it in Linux under Python 3.7. Material models of gold and GaAs were described and inserted into the code, and simulations were run using the same geometry as the designs in Chapter 3 and 4 for a gold dipole on a dielectric cavity, and a gold dipole on a dielectric cavity with a ground plane, respectively. Although there were other designs addressed in this dissertation, more complex geometries were difficult to implement in the FDTD code.

However, the results of the simulations have shown strong agreement between the FDTD results and the commercial solver results from CST and HFSS and is taken as support for the results of this dissertation.

Chapter 6: Conclusions and Future Work

6.1 Conclusions

This dissertation has presented a theoretical study on the responses of plasmonic nanoantennas in the visible and near-infrared (NIR) region. The nanoantennas operating at this frequency have been shown to have strong plasmonic gains by concentrating and localizing incident optical waves into subwavelength areas. This is achieved by exploiting the surface plasmon resonance that occurs in gold and some other metals in the optical frequency range, which allows for a transfer of energy to occur into an area that is much smaller than the wavelength of the incident plane wave. Other works in the literature have focused on improving NFIE through antenna designs, Fabry-Perot cavities, and photonic mirrors, however very little attention has been given to the substrate. This dissertation has investigated a dielectric resonant cavity that can be coupled to plasmonic nanoantennas and can be easily designed and modelled while simultaneously identifying a ballpark figure for the expected NFIE after coupling.

The dissertation first ensured that the results were valid through a multi-step procedure. The material models for the various materials that would be used in this work were compared and the Brendel-Bormann model was chosen over the more commonly used Drude model due to higher accuracy. The BB model was also fitted to experimental data to ensure that the results would be reliable. The commercial electromagnetic solvers of CST and HFSS were used to generate data based on designs from the literature, and the solvers and material models were proven to be consistent with literature when the generated results had only small discrepancies. A dielectric resonator was then proposed, with clear results

in the form of strong NFIE when coupled with a gold plasmonic dipole. It was shown that the strong NFIE was formed due to coupling with the resonant modes of the dielectric cavity resonator. The resonator was analysed using equations that model a truncated dielectric waveguide and numerical analysis was shown to accurately predict the frequency and characteristic of the modes. Unfortunately, the equations do not predict the electric field strength of the modes and therefore CST was used to simulate the amplitude of the resonant modes. All the resonant modes were shown to be capable of coupling with the nanoantenna and therefore it was only a matter of choosing and coupling with the resonant mode with the strongest electric field enhancement. Finally, the results obtained in CST and HFSS were corroborated with numerical analysis in the form of FDTD calculations which were automated in computer code. **The first contribution** of this dissertation is that it details how any resonant mode of a dielectric cavity can be coupled to a plasmonic nanoantenna, as well as how to find such resonant modes, obtain their enhancement, and guesstimate the resultant NFIE increase. Included in the first contribution is an NFIE of 37k that is significantly higher than published NFIEs using a gold dipole with a 10nm gap.

The NFIE increase of a gold dipole was shown to be exponentially proportional to the strength of the incident light and is **the second contribution** of this dissertation. The dielectric resonator cavity model was found to trap and focus the incident light, and therefore follows the same linear model albeit with some losses when the gallium arsenide (GaAs) data driven model was applied. This is important as it allows rapid simulation of ideal dielectric cavity models that are suitable for coupling to plasmonic nano-antennas. Simulations of dielectric cavities that have strong field enhancement not due to plasmonic effects are conclusively shown to keep this enhancement when coupled to plasmonic nano-antennas, which allows for rapid prototyping since dielectric cavities can be simulated or experimentally tested much more easily than plasmonic nano-antennas.

Other forms of plasmonic enhancement were also investigated. Other light-focusing and light-coupling models were investigated, and the results discussed. However, these other designs were also combined with a dielectric resonator cavity to understand whether the dielectric resonator could couple universally to other structures. **The third contribution** of this work is to show that the proposed resonator can easily couple with a multitude of structures including metallic ground planes, photonic crystals and optical lenses, and can target a resonant frequency through simple scaling methods. However, coupling with multiple structures causes frequency shifts and introduces other considerations such as added thickness or more complicated fabrication methods.

The fourth contribution is the demonstration of a low-profile method to achieve similar or better results than that already shown in the first contribution. A low-profile design was proposed in combination with a thin gold slab for a total thickness of 270nm which achieved a NFIE of 62k, higher than the original design with a thickness of 1000nm which had a NFIE of 37k.

The properties of the proposed hybrid dipole-cavity were also studied using numerical analysis. A program using the FDTD method was coded in Python to understand the behaviour of the design with certain assumptions without the influence of commercial solvers. **The fifth contribution** of this work is to create the code to analyse this design with the FDTD method, to verify the results obtained in the earlier chapters. All the simulation results have also been compared at various points against numerical analysis, other electromagnetic solvers, as well as published results. Although fabrication and experiments were not carried out due to a lack of facilities and the high cost of fabrication, a large number of journal papers in this field have also opted to publish simulated results. The

cross-comparisons carried out at various steps should ensure that the results are close to real results.

6.2 Recommendations for Future Work

There are many avenues for future work in this line of research. **The first** is to overcome the limitations in this current research in terms of no experimental data. The ability to fabricate the proposed designs and experimentally test them will improve the validity of the results by adding another supporting point on top of numerical analysis and simulations. This additional data would verify the results since challenges can occur in terms of fabrication defects that can easily affect the predicted results, and experimentation can easily verify the extent of these changes. One of the challenges of fabrication using current technologies is that all fabrication methods would have topographical defects to a certain extent due to the resolutions available. For example, the designs proposed in this dissertation are 20nm thick with a 10nm gap, and very few fabrication technologies can even have 5nm resolution. Even 5nm resolution fabrication methods would therefore still have defects, for example a 2nm difference in the length or width of the gold nanorods is equivalent to 10% difference of the design thickness and 20% difference of the gap size which would drastically affect the expected results. It might therefore require multiple tries to obtain a sample where the defects are not large enough to suppress or skew the high potential results. Microstructural fabrication defects such as surface roughness and nano-cracks might also be enough to significantly change the NFIE and are still prevalent in most fabrication technologies where the resolution is around ~10nm as described in Chapter 1. The width and height of the fabricated structures may also vary with changes of +/- 5nm and the line edges are also susceptible to roughness whereby the lines are not perfectly straight. Lastly, shot noise can also occur whereby the surfaces of the fabricated structures may be affected

Second, many more dielectric resonator designs are possible and can be achieved with various dielectric materials. Changes in the aspect ratio and in the permittivity of the dielectric resonator will excite new and different modes at different frequencies, and even the amplitude of the resonance peaks would be affected. Therefore, each new design offers an opportunity to target different applications that might require different needs such as high NFIE, or larger bandwidth, or thinner profile. So far only two designs have been proposed in this dissertation that target high NFIE and low-profile design. Other applications could be considered at other frequencies and different relative permittivity. The new dielectric resonator cavity designs can be easily generated through the MATLAB code that we have created and can be quickly compared against simulations in CST or HFSS. Once a suitable resonance mode is identified, the dielectric cavity can be scaled in terms of size and frequency to couple with a plasmonic nano-antenna. The work in Chapter 2 shows that it is possible to scale designs of dielectric cavities from the GHz range to the THz range in a predictable manner. More dielectric resonator designs should therefore be attempted with a target to different application scenarios. Some designs were previously attempted in the first year of the PhD studies but at the time were not completely explored due to their more complicated natures, which include cylindrical dielectric cavity designs, hemispherical dielectric cavities, as well as curved plasmonic nano-antennas placed on dielectric cavity curved surfaces.

Third, further experiments could be run with the use of different materials such as coated silver instead of gold for a plasmonic material. Gold is more commonly used and was thus used in this study to enable easier comparisons with the literature. Silver on the other hand, oxidates, but more advanced fabrication methods now allow for a coating to be applied on the silver surface which can improve results further while reducing the effect of oxidation. Iterating the designs in this dissertation with coated silver could prove beneficial

in terms of securing a structure with extremely strong NFIE. Although the coating would reduce the side effects that come with oxidation, the effects of the coating and the plasmon resonance of silver itself would introduce issues and changes that would need to be addressed in future works to ensure that the coupling is optimized. One of those issues is quenching, which would reduce the fluorescence and the decay rate of the plasmonic structure depending on the material and thickness of the coating. Therefore, the use of coated silver is expected to enhance certain properties such as NFIE, while reducing other properties such as fluorescence and Q-values. Therefore, it requires further research to understand the best applications of dielectric cavities coupled to coated silver nano-antennas. Other plasmonic metals also introduce their own sets of advantages and disadvantages, such as aluminium which has a plasmonic resonance closer to the ultraviolet (UV) wavelength and could be more beneficial for higher frequency applications. This could become a more heated topic in the future as higher frequencies such as UV and X-ray are further exploited in terms of plasmonic resonance. However, the dielectric resonator cavity designs would need to be tweaked and optimized to perform well with such new materials. It is at this juncture that the methods used in this dissertation become useful in terms of quickly evaluating potential dielectric cavity designs to be coupled with such plasmonic nano-antennas. The use of other dielectric materials would also contribute knowledge due to the different optical properties of each material as well as ease of fabrication. The ideal dielectric material would have a high relative permittivity to allow a high refractive index, but with low absorption to reduce optical and thermal losses as described in Chapter 2. The application of such a material could perhaps further increase the NFIE of the hybrid structure comprised of a dielectric cavity and plasmonic nano-antenna, while reducing the footprint of such a design.

Fourth, further investigations can be carried out for designs with a gap of less than 10nm, with particular emphasis on designs that have gaps less than 2nm which have been a challenge in the course of this work where gaps less than 2nm have reduced the NFIE. Designs with a gap smaller than 10nm have been proven by other works to have stronger plasmonic resonance, but this is countered by the feasibility and practicality of utilizing such designs for mass production. Consequently, the number of publications which have carried out experimental studies on such small gap sizes are still relatively small. In terms of gaps with less than 2nm, it was found in our simulations that gaps less than this size would actually reduce the NFIE found in the gap which was not intuitively expected. This can be attributed to the ratio between the gap size and the thickness of the dipole, where if the ratio is too large, then the gap "disappears" and the dipole reacts as a single piece which shifts the absorbed incident light from the centre of the gap to the far ends of the dipole arms. Although the dipole could be made thinner to maintain the ratio, this would have negative effects on the absorption of the incident light which is affected by the thickness of the dipole.

Fifth, the proposed designs have possible applications in such fields as solar power generation and optical communication, however, each field has its own parameters and standards that must be taken into account. For example, fibre optic communication utilizes specific wavelengths based on certain standards for signal transmission and would require a transmitter or receiver operating at that specific wavelength. The designs proposed in this dissertation would necessarily be adjusted to such requirements. Other industries may require the use of a particular dielectric material for the cavity or have restrictions in terms of the size of the total structure in order to fit it into their current designs. The proposed designs in this work are general in nature but can be tailored in future research to suit particular applications while taking into account the parameters and limitations set forth by

each industry. In that sense, the mirrored dielectric cavity and the low-profile dielectric cavities that were proposed give a hint towards dielectric cavities constrained by certain physical dimensions.

Bibliography

[1] C. A. Balanis, *Antenna theory: analysis and design*, Fourth edition. Hoboken, NJ: Wiley, 2016.

[2] P. R. Gringer, *English: Revised diagram with re-aligned spectrum*. 2013.

[3] H. Vettikalladi, W. T. Sethi, A. F. B. Abas, W. Ko, M. A. Alkanhal, and M. Himdi, "Sub-THz Antenna for High-Speed Wireless Communication Systems," *International Journal of Antennas and Propagation*, 2019. [Online]. Available: https://www.hindawi.com/journals/ijap/2019/9573647/. [Accessed: 12-Mar-2020].

[4] A. J. Tudos and R. Schasfoort, Eds., *Handbook of Surface Plasmon Resonance*. 2008.

[5] A. Otto, "Excitation of nonradiative surface plasma waves in silver by the method of frustrated total reflection," *Z. Für Phys. Hadrons Nucl.*, vol. 216, no. 4, pp. 398–410, Aug. 1968, doi: 10.1007/BF01391532.

[6] E. Kretschmann and H. Raether, "Notizen: Radiative Decay of Non Radiative Surface Plasmons Excited by Light," *Z. Für Naturforschung A*, vol. 23, no. 12, Jan. 1968, doi: 10.1515/zna-1968-1247.

[7] S. A. Maier, *Plasmonics: fundamentals and applications*. New York: Springer, 2007.

[8] W. Hergert and T. Wriedt, *The Mie Theory: Basics and Applications*. Berlin; London: Springer, 2012.

[9] "Beyond the diffraction limit," *Nat. Photonics*, vol. 3, no. 7, p. 361, Jul. 2009, doi: 10.1038/nphoton.2009.100.

[10] T. K. Sarkar, M. N. Abdallah, M. Salazar-Palma, and W. M. Dyab, "Surface Plasmons-Polaritons, Surface Waves, and Zenneck Waves: Clarification of the terms and a description of the concepts and their evolution.," *IEEE Antennas Propag. Mag.*, vol. 59, no. 3, pp. 77–93, Jun. 2017, doi: 10.1109/MAP.2017.2686079.

[11] S. V. Boriskina *et al.*, "Losses in plasmonics: from mitigating energy dissipation to embracing loss-enabled functionalities," *Adv. Opt. Photonics*, vol. 9, no. 4, p. 775, Dec. 2017, doi: 10.1364/AOP.9.000775.

[12] K. B. Crozier, W. Zhu, D. Wang, S. Lin, M. D. Best, and J. P. Camden, "Plasmonics for Surface Enhanced Raman Scattering: Nanoantennas for Single Molecules," *IEEE J. Sel. Top. Quantum Electron.*, vol. 20, no. 3, pp. 1–11, May 2014, doi: 10.1109/JSTQE.2013.2282257.

[13] S. Okazaki, "High resolution optical lithography or high throughput electron beam lithography: The technical struggle from the micro to the nano-fabrication evolution," *Microelectron. Eng.*, vol. 133, pp. 23–35, Feb. 2015, doi: 10.1016/j.mee.2014.11.015.

[14] R. Elghanian, J. J. Storhoff, R. C. Mucic, R. L. Letsinger, and C. A. Mirkin, “Selective Colorimetric Detection of Polynucleotides Based on the Distance-Dependent Optical Properties of Gold Nanoparticles,” *Science*, vol. 277, no. 5329, pp. 1078–1081, Aug. 1997, doi: 10.1126/science.277.5329.1078.

[15] X. Chen, Y. Yang, Y.-H. Chen, M. Qiu, R. J. Blaikie, and B. Ding, “Probing Plasmonic Gap Resonances between Gold Nanorods and a Metallic Surface,” *J. Phys. Chem. C*, vol. 119, no. 32, pp. 18627–18634, Aug. 2015, doi: 10.1021/acs.jpcc.5b06006.

[16] A. V. Ermushev, B. V. Mchedlishvili, V. A. Oleĭnikov, and A. V. Petukhov, “Surface enhancement of local optical fields and the lightning-rod effect,” *Quantum Electron.*, vol. 23, no. 5, p. 435, 1993, doi: 10.1070/QE1993v023n05ABEH003090.

[17] W. Yu-Ming, “Analysis and Design of Nanoantennas,” PhD Dissertation, National University of Singapore, 2010.

[18] A. K. Sharma and A. Dominic, “Influence of Chemical Potential on Graphene-Based SPR Sensor #x2019;s Performance,” *IEEE Photonics Technol. Lett.*, vol. 30, no. 1, pp. 95–98, Jan. 2018, doi: 10.1109/LPT.2017.2776945.

[19] H. Yu, X. Shan, S. Wang, and N. Tao, “Achieving High Spatial Resolution Surface Plasmon Resonance Microscopy with Image Reconstruction,” *Anal. Chem.*, vol. 89, no. 5, pp. 2704–2707, Mar. 2017, doi: 10.1021/acs.analchem.6b05049.

[20] A. Kinkhabwala, Z. Yu, S. Fan, Y. Avlasevich, K. Müllen, and W. E. Moerner, “Large single-molecule fluorescence enhancements produced by a bowtie nanoantenna,” *Nat. Photonics*, vol. 3, no. 11, pp. 654–657, Nov. 2009, doi: 10.1038/nphoton.2009.187.

[21] “Raman FAQs - What is the spatial resolution of a Raman microscope? - HORIBA.” [Online]. Available: http://www.horiba.com/scientific/products/raman-spectroscopy/raman-academy/raman-faqs/what-is-the-spatial-resolution-of-a-raman-microscope/. [Accessed: 16-Apr-2018].

[22] L. A. Coldren, S. W. Corzine, and M. Mashanovitch, *Diode lasers and photonic integrated circuits*, 2nd ed. Hoboken, N.J: Wiley, 2012.

[23] I. Ros *et al.*, “SERS Properties of Gold Nanorods at Resonance with Molecular, Transverse, and Longitudinal Plasmon Excitations,” *Plasmon. Norwell Mass*, vol. 9, no. 3, pp. 581–593, 2014, doi: 10.1007/s11468-014-9669-4.

[24] S. Varlamov, Z. Ouyang, X. Zhao, and D. S. Jung, “Surface plasmon enhanced light-trapping in polycrystalline silicon thin-film solar,” in *Photonics Global Conference (PGC), 2010*, 2010, pp. 1–6, doi: 10.1109/PGC.2010.5706090.

[25] M. S. Eggleston, K. Messer, L. Zhang, E. Yablonovitch, and M. C. Wu, “Optical antenna enhanced spontaneous emission,” *Proc. Natl. Acad. Sci.*, vol. 112, no. 6, pp. 1704–1709, Feb. 2015, doi: 10.1073/pnas.1423294112.

[26] J. M. Jornet and I. F. Akyildiz, “Graphene-based Plasmonic Nano-Antenna for Terahertz Band Communication in Nanonetworks,” *IEEE J. Sel. Areas Commun.*, vol. 31, no. 12, pp. 685–694, Dec. 2013, doi: 10.1109/JSAC.2013.SUP2.1213001.

[27] X. Wen, A. Datta, L. M. Traverso, L. Pan, X. Xu, and E. E. Moon, “High throughput optical lithography by scanning a massive array of bowtie aperture antennas at near-field,” *Sci. Rep.*, vol. 5, p. 16192, Nov. 2015, doi: 10.1038/srep16192.

[28] R. Wollhofen, J. Katzmann, C. Hrelescu, J. Jacak, and T. A. Klar, “120 nm resolution and 55 nm structure size in STED-lithography,” *Opt. Express*, vol. 21, no. 9, p. 10831, May 2013, doi: 10.1364/OE.21.010831.

[29] B. Kwon and J. H. Kim, “Importance of Molds for Nanoimprint Lithography: Hard, Soft, and Hybrid Molds,” *J. Nanosci.*, vol. 2016, pp. 1–12, 2016, doi: 10.1155/2016/6571297.

[30] R. Garcia, A. W. Knoll, and E. Riedo, “Advanced scanning probe lithography,” *Nat. Nanotechnol.*, vol. 9, no. 8, pp. 577–587, Aug. 2014, doi: 10.1038/nnano.2014.157.

[31] X. Shi, P. Prewett, E. Huq, D. M. Bagnall, A. P. G. Robinson, and S. A. Boden, “Helium ion beam lithography on fullerene molecular resists for sub-10nm patterning,” *Microelectron. Eng.*, vol. 155, pp. 74–78, Apr. 2016, doi: 10.1016/j.mee.2016.02.045.

[32] A. Cattoni *et al.*, “Sub-10nm electron and helium ion beam lithography using a recently developed alumina resist,” *Microelectron. Eng.*, vol. 193, pp. 18–22, Jun. 2018, doi: 10.1016/j.mee.2018.02.015.

[33] L. Huang, L. Xu, H. Zhang, and N. Gu, “Fabrication of a nano-scale gap by selective chemical deposition,” *Chem. Commun.*, no. 1, pp. 72–73, Jan. 2002, doi: 10.1039/B109189C.

[34] M. J. Banholzer, L. Qin, J. E. Millstone, K. D. Osberg, and C. A. Mirkin, “On-wire lithography: synthesis, encoding and biological applications,” *Nat. Protoc.*, vol. 4, no. 6, pp. 838–848, 2009, doi: 10.1038/nprot.2009.52.

[35] T. Hutter, S. R. Elliott, and S. Mahajan, “Interaction of metallic nanoparticles with dielectric substrates: effect of optical constants,” *Nanotechnology*, vol. 24, no. 3, pp. 1–8, Jan. 2013, doi: 10.1088/0957-4484/24/3/035201.

[36] M. Khosravi, R. A. Sadeghzadeh, and M. S. Abrishamian, “Resonant Capability of Multilayer Spheroidal Nanoparticles as Plasmonic Nanoantennas,” *Sess. 3A8*, p. 521, Mar. 2013.

[37] C. Fumeaux, M. A. Gritz, I. Codreanu, W. L. Schaich, F. J. González, and G. D. Boreman, “Measurement of the resonant lengths of infrared dipole antennas,” *Infrared Phys. Technol.*, vol. 41, no. 5, pp. 271–281, Oct. 2000, doi: 10.1016/S1350-4495(00)00047-5.

[38] H. Liu, J. Ng, S. B. Wang, Z. H. Hang, C. T. Chan, and S. N. Zhu, “Strong plasmon coupling between two gold nanospheres on a gold slab,” *New J. Phys.*, vol. 13, no. 7, p. 073040, Jul. 2011, doi: 10.1088/1367-2630/13/7/073040.

[39] S. V. Lobanov, T. Weiss, D. Dregely, H. Giessen, N. A. Gippius, and S. G. Tikhodeev, “Emission properties of an oscillating point dipole from a gold Yagi-Uda nanoantenna array,” *ArXiv11100301 Phys.*, Oct. 2011.

[40] Y. Wu, L.-W. Li, and B. Liu, “Gold Bow-Tie Shaped Aperture Nanoantenna: Wide Band Near-field Resonance and Far-Field Radiation,” *IEEE Trans. Magn.*, vol. 46, no. 6, pp. 1918–1921, Jun. 2010, doi: 10.1109/TMAG.2010.2043063.

[41] Y. Wu, L.-W. Li, and B. Liu, “Geometric effects in designing bow-tie nanoantenna for optical resonance investigation,” in *2010 Asia-Pacific Symposium on Electromagnetic Compatibility (APEMC)*, 2010, pp. 1108–1111, doi: 10.1109/APEMC.2010.5475666.

[42] V. Dinesh Kumar, A. Bhardwaj, and D. Mishra, “Investigation of a turnstile nanoantenna,” *IET Micro Nano Lett.*, vol. 6, no. 2, pp. 94–97, Feb. 2011, doi: 10.1049/mnl.2010.0168.

[43] A. Polemi and K. L. Shuford, “Fabry–Perot effect on dimer nanoantennas,” *Photonics Nanostructures-Fundam. Appl.*, vol. 10, no. 1, pp. 36–45, 2012.

[44] J. Chen *et al.*, “Optical Cavity-Enhanced Localized Surface Plasmon Resonance for High-Quality Sensing,” *IEEE Photonics Technol. Lett.*, vol. 30, no. 8, pp. 728–731, Apr. 2018, doi: 10.1109/LPT.2018.2814216.

[45] S. Alrasheed and E. D. Fabrizio, “Effect of Surface Plasmon Coupling to Optical Cavity Modes on the Field Enhancement and Spectral Response of Dimer-Based sensors,” *Sci. Rep.*, vol. 7, no. 1, p. 10524, Sep. 2017, doi: 10.1038/s41598-017-11140-0.

[46] R. Y. Chou *et al.*, “A hybrid nanoantenna for highly enhanced directional spontaneous emission,” *J. Appl. Phys.*, vol. 115, no. 24, p. 244310, Jun. 2014, doi: 10.1063/1.4885422.

[47] D. Dey, J. Kohoutek, R. M. Gelfand, A. Bonakdar, and H. Mohseni, “Composite Nano-Antenna Integrated With Quantum Cascade Laser,” *IEEE Photonics Technol. Lett.*, vol. 22, no. 21, pp. 1580–1582, Nov. 2010, doi: 10.1109/LPT.2010.2073459.

[48] Y. Zhou, D. Zhu, X. Yu, W. Ding, and F. Luan, “Fano resonances in metallic grating coupled whispering gallery mode resonator,” *Appl. Phys. Lett.*, vol. 103, no. 15, p. 151108, Oct. 2013, doi: 10.1063/1.4823531.

[49] Y. Chu, E. Schonbrun, T. Yang, and K. B. Crozier, “Experimental observation of narrow surface plasmon resonances in gold nanoparticle arrays,” *Appl. Phys. Lett.*, vol. 93, no. 18, p. 181108, 2008, doi: 10.1063/1.3012365.

[50] F. Wang and H. Harutyunyan, “Tailoring the quality factors and nonlinear response in hybrid plasmonic-dielectric metasurfaces,” *Opt. Express*, vol. 26, no. 1, pp. 120–129, Jan. 2018, doi: 10.1364/OE.26.000120.

[51] K. Li, M. I. Stockman, and D. J. Bergman, “Self-Similar Chain of Metal Nanospheres as an Efficient Nanolens,” *Phys. Rev. Lett.*, vol. 91, no. 22, Nov. 2003, doi: 10.1103/PhysRevLett.91.227402.

[52] O. Sqalli, I. Utke, P. Hoffmann, and F. Marquis-Weible, “Gold elliptical nanoantennas as probes for near field optical microscopy,” *J. Appl. Phys.*, vol. 92, no. 2, pp. 1078–1083, Jul. 2002, doi: 10.1063/1.1487918.

[53] A. Polemi and K. L. Shuford, “Effect of a dielectric coating on quenching in a molecule-nanosphere system,” *Chem. Phys. Lett.*, vol. 546, pp. 129–132, Sep. 2012, doi: 10.1016/j.cplett.2012.07.074.

[54] K. M. Luk, Ed., *Dielectric resonator antennas*. Baldock: Research Studies Press, 2003.

[55] E. a. J. Marcatili, “Dielectric Rectangular Waveguide and Directional Coupler for Integrated Optics,” *Bell Syst. Tech. J.*, vol. 48, no. 7, pp. 2071–2102, 1969, doi: 10.1002/j.1538-7305.1969.tb01166.x.

[56] L. Zou *et al.*, “Efficiency and Scalability of Dielectric Resonator Antennas at Optical Frequencies,” *IEEE Photonics J.*, vol. 6, no. 4, pp. 1–10, Aug. 2014, doi: 10.1109/JPHOT.2014.2337891.

[57] L. Lin *et al.*, “Dielectric nanoresonator based lossless optical perfect magnetic mirror with near-zero reflection phase,” *Appl. Phys. Lett.*, vol. 108, no. 17, p. 171902, Apr. 2016, doi: 10.1063/1.4947274.

[58] X.-W. Chen, M. Agio, and V. Sandoghdar, “Metallodielectric hybrid antennas for ultrastrong enhancement of spontaneous emission,” *Phys. Rev. Lett.*, vol. 108, no. 23, p. 233001, 2012.

[59] R. H. Ritchie, “Plasma Losses by Fast Electrons in Thin Films,” *Phys. Rev.*, vol. 106, no. 5, pp. 874–881, Jun. 1957, doi: 10.1103/PhysRev.106.874.

[60] “Bragg reflector.” [Online]. Available: http://www.batop.com/information/r_Bragg.html. [Accessed: 17-Apr-2018].

[61] M. Kaliteevski *et al.*, “Tamm plasmon-polaritons: Possible electromagnetic states at the interface of a metal and a dielectric Bragg mirror,” *Phys. Rev. B*, vol. 76, no. 16, p. 165415, Oct. 2007, doi: 10.1103/PhysRevB.76.165415.

[62] V. Lousse, W. Suh, O. Kilic, S. Kim, O. Solgaard, and S. Fan, “Angular and polarization properties of a photonic crystal slab mirror,” *Opt. Express*, vol. 12, no. 8, pp. 1575–1582, Apr. 2004, doi: 10.1364/OPEX.12.001575.

[63] B. Sain, R. Kaner, Y. Bondy, and Y. Prior, “Plasmonic flat surface Fabry-Perot interferometry,” *Nanophotonics*, vol. 7, no. 3, pp. 635–641, 2018, doi: 10.1515/nanoph-2017-0082.

[64] Z. Liu, E. Li, V. M. Shalaev, and A. V. Kildishev, “Near field enhancement in silver nanoantenna-superlens systems,” *Appl. Phys. Lett.*, vol. 101, no. 2, p. 021109, 2012.

[65] S. Maity and B. Gupta, “Closed Form Expressions to Find Radiation Patterns of Rectangular Dielectric Resonator Antennas for Various Modes,” *IEEE Trans. Antennas Propag.*, vol. 62, no. 12, pp. 6524–6527, Dec. 2014, doi: 10.1109/TAP.2014.2361146.

[66] V. Mocella and S. Romano, “Giant field enhancement in photonic resonant lattices,” *Phys. Rev. B*, vol. 92, no. 15, p. 155117, Oct. 2015, doi: 10.1103/PhysRevB.92.155117.

[67] T. Iida, A. Nakamura, S. Hidaka, M. Tamura, T. Shiono, and S. Furumiya, “Enhanced modulation of scattered light from phase-change nanoparticles by tailored plasmonic mirror image,” *Appl. Phys. Lett.*, vol. 103, no. 4, p. 041108, Jul. 2013, doi: 10.1063/1.4813749.

[68] A. M. A. Sabaawi, C. C. Tsimenidis, and B. S. Sharif, “Planar Bowtie Nanoarray for THz Energy Detection,” *IEEE Trans. Terahertz Sci. Technol.*, vol. 3, no. 5, pp. 524–531, Sep. 2013, doi: 10.1109/TTHZ.2013.2271833.

[69] B. B. Yousif and A. S. Samra, “Modeling of Optical Nanoantennas,” *Phys. Res. Int.*, vol. 2012, p. e321075, Nov. 2012, doi: 10.1155/2012/321075.

[70] “Solvers | CST EMC STUDIO.” [Online]. Available: https://www.cst.com/products/cstemcs/solvers. [Accessed: 30-Aug-2018].

[71] C. Hafner and L. H. Bomholt, *The 3D electrodynamic wave simulator: 3D MMP software and user’s guide*. Wiley, 1993.

[72] J. Hoffmann, C. Hafner, P. Leidenberger, J. Hesselbarth, and S. Burger, “Comparison of electromagnetic field solvers for the 3D analysis of plasmonic nanoantennas,” in *SPIE Europe Optical Metrology*, 2009, pp. 73900J–73900J.

[73] H. Yu, Y. Peng, Y. Yang, and Z.-Y. Li, “Plasmon-enhanced light–matter interactions and applications,” *Npj Comput. Mater.*, vol. 5, no. 1, pp. 1–14, Apr. 2019, doi: 10.1038/s41524-019-0184-1.

[74] M. Janipour, I. B. Misirlioglu, and K. Sendur, “Tunable Surface Plasmon and Phonon Polariton Interactions for Moderately Doped Semiconductor Surfaces,” *Sci. Rep.*, vol. 6, no. 1, pp. 1–11, Oct. 2016, doi: 10.1038/srep34071.

[75] W. M. Moore and P. J. Codella, “Oxidation of silver films by atomic oxygen,” *J. Phys. Chem.*, vol. 92, no. 15, pp. 4421–4426, Jul. 1988, doi: 10.1021/j100326a035.

[76] A. Kuzma *et al.*, “Influence of surface oxidation on plasmon resonance in monolayer of gold and silver nanoparticles,” *J. Appl. Phys.*, vol. 112, no. 10, p. 103531, Nov. 2012, doi: 10.1063/1.4767688.

[77] E. K. Payne, K. L. Shuford, S. Park, G. C. Schatz, and C. A. Mirkin, “Multipole Plasmon Resonances in Gold Nanorods,” *J. Phys. Chem. B*, vol. 110, no. 5, pp. 2150–2154, Feb. 2006, doi: 10.1021/jp056606x.

[78] K. Kolwas and A. Derkachova, “Plasmonic abilities of gold and silver spherical nanoantennas in terms of size dependent multipolar resonance frequencies and plasmon damping rates,” *Opto-Electron. Rev.*, vol. 18, no. 4, Jan. 2010, doi: 10.2478/s11772-010-0043-6.

[79] A. D. Rakić, A. B. Djurišić, J. M. Elazar, and M. L. Majewski, “Optical properties of metallic films for vertical-cavity optoelectronic devices,” *Appl. Opt.*, vol. 37, no. 22, pp. 5271–5283, Aug. 1998, doi: 10.1364/AO.37.005271.

[80] P. Jahanshahi, M. Ghomeishi, and F. R. M. Adikan, “Study on Dielectric Function Models for Surface Plasmon Resonance Structure,” *Sci. World J.*, vol. 2014, Jan. 2014, doi: 10.1155/2014/503749.

[81] P. B. Johnson and R. W. Christy, “Optical Constants of the Noble Metals,” *Phys. Rev. B*, vol. 6, no. 12, pp. 4370–4379, Dec. 1972, doi: 10.1103/PhysRevB.6.4370.

[82] E. D. Palik and G. Ghosh, *Handbook of optical constants of solids*. San Diego: Academic Press, 1998.

[83] P. Mühlschlegel, H.-J. Eisler, O. J. F. Martin, B. Hecht, and D. W. Pohl, “Resonant Optical Antennas,” *Science*, vol. 308, no. 5728, pp. 1607–1609, Jun. 2005, doi: 10.1126/science.1111886.

[84] T. T. Zygiridis and T. D. Tsiboukis, “Development of higher order FDTD schemes with controllable dispersion error,” *IEEE Trans. Antennas Propag.*, vol. 53, no. 9, pp. 2952–2960, Sep. 2005, doi: 10.1109/TAP.2005.854559.

[85] N. Kumar, “Spontaneous emission rate enhancement using optical antennas,” University of California, Berkeley, 2013.

[86] I. Kocakarin and K. Yegin, “Glass Superstrate Nanoantennas for Infrared Energy Harvesting Applications,” *Int. J. Antennas Propag.*, vol. 2013, p. e245960, Mar. 2013, doi: 10.1155/2013/245960.

[87] O. Madelung, *Semiconductors: Data Handbook*, 3rd ed. Berlin Heidelberg: Springer-Verlag, 2004.

[88] C. C. Homes, T. Vogt, S. M. Shapiro, S. Wakimoto, and A. P. Ramirez, “Optical Response of High-Dielectric-Constant Perovskite-Related Oxide,” *Science*, vol. 293, no. 5530, pp. 673–676, Jul. 2001, doi: 10.1126/science.1061655.

[89] D. G. Baranov *et al.*, “All-dielectric nanophotonics: the quest for better materials and fabrication techniques,” *Optica*, vol. 4, no. 7, pp. 814–825, Jul. 2017, doi: 10.1364/OPTICA.4.000814.

[90] “Scientists announce the quest for high-index materials,” 24-Jul-2017. [Online]. Available: https://phys.org/news/2017-07-scientists-quest-high-index-materials.html. [Accessed: 13-Jul-2018].

[91] J. Toudert and R. Serna, “Interband transitions in semi-metals, semiconductors, and topological insulators: a new driving force for plasmonics and nanophotonics [Invited],” *Opt. Mater. Express*, vol. 7, no. 7, pp. 2299–2325, Jul. 2017, doi: 10.1364/OME.7.002299.

[92] F. Li, Q. H. Liu, and D. P. Klemer, “Plasmon Resonance Effects in GaAs/AlGaAs Heterojunction Devices: An Analysis Based on Spectral Element Simulation,” *IEEE Trans. Electron Devices*, vol. 61, no. 5, pp. 1477–1482, May 2014, doi: 10.1109/TED.2014.2311473.

[93] S. Adachi, “Optical dispersion relations for GaP, GaAs, GaSb, InP, InAs, InSb, AlxGa1−xAs, and In1−xGaxAsyP1−y,” *J. Appl. Phys.*, vol. 66, no. 12, pp. 6030–6040, Dec. 1989, doi: 10.1063/1.343580.

[94] H. Fischer and O. J. F. Martin, “Engineering the optical response ofplasmonic nanoantennas,” *Opt. Express*, vol. 16, no. 12, pp. 9144–9154, Jun. 2008, doi: 10.1364/OE.16.009144.

[95] W. A. Murray, B. Auguié, and W. L. Barnes, “Sensitivity of Localized Surface Plasmon Resonances to Bulk and Local Changes in the Optical Environment,” *J. Phys. Chem. C*, vol. 113, no. 13, pp. 5120–5125, Apr. 2009, doi: 10.1021/jp810322q.

[96] H. Takeuchi, T. Sumioka, and M. Nakayama, “Longitudinal Optical Phonon-Plasmon Coupled Mode in Undoped GaAs/n-Type GaAs Epitaxial Structures Observed by Raman Scattering and Terahertz Time-Domain Spectroscopic Measurements: Difference in Observed Modes and Initial Polarization Effects,” *IEEE Trans. Terahertz Sci. Technol.*, vol. 7, no. 2, pp. 124–130, Mar. 2017, doi: 10.1109/TTHZ.2017.2650220.

[97] R. Fernández-García, Y. Sonnefraud, A. I. Fernández-Domínguez, V. Giannini, and S. A. Maier, “Design considerations for near-field enhancement in optical antennas,” *Contemp. Phys.*, vol. 55, no. 1, pp. 1–11, Jan. 2014, doi: 10.1080/00107514.2013.850788.

[98] N. Kumar, S. Mignuzzi, W. Su, and D. Roy, “Tip-enhanced Raman spectroscopy: principles and applications,” *EPJ Tech. Instrum.*, vol. 2, no. 1, Dec. 2015, doi: 10.1140/epjti/s40485-015-0019-5.

[99] M. Zhang, R. Wang, Z. Zhu, J. Wang, and Q. Tian, “Experimental research on the spectral response of tips for tip-enhanced Raman spectroscopy,” *J. Opt.*, vol. 15, no. 5, pp. 1–5, May 2013, doi: 10.1088/2040-8978/15/5/055006.

[100] M. W. Knight, Y. Wu, J. B. Lassiter, P. Nordlander, and N. J. Halas, “Substrates Matter: Influence of an Adjacent Dielectric on an Individual Plasmonic Nanoparticle,” *Nano Lett.*, vol. 9, no. 5, pp. 2188–2192, 2009, doi: 10.1021/nl900945q.

[101] G. N. Malheiros-Silveira, G. S. Wiederhecker, and H. E. Hernández-Figueroa, “Dielectric resonator antenna for applications in nanophotonics,” *Opt. Express*, vol. 21, no. 1, pp. 1234–1239, Jan. 2013, doi: 10.1364/OE.21.001234.

[102] J. Hecht, *Understanding fiber optics*, 5th ed. Upper Saddle River, N.J: Pearson/Prentice Hall, 2006.

[103] L. Novotny, “Effective Wavelength Scaling for Optical Antennas,” *Phys. Rev. Lett.*, vol. 98, no. 26, p. 266802, Jun. 2007, doi: 10.1103/PhysRevLett.98.266802.

[104] J. Aizpurua, G. W. Bryant, L. J. Richter, F. J. García de Abajo, B. K. Kelley, and T. Mallouk, “Optical properties of coupled metallic nanorods for field-enhanced spectroscopy,” *Phys. Rev. B*, vol. 71, no. 23, p. 235420, Jun. 2005, doi: 10.1103/PhysRevB.71.235420.

[105] I. V. Minin and O. V. Minin, *Microsensors*. Rijeka: InTech, 2011.

[106] X. Zhang and Z. Liu, “Superlenses to overcome the diffraction limit,” *Nat. Mater.*, vol. 7, no. 6, pp. 435–441, Jun. 2008, doi: 10.1038/nmat2141.

[107] R. Fernandez-Garcia, M. Rahmani, M. Hong, S. A. Maier, and Y. Sonnefraud, “Use of a gold reflecting-layer in optical antenna substrates for increase of photoluminescence enhancement,” *Opt. Express*, vol. 21, no. 10, pp. 12552–12561, May 2013, doi: 10.1364/OE.21.012552.

[108] P. Yeh, *Optical waves in layered media*. Hoboken, NJ: Wiley, 2005.

[109] J. D. Joannopoulos, S. G. Johnson, J. N. Winn, and R. D. Meade, *Photonic Crystals: Molding the Flow of Light (Second Edition).* Princeton: Princeton University Press, 2008.

[110] F. Galve and R. Zambrini, "Completely Subradiant Multi-Atom Architectures Through 2D Photonic Crystals," *Ann. Phys.*, vol. 530, no. 5, p. 1800017, Mar. 2018, doi: 10.1002/andp.201800017.

[111] J. P. Moura, R. A. Norte, J. Guo, C. Schäfermeier, and S. Gröblacher, "Centimeter-scale suspended photonic crystal mirrors," *Opt. Express*, vol. 26, no. 2, pp. 1895–1909, Jan. 2018, doi: 10.1364/OE.26.001895.

[112] I. W. Jung, S. B. Mallick, and O. Solgaard, "A Large-Area High-Reflectivity Broadband Monolithic Single-Crystal-Silicon Photonic Crystal Mirror MEMS Scanner With Low Dependence on Incident Angle and Polarization," *IEEE J. Sel. Top. Quantum Electron.*, vol. 15, no. 5, pp. 1447–1454, Sep. 2009, doi: 10.1109/JSTQE.2009.2021863.

[113] K. G. Lee, K. J. Ahn, H. W. Kihm, J. S. Ahn, and D. S. Kim, "Surface plasmon image dipole effect," in *2008 Conference on Lasers and Electro-Optics and 2008 Conference on Quantum Electronics and Laser Science*, 2008, pp. 1–2.

[114] Kane Yee, "Numerical solution of initial boundary value problems involving maxwell's equations in isotropic media," *IEEE Trans. Antennas Propag.*, vol. 14, no. 3, pp. 302–307, May 1966, doi: 10.1109/TAP.1966.1138693.

[115] A. F. Oskooi, D. Roundy, M. Ibanescu, P. Bermel, J. D. Joannopoulos, and S. G. Johnson, "Meep: A flexible free-software package for electromagnetic simulations by the FDTD method," *Comput. Phys. Commun.*, vol. 181, no. 3, pp. 687–702, Mar. 2010, doi: 10.1016/j.cpc.2009.11.008.

[116] I. Nathan, S. Yuferev, and R. Di, "A systematic approach to the concept of surface impedance boundary conditions," *Facta Univ. - Ser. Electron. Energ.*, vol. 22, no. 2, pp. 143–158, 2009, doi: 10.2298/FUEE0902143N.

[117] N. Farahat, S. Yuferev, and N. Ida, "High order surface impedance boundary conditions for the FDTD method," *IEEE Trans. Magn.*, vol. 37, no. 5, pp. 3242–3245, Sep. 2001, doi: 10.1109/20.952586.

(This page is intentionally left blank)

Appendix A: MEEP Code for Nano-Antenna Dielectric Cavity Hybrid Simulation

Appendix A contains sample code for the FDTD simulation of a hybrid antenna consisting of a dipole nano-antenna on top of a dielectric cavity. The sample code below was used for one iteration of the simulation with the same parameters as the CST simulations for the final design in Chapter 3. Quote under heading 3.4, " *In the final design, a gold strip dipole with arm lengths of 90nm and thickness of 20nm, is coupled to the TE122 mode of a GaAs dielectric cavity of 880nm × 880nm × 1000nm, with a plane wave excitation source going down in the –Z axis facing the surface with the dipole in an orthogonal direction.*"

```
from __future__ import division

import meep as mp
import numpy as np
import math
import cmath
import random
import argparse

# default unit length is 1 um
um_scale = 1.0
nm_scale = um_scale/1000

# conversion factor for eV to 1/um [=1/hc]
eV_um_scale = um_scale/1.23984193

#------------------------------------------------------------
-------
# gold (Au)
```

```
metal_range = mp.FreqRange(min=um_scale/6.1992,
max=um_scale/.24797)

Au_plasma_frq = 9.03*eV_um_scale
Au_f0 = 0.760
Au_frq0 = 1e-10
Au_gam0 = 0.053*eV_um_scale
Au_sig0 = Au_f0*Au_plasma_frq**2/Au_frq0**2
Au_f1 = 0.024
Au_frq1 = 0.415*eV_um_scale   # 2.988 um
Au_gam1 = 0.241*eV_um_scale
Au_sig1 = Au_f1*Au_plasma_frq**2/Au_frq1**2
Au_f2 = 0.010
Au_frq2 = 0.830*eV_um_scale   # 1.494 um
Au_gam2 = 0.345*eV_um_scale
Au_sig2 = Au_f2*Au_plasma_frq**2/Au_frq2**2
Au_f3 = 0.071
Au_frq3 = 2.969*eV_um_scale   # 0.418 um
Au_gam3 = 0.870*eV_um_scale
Au_sig3 = Au_f3*Au_plasma_frq**2/Au_frq3**2
Au_f4 = 0.601
Au_frq4 = 4.304*eV_um_scale   # 0.288 um
Au_gam4 = 2.494*eV_um_scale
Au_sig4 = Au_f4*Au_plasma_frq**2/Au_frq4**2
Au_f5 = 4.384
Au_frq5 = 13.32*eV_um_scale   # 0.093 um
Au_gam5 = 2.214*eV_um_scale
Au_sig5 = Au_f5*Au_plasma_frq**2/Au_frq5**2

Au_susc = [mp.DrudeSusceptibility(frequency=Au_frq0,
gamma=Au_gam0, sigma=Au_sig0),
          mp.LorentzianSusceptibility(frequency=Au_frq1,
gamma=Au_gam1, sigma=Au_sig1),
          mp.LorentzianSusceptibility(frequency=Au_frq2,
gamma=Au_gam2, sigma=Au_sig2),
          mp.LorentzianSusceptibility(frequency=Au_frq3,
gamma=Au_gam3, sigma=Au_sig3),
          mp.LorentzianSusceptibility(frequency=Au_frq4,
gamma=Au_gam4, sigma=Au_sig4),
          mp.LorentzianSusceptibility(frequency=Au_frq5,
gamma=Au_gam5, sigma=Au_sig5)]

gold = mp.Medium(epsilon=1.0, E_susceptibilities=Au_susc,
valid_freq_range=metal_range)

#-------------------------------------------------------
-------
```

```
#-------------------------------------------------------------
-------

GaAs_range = mp.FreqRange(min=um_scale/17,
max=um_scale/0.97)

GaAs_frq1 = 1/(0.4431307*um_scale)
GaAs_gam1 = 0
GaAs_sig1 = 5.466742
GaAs_frq2 = 1/(0.8746453*um_scale)
GaAs_gam2 = 0
GaAs_sig2 = 0.02429960
GaAs_frq3 = 1/(36.9166*um_scale)
GaAs_gam3 = 0
GaAs_sig3 = 1.957522

GaAs_susc =
[mp.LorentzianSusceptibility(frequency=GaAs_frq1,
gamma=GaAs_gam1, sigma=GaAs_sig1),
          mp.LorentzianSusceptibility(frequency=GaAs_frq2,
gamma=GaAs_gam2, sigma=GaAs_sig2),
          mp.LorentzianSusceptibility(frequency=GaAs_frq3,
gamma=GaAs_gam3, sigma=GaAs_sig3)]

GaAs = mp.Medium(epsilon=5.372514,
E_susceptibilities=GaAs_susc, valid_freq_range=GaAs_range)

#-------------------------------------------------------------
-------


# cell size needs to be double of used space
cell_size = mp.Vector3(5,5,30)

# Defining geometries

geometry = [mp.Block(geom_dipole1,material=gold),
          mp.Block(geom_dipole2,material=gold),
          mp.Block(geom_cavity,material=GaAs)]

def main(args):
s = 13  # the size of the computational cell, not including
PML
dpml = 1  # thickness of PML layers
sxy = s + 2 * dpml  # cell size, including PML
cell = mp.Vector3(sxy, sxy, 0)
pml_layers = [mp.PML(dpml)]
resolution = 10

fcen = 0.5  # pulse center frequency
```

```
df = 0.001  # turn-on bandwidth
kdir = mp.Vector3(1, 1)  # direction of k (length is
irrelevant)
n = 1 # refractive index of material containing the source
k = kdir.unit().scale(2 * math.pi * fcen * n)  # k with
correct length
nfreq=3

#Gaussian source (planewave)
sources = [
     mp.Source(
     mp.GaussianSource(fcen, fwidth=df),
     component=mp.Ex,
     center=mp.Vector3(0, 0,-13.4),
     size=mp.Vector3(5,5,0),
     amplitude=1.0
     )
]

sim = mp.Simulation(
     cell_size=cell_size,
     sources=sources,
     boundary_layers=pml_layers,
     resolution=resolution,
     default_material=mp.Medium(index=n),
     geometry=geometry
)

#place box around flux get area
srcbox_width = 0.1
src_box = sim.add_flux(fcen, df, nfreq,

     mp.FluxRegion(center=mp.Vector3(0,0,(-
5.11+0.5*srcbox_width)),
size=mp.Vector3(srcbox_width,srcbox_width,0),
direction=mp.Z, weight=+1),

     #mp.FluxRegion(center=mp.Vector3(0,0,(-5.11-
0.5*srcbox_width)),
size=mp.Vector3(srcbox_width,srcbox_width,0),
direction=mp.Z, weight=-1),

     #mp.FluxRegion(center=mp.Vector3(0.5*srcbox_width,0,-
5.11), size=mp.Vector3(0,srcbox_width,srcbox_width),
direction=mp.X, weight=+1),
                          #mp.FluxRegion(center=mp.Vector3(-
0.5*srcbox_width,0,-5.11),
size=mp.Vector3(0,srcbox_width,srcbox_width),
direction=mp.X, weight=-1),
```

```
     #mp.FluxRegion(center=mp.Vector3(0,0.5*srcbox_width,-
5.11), size=mp.Vector3(srcbox_width,0,srcbox_width),
direction=mp.Y, weight=+1),

     #mp.FluxRegion(center=mp.Vector3(0,-0.5*srcbox_width,-
5.11), size=mp.Vector3(srcbox_width,0,srcbox_width),
direction=mp.Y, weight=-1))
                    )
# padding for flux box to fully capture waveguide mode
fluxbox_dpad = 0.05

#t=100
#sim.run(mp.at_every(10), until=t)
sim.run(until_after_sources=mp.stop_when_fields_decayed(
     50, mp.Ex, mp.Vector3(0, 0, 15), 1e-6))

sim.display_fluxes(src_box)

flux_total=mp.get_fluxes(src_box)
#flux_srcbox_top+flux_srcbox_bot+flux_srcbox_xp+flux_srcbox_
xm+flux_srcbox_yp+flux_srcbox_ym

fieldEX=sim.get_field_point(mp.Ex, mp.Vector3(0,0,-5.11))

print ("Flux is ", flux_total)

#visualize in 3D
sim.init_sim()

eps_data = sim.get_epsilon()

from mayavi import mlab
s = mlab.contour3d(eps_data, colormap="YlGnBu")
mlab.show()
```

(This page is intentionally left blank)

Appendix B: Complex Permittivity of Gold

Appendix B lists the complex permittivity value of Gold from 50 – 1000 THz. The data is obtained from the Brendel-Bormann Model [79]. A continuous plot is also displayed that is a replica of Figure 2.7.

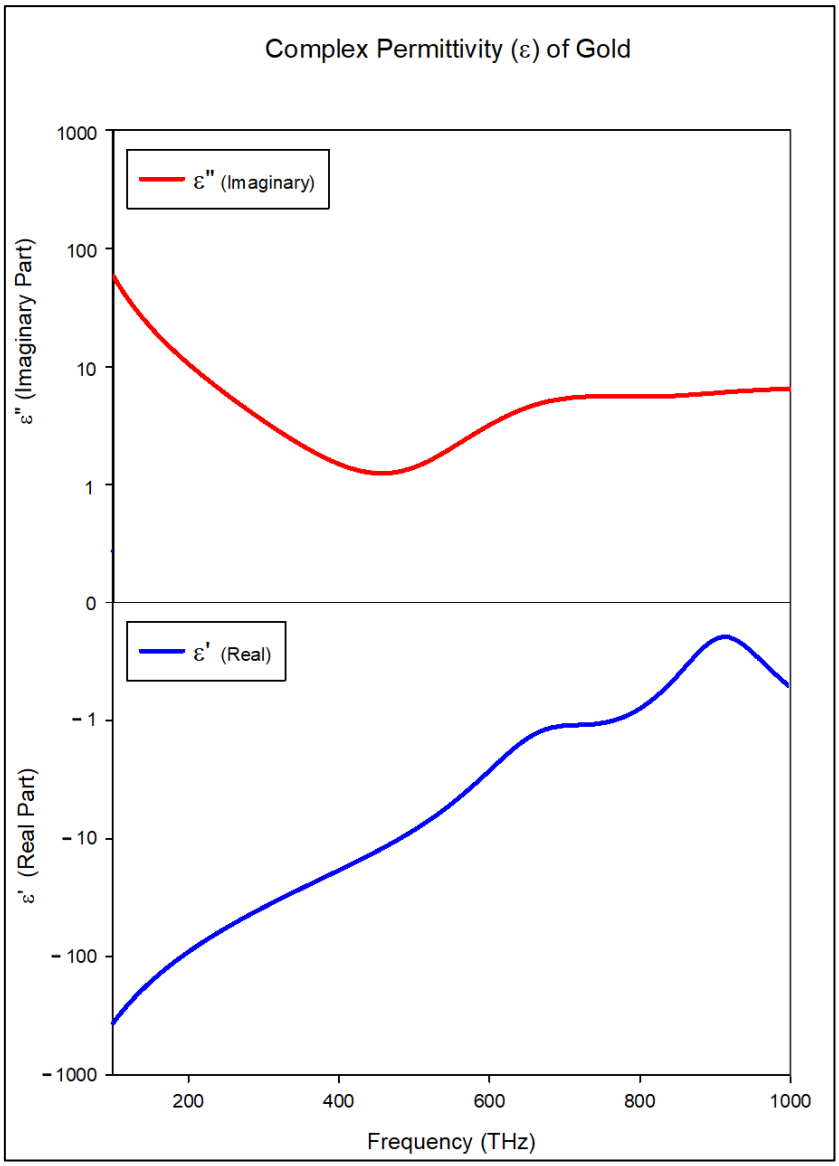

Table A: Complex permittivity values for gold

Frequency (THz)	e1 (real)	e2 (imaginary)
48.35986	-1472.9	402.17
49.14872	-1428.7	384.82
49.94959	-1385.8	368.23
50.7641	-1344.1	352.35
51.59229	-1303.6	337.17
52.43327	-1264.2	322.65
53.28886	-1226	308.77
54.15718	-1188.9	295.49
55.04011	-1152.8	282.8
55.93769	-1117.8	270.65
56.84994	-1083.8	259.04
57.77684	-1050.8	247.94
58.71951	-1018.7	237.33
59.67682	-987.61	227.18
60.6499	-957.41	217.48
61.63876	-928.1	208.2
62.6447	-899.66	199.33
63.66642	-872.05	190.85
64.70387	-845.27	182.74
65.75982	-819.28	174.99
66.83144	-794.06	167.57
67.92162	-769.59	160.49
69.02889	-745.86	153.71
70.15479	-722.84	147.23
71.29767	-700.51	141.04
72.46089	-678.84	135.11
73.6428	-657.83	129.45
74.84333	-637.46	124.03
76.06436	-617.7	118.86
77.30395	-598.54	113.9
78.56402	-579.95	109.16
79.84671	-561.94	104.63
81.14781	-544.47	100.3
82.47158	-527.53	96.157
83.81583	-511.1	92.192
85.18283	-495.18	88.399
86.57266	-479.75	84.771
87.98276	-464.78	81.299
89.41822	-450.28	77.978
90.87649	-436.21	74.799
92.3575	-422.58	71.758

93.86407	-409.37	68.846
95.39631	-396.57	66.06
96.95119	-384.15	63.393
98.53167	-372.12	60.839
100.1378	-360.47	58.394
101.7729	-349.17	56.053
103.4302	-338.21	53.811
105.1166	-327.6	51.663
106.8322	-317.32	49.606
108.5733	-307.35	47.636
110.3436	-297.69	45.747
112.1432	-288.33	43.938
113.9722	-279.26	42.204
115.8305	-270.47	40.542
117.718	-261.95	38.948
119.6394	-253.7	37.42
121.5901	-245.7	35.954
123.5748	-237.95	34.549
125.5886	-230.44	33.2
127.6364	-223.16	31.907
129.7185	-216.11	30.665
131.8349	-209.28	29.473
133.9855	-202.66	28.33
136.1703	-196.25	27.231
138.3892	-190.03	26.176
140.642	-184.01	25.163
142.9353	-178.17	24.19
145.2694	-172.52	23.255
147.6374	-167.04	22.356
150.0463	-161.73	21.492
152.4885	-156.59	20.661
154.9796	-151.6	19.862
157.5037	-146.77	19.094
160.0771	-142.09	18.355
162.6831	-137.55	17.643
165.3389	-133.15	16.959
168.0357	-128.89	16.3
170.7733	-124.76	15.666
173.5613	-120.76	15.055
176.39	-116.88	14.467
179.2695	-113.12	13.901
182.1893	-109.48	13.355
185.1599	-105.95	12.829
188.1818	-102.53	12.322
191.243	-99.21	11.833
194.3675	-95.994	11.363

197.5308	-92.876	10.909
200.7584	-89.853	10.471
204.0237	-86.923	10.049
207.354	-84.082	9.6417
210.7356	-81.328	9.2491
214.1681	-78.657	8.8705
217.6668	-76.068	8.5054
221.2164	-73.556	8.1532
224.8162	-71.121	7.8135
228.4829	-68.759	7.4859
232.2172	-66.469	7.17
236.0013	-64.247	6.8653
239.8532	-62.091	6.5715
243.7535	-60.001	6.2883
247.7419	-57.972	6.0154
251.7783	-56.005	5.7523
255.8829	-54.095	5.4988
260.0559	-52.242	5.2546
264.2973	-50.444	5.0196
268.6072	-48.7	4.7933
272.9853	-47.006	4.5755
277.4315	-45.362	4.3661
281.9718	-43.766	4.1648
286.5537	-42.217	3.9715
291.2303	-40.713	3.7858
295.9744	-39.252	3.6077
300.8092	-37.834	3.4369
305.7141	-36.456	3.2733
310.698	-35.118	3.1167
315.7638	-33.819	2.9671
320.9151	-32.556	2.8242
326.1485	-31.329	2.6879
331.4638	-30.136	2.5581
336.872	-28.978	2.4346
342.3656	-27.851	2.3175
347.9485	-26.756	2.2065
353.6206	-25.691	2.1016
359.3858	-24.655	2.0028
365.2487	-23.648	1.9099
371.2048	-22.668	1.8229
377.2588	-21.714	1.7418
383.4104	-20.785	1.6665
389.6597	-19.881	1.5971
396.0166	-19	1.5336
402.4708	-18.142	1.476
409.0384	-17.306	1.4245

415.7029	-16.49	1.3791
422.4869	-15.695	1.3401
429.3729	-14.918	1.3076
436.3728	-14.16	1.2819
443.4931	-13.42	1.2635
450.7208	-12.696	1.2528
458.0761	-11.989	1.2502
465.5452	-11.296	1.2565
473.1349	-10.619	1.2723
480.8528	-9.9565	1.2986
488.6911	-9.3082	1.3361
496.6576	-8.674	1.3861
504.7606	-8.0541	1.4496
512.9919	-7.4489	1.5277
521.351	-6.8592	1.6218
529.8559	-6.286	1.733
538.4977	-5.7308	1.8623
547.2763	-5.1954	2.0105
556.2012	-4.682	2.1782
565.2729	-4.1933	2.3655
574.4911	-3.7322	2.5719
583.8558	-3.3018	2.7963
593.3782	-2.9053	3.0368
603.0585	-2.5459	3.2906
612.8845	-2.2261	3.5539
622.8807	-1.9482	3.8222
633.0345	-1.7133	4.0901
643.3591	-1.5214	4.3516
653.8549	-1.3713	4.6006
664.522	-1.2601	4.8309
675.3603	-1.1833	5.0369
686.3695	-1.1352	5.2139
697.5649	-1.1088	5.3587
708.9303	-1.0962	5.4698
720.4991	-1.0893	5.5479
732.237	-1.0805	5.5957
744.1789	-1.063	5.6178
756.3259	-1.0317	5.6205
768.6592	-0.98359	5.6112
781.1774	-0.91772	5.5978
793.9209	-0.83561	5.5876
806.8698	-0.74077	5.5872
820.0237	-0.63838	5.6014
833.405	-0.53459	5.6333
846.991	-0.43591	5.6837
860.8047	-0.34853	5.7515

874.8467	-0.27775	5.8339
889.117	-0.22758	5.9267
903.6153	-0.20055	6.0253
918.3411	-0.19767	6.1244
933.3223	-0.21854	6.2191
948.5302	-0.2616	6.3051
963.9939	-0.32438	6.3788
979.7139	-0.40381	6.4373
995.6905	-0.49646	6.4787
1011.924	-0.59878	6.5019

Appendix C: Complex Permittivity of Gallium Arsenide

Appendix C lists the complex permittivity value of Gallium Arsenide from 100 – 600 THz. The data is obtained from the Adachi Model [93]. A continuous plot is also displayed that is a replica of Figure 2.8.

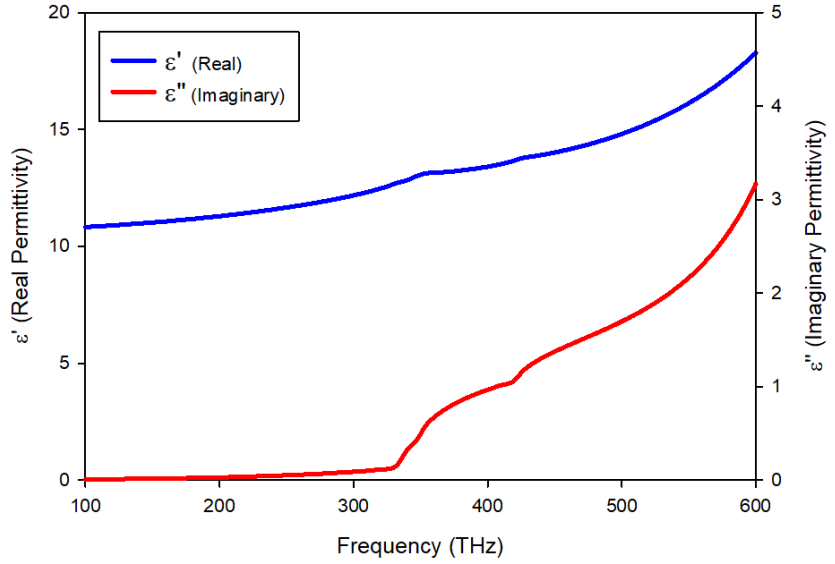

Table B: Complex permittivity values for gallium arsenide

Frequency (THz)	**Ɛ' (Real Part)**	**Ɛ'' (Imaginary Part)**
95.9	11.1416	0.0299
103.0	11.1562	0.0322
110.2	11.1723	0.0345
117.4	11.1890	0.0368
124.5	11.2071	0.0392
131.7	11.2265	0.0415
138.9	11.2473	0.0439
146.0	11.2687	0.0463
153.2	11.2922	0.0488

160.4	11.3164	0.0512
167.6	11.3420	0.0537
174.7	11.3696	0.0562
181.9	11.3980	0.0588
189.1	11.4284	0.0614
196.2	11.4595	0.0640
203.4	11.4927	0.0666
210.6	11.5280	0.0693
217.7	11.5646	0.0720
224.9	11.6028	0.0747
232.1	11.6430	0.0775
239.2	11.6853	0.0803
246.4	11.7298	0.0832
253.6	11.7771	0.0861
260.8	11.8259	0.0891
267.9	11.8782	0.0921
275.1	11.9327	0.0952
282.3	11.9908	0.0983
289.4	12.0525	0.1015
296.6	12.1178	0.1047
303.8	12.1889	0.1080
310.9	12.2659	0.1113
318.1	12.3507	0.1148
325.3	12.4465	0.1182
332.4	12.5611	0.1218
339.6	12.7196	0.1254
346.8	12.9320	0.3288
354.0	12.9341	0.4700
361.1	12.9425	0.5561
368.3	12.9577	0.6183
375.5	12.9788	0.6662
382.6	13.0060	0.7042
389.8	13.0405	0.7350
397.0	13.0811	0.7603
404.1	13.1290	0.7812
411.3	13.1859	0.7987
418.5	13.2539	0.8133
425.6	13.3453	0.8327
432.8	13.4386	0.9392
440.0	13.4827	1.0195
447.1	13.5335	1.0949
454.3	13.5901	1.1719
461.5	13.6532	1.2522
468.7	13.7227	1.3364
475.8	13.7995	1.4247
483.0	13.8820	1.5169

490.2	13.9719	1.6128
497.3	14.0692	1.7122
504.5	14.1747	1.8148
511.7	14.2870	1.9205
518.8	14.4085	2.0289
526.0	14.5378	2.1397
533.2	14.6773	2.2529
540.3	14.8265	2.3681
547.5	14.9862	2.4851
554.7	15.1583	2.6038
561.9	15.3422	2.7240
569.0	15.5397	2.8455
576.2	15.7528	2.9682
583.4	15.9817	3.0920
590.5	16.2293	3.2167
597.7	16.4968	3.3422
604.9	16.7864	3.4684

(This page is intentionally left blank)

Appendix D: MATLAB Code for DRA Design

Appendix D contains code that was run in MATLAB to calculate the resonant modes for a DRA of certain dimensions. Here, the code uses the following parameters:

- Width = 1200 nm
- Length = 1200 nm
- Height = 650 nm
- Permittivity of DRA, $\varepsilon_r = 12.94$

```
clc
%define constants%
pi=pi; er=12.94; c=3*10^17; %17 for nm, 11 for mm
%define dimensions of substrate%
a=1200;
b=a;
d=650;
%define TE modes%
m=1;
n=1;
p=1;
%start do loop%
i=1;
  for m=1:2:7
    for n=1:2:7
      for p=1:2:7
        kx=m*pi/a;
        ky=n*pi/b;
        %solving transcendental function to obtain kz
        f=@(vn) (vn*vn*tan(vn*d/2)*tan(vn*d/2))-(((er-
1)/er)*((kx*kx)+(ky*ky)+(vn*vn)))+(vn*vn);
        kz=fzero(f,10e-4);
        ko=sqrt((kx*kx)+(ky*ky)+(kz*kz))/sqrt(er);
        fo=ko*c/(2*pi);

        fr=fo*(10^-12); %convert resonant frequency to THz;
12 for THz, 9 for GHz
        %fg=2*pi*a*fo*sqrt(er)/c;
        %i,m,n,p,fr,fg
        disp(sprintf('%1.0f \t %1.0f \t %1.0f \t %1.0f \t
%4.1f',i,n,m,p,fr));
```

```
        %disp(sprintf('i=%1.0f \t m=%1.0f \t n=%1.0f \t
p=%1.0f \t fr=%4.1f',i,m,n,p,fr));
        %disp(sprintf('Resonant freq (THz) = %4.1f\n',fr));
                i=i+1;
      end
    end
  end
```

Appendix E: NFIE for Substrate of Varying Permittivity

Appendix E lists the values obtained during simulation in CST for a dielectric substrate with length, width, and height of 1200, 1200, and 50nm. A plane wave has been induced upon the structure and the maximum NFIE on the surface has been monitored for permittivities over a range of ε_r = 1-50 and a frequency range of f = 100-300 THz. The maximum NFIE on the surface of the dielectric substrate was recorded.

Table C: Increase of electric field enhancement and NFIE across various dielectric constants

Relative Permittivity (ε_r)	**Maximum Enhancement (V/m)**	**NFIE (V^2/m^2)**
1	1	1
2.25	1.03	1.07
4	1.18	1.39
7	1.84	3.37
9	2.27	5.13
11	2.5	6.24
13	2.77	7.65
15	2.93	8.63
20	3.47	12.07
25	3.71	13.76
30	4.09	16.73
35	4.29	18.40
40	4.71	22.18
50	4.98	24.80

(This page is intentionally left blank)